CZECH TECHNICAL UNIVERSITY IN PRAGUE

FACULTY OF BIOMEDICAL ENGINEERING
Department of Biomedical Technology

Development of methods for the detection and reduction of image artifacts during surface acquisition with high-frequency ultrasound

Master thesis

Study programme: Biomedical and Clinical Technology
Study branch: Biomedical Engineering (CEMACUBE)

Name of supervisor: doc. Ing. Martin Rožánek, Ph.D.

Katharina Hauprich

Kladno, August 2018

Department of Biomedical Technology   Academic year: 2017/2018

Diploma thesis assignment
(Master project thesis assignment)

Student:	**Katharina Hauprich**
Study branch:	Biomedical Engineering (CEMACUBE)
Title:	**Development of methods for the detection and reduction of image artifacts during surface acquisition with high- frequency ultrasound**
Title in Czech:	Vývoj metod pro detekci a redukci artefaktů u povrchových vysokofrekvenčních ultrazvukových obrazů

Instructions for processing:

Develop methods for detecting and reducing image artifacts in order to increase the process reliability of ultrasound images. Prepare a requirement profile, construct a reference model for the simulation of artifacts and develop and evaluate concepts and selected approaches. Document and discuss the chosen approach and achieved results distinctly and comprehensively.

References:

[1] VOLLBORN, T, Intraoraler Ultraschallmikroscanner für die digitale Abdrucknahme von Zahnpräparationen, Aachener Beiträge zur Medizintechnik, ročník 44, číslo 1, 2017
[2] CHUEMBOU PEKAM, F., MAROTTI, J., WOLFART, S., TINSCHERT, J., RADERMACHER, K., AND HEGER, S., High-frequency ultrasound as an option for scanning of prepared teeth. An in vitro study, Ultrasound in medicine & biology, ročník 41, číslo 1, 2015, 309–316 s.
[3] KREMKAU, F.W., AND TAYLOR, K.J., Artifacts in ultrasound imaging, Journal of ultrasound in medicine : official journal of the American Institute of Ultrasound in Medicine, ročník 5, číslo 4, 1986, 227–237 s.

Validity of assignment until date:	20.09.2019
Supervisor of diploma thesis:	doc. Ing. Martin Rožánek, Ph.D.
Consultant of diploma thesis:	Dipl.-Ing. Thorsten Vollborn

....
Head of Department   Dean

In Kladno, 19.02.2018

Declaration

I hereby declare that I have completed this thesis having the topic "Development of methods for the detection and reduction of image artifacts during surface acquisition with high-frequency ultrasound" independently and I have included a full list of used references.

I do not have a compelling reason against the use of this thesis within the meaning of Section 60 of the Act No 121/2000 Sb., on copyright and rights related to copyright and on amendment to some other acts (The Copyright Act), as amended.

In Aachen, 11.06.2018

Student´s signature

Acknowledgements

I would first like to thank my thesis advisor Univ.-Prof. Dr.-Ing. Klaus Radermacher of the Chair of Medical Engineering, Helmholtz-Institute for Biomedical Engineering of the RWTH Aachen University for giving me the opportunity to work on this thesis. I would also like to thank Doc. Ing. Martin Rožánek, Ph.D. of the Faculty of Biomedical Engineering at Czech Technical University in Prague, Czech Republic for his help in organisation in Prague.

Thanks a lot to Dipl.-Ing Daniel Habor and Dr.-Ing. Thorsten Vollborn for their patience and encouraging words during the thesis – highly appreciated! Finishing this thesis would not have been possible without you.

I would also like to thank the entire whitesonic GmbH and all employees of mediTEC. Thanks to Fabrice who dared hire me as a student assistant. Thanks to Christopher, Marie, Max, Benjamin, Kai, Florian and Fabian for all the unusual business ideas and hours of laughter in the container. It's been a pleasure working with you!

Finally, I would like to thank and dedicate this thesis to my parents Hannelore and Günter, as well as Christoph. They have always been a solid support when I had almost given up. Thank you!

Abstract

Function and aesthetic of human teeth take a high priority in everyday life. In order to produce a high-quality dental restoration, such as veneers, dental crowns or bridges, a particularly detailed impression of the prepared tooth region is needed. A high-frequency ultrasound based dental microscanner (S.CAI System, whitesonic GmbH, Aachen, Germany) has been proven to be a feasible system for this purpose. Nevertheless, as with other medical imaging modalities, sonography is prone to image artifacts. A strong degradation is given by air bubbles present in the coupling space. Due to the scanner movement, they cause a bowl-like artifact that is strongly dependent on the location of the bubble with respect to the beam focus. During signal processing, the artifact may be confused as originating from the tooth surface. Thus, air bubbles have to be detected to reduce their influence. Two indirect detection methods were developed. The outcome of the conceptual stage was given by a signal-based and an image-based technique that address the segmentation of the bowl artifact in the three-dimensional space. The signal-based method was aiming at the recognition of amplitude changes within the recorded A-signals, while the image-based method was detecting elliptic structures in C-Mode images. Both procedures proof to be potential detection methods but show to be limited in their detection ability and robustness. Further developments are required to accomplish a feasible detection approach.

keywords – high-frequency ultrasound, dental microscanner, digital dental impression, ultrasound image artifacts, semi-automated artifact detection, indirect air bubble detection

Table of Contents

1. Introduction

Human teeth perform several functions such as food intake and comminution as well as support and shape of the lower facial contour. They contribute significantly to articulation and pronunciation. In addition, an aesthetic denture plays an important social role in any society. Hence, function and aesthetic of teeth take a high priority in everyday life. In modern dentistry, a broad spectrum of dental treatments can be used to maintain natural, healthy teeth. In Germany, an increased health awareness and good dental care led to a decline in carious lesions in the population, especially in children and adolescents that can be attributed to the strengthened prophylactic supply [Hoffmann et al. 2006]. Nevertheless, the number of accounting cases for restorative measures according to §5 SGB V stagnates at more than 8 million per year since 2007 [BMG 2009, 2012]. Tooth-preserving treatments take about two-thirds of the working time in German dental practices of which approximately 15% are attributable to prosthetic services [Brecht et al. 2009]. If conservating treatments are no longer feasable and strong damage to hard tooth substance is recorded, dental restorative procedures such as veneers, artificial crowns or dental bridges are required. Restoring dental functions as well as aesthetic and phonetic measures are part of dental prosthetics [Strub 2011]. Due to technical innovations, decisive progress was made in the prosthetic field which also promotes the development of new materials. In this course, computer-aided design (CAD) and computer-aided manufacturing (CAM) processes found their application in the dental healthcare sector [Susic et al. 2017]. In 2002, sale and distribution of dental goods, especially dental prosthetics, had a production volume of about 2 Billion Euro and represented the largest position of medical technology productions in Germany. It therefore offers a lucrative economic sector for further development of processes, systems and devices [Krawczyk et al. 2005]. In dental prosthetics, the production of high-quality restorative dentures requires a dental impression with the highest possible dimensional accuracy and detailed reproduction of the intraoral situation [Strub 2011]. Common methods are given by the conventional impression taking by means of elastomer-based materials, such as silicone, to achieve a negative duplication, as well as digital impression based on optical scanner systems. Although integration into the digital process flow is realized by optical systems both methods have major disadvantages. Equigingival and subgingival treatments require a painful exposure of the preparation margin, usually done with retraction cords, soft tissue lasers, or electrosurgically. Additionally, drainage is needed to reduce falsification of the outcome (e.g., by displacement of materials). Therefore, blood and saliva are critical factors in impression taking. Furthermore, inaccuracies that occur during this process are unlikely to result in high-quality and cost-

effective restorations. In worst case, the procedure has to be repeated to the detriment of the patient. Also, additional working steps lengthen the treatment time. In order to minimize the impact of confounding factors mentioned, an ultrasound-based microscanner as described in [Vollborn 2017] offers an attractive alternative. In medicine, the physics of ultrasound are exploited in various applications for diagnostics and therapy [Oppelt 2011]. Gingiva, blood, and saliva can be penetrated non-invasively by acoustic waves. This provides the ability of a patient-friendly procedure and also ensures the intregration in the digital work flow. In a cooperation of the whitesonic GmbH (Aachen, Germany) and the Chair of Medical Engineering at RWTH Aachen University (Aachen, Germany), the concept of an ultrasound-based intraoral scanner is developed. In order to obtain a detailed reproduction, a resolution in the micrometer range is required, which can be achieved by high-frequency ultrasound. Various data processing steps are implemented to obtain a digital three-dimensional (3D) reconstruction of the tooth surface to form the basis of CAD/CAM procedures. However, as with other medical imaging modalities, such as magnetic resonance imaging (MRI) or x-ray based computed tomography (CT), medical sonography is prone to image artifacts [Krupa & Bekiesińska-Figatowska 2015; Boas & Fleischmann 2012; Kremkau & Taylor 1986]. These artifacts may adversely affect and distort the appearance of the surface geometry of the final 3D reconstruction. Trapped air in the ultrasonic coupling medium is known to be a strong degradation factor in acoustic examinations as it may direct physical parameters such as sound propagation and acoustic penetration depth. Caused by the transducer´s trajectory of the present intraoral scanner, characteristic bowl-like artifacts may result from acoustic waves reflected at an air inclusion. This distortion may be confused as being tooth structure in sonographic examinations. However, a precise fit of the dental restoration on the prepared tooth is important for a healthy integration of the prosthesis [Bader et al. 1991; Knoernschild & Campbell 2000]. In order to avoid misrepresentation of the digital tooth model, a bubble´s artifact has to be recognized and identified. Therefore, objective of this thesis is to develop a method for the detection and reduction of the characteristic air bubble artifacts after sonographic data acquisition. In the following chapter 2, the medical problem is explained in detail. Analysis of the state of the art in dental technology regarding the intraoral impression taking and the novel scanning system are described. Requirements for an ultrasound-based detection system will subsequently lead to concepts, which are described in ch. 3. Two of the concepts are pursued. The approaches implemented in the frame of this work are described in ch. 4 and evaluated by three *in vitro* and one *in vivo* sample. Ch. 5 and 6 demonstrates the findings obtained by the implementations as well as a discussion about the chosen methods. A conclusion is given in ch. 7.

2. Medical and Technical Background

This chapter provides a brief introduction into the anatomical basis of human dentitions as well as an overview of the state-of-the-art of conventional and digital impression taking for the production of high-quality fixed dental restorations in the field of dental prosthetics. In this context, a novel ultrasound-based micro-scanner is presented, its data processing discussed and difficulties of ultrasound image artifacts are demonstrated.

2.1 Anatomical Basis

Dental Classification and Function

The adult human dentition consists of a total of 32 teeth (including the wisdom teeth) that are evenly arranged in the dental arch of the upper (*maxilla*) and lower jaw (*mandibula*) (see **Figure 1a**). Due to their function and position one distinguishes between incisors (*dentes incisivi*), canines (*dentes canini*), premolars (*dentes praemolares*) and molars (*dentes molares*). With their sharp cutting edge (incisal edge), the incisors and canines located in the anterior region are mainly used for grasping and tearing food. In contrast to posterior teeth they have no chewing surface (occlusal surface). The premolars and molars in the posterior region perform the function of chopping and grinding food during the chewing process to create a swallowable mass. In order to clearly identify teeth in the jaw and in the dental arch, several teeth schemes have been developed in history [Strub 2011]. The most widely used internationally valid dental notation system was defined by the Fédération Dentaire Internationale (FDI) in [DIN EN ISO 3950 2016]. It is a two-digit identifier in which the first digit denotes the quadrant of the dentition (1-4) and the second digit the tooth (1-8, mesial to distal). **Figure 1b** illustrates the labeling.

Tooth Structure and Periodontal Apparatus

Despite the different functions and shapes of the teeth, their basic structure remains the same. A single tooth consists of a dental crown (*corona dentis*), dental neck (*cervix dentis*) and dental root (*radix dentis*) and is composed of several layers. In a healthy set of teeth, only the crown is exposed to the oral cavity protruding from the gum (*gingiva*). It is covered by tooth enamel (*enamelum*), which is the hardest substance found in the human body. Chemically, enamel is composed of 95% minerals (mostly the phosphate hydroxyapatite [$Ca_{10}(PO_4)_6(OH)_2$]), 1% oranic matrix and 4% water [Strub 2011]. Overlayed by enamel, the softer dentin (*substantia*

eburnea) represents a large proportion of the tooth. Dentin envelopes the tooth pulp (*pulpa dentis*) that fills the inner part of the tooth and extends from the dental crown to the tip of the dental root. The pulp consists of connective tissue containing the tooth nerve as well as blood and lymph vessels. Anatomically, a distinction is made between crown and root pulp. The transition from the tooth crown to the tooth root is called the dental neck or cervical. Due to the diversity of the teeth, the number of roots varies according to the tooth type. Usually, the incisors, canines and premolares are single-rooted, while the molars in the upper jaw are three-rooted and in the lower jaw two-rooted. In most cases (>60%) the first upper premolar might also be two-rooted [Strub 2011].
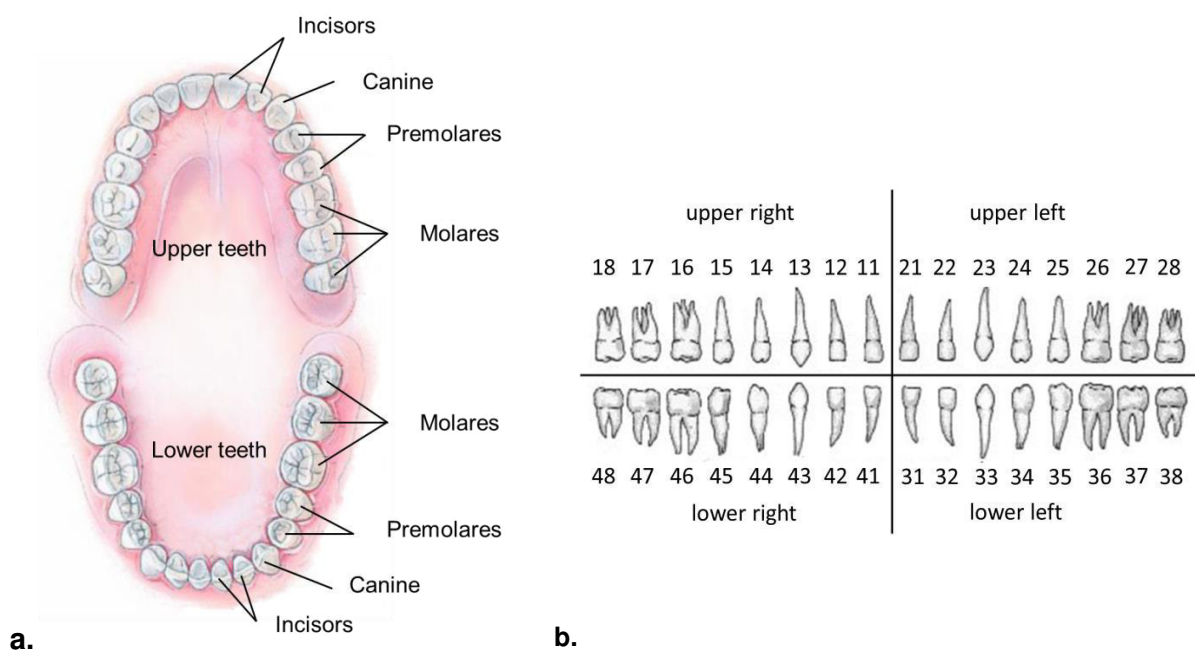

Figure 1: a. Permanent (secondary) dentition (modified from (m.f.) [Tortora & Nielsen 2012]); **b.** FDI Dental Notation System according to DIN EN ISO 3950 (m.f. [Sousa & Mourão 2015]).

All teeth are firmly anchored by their dental root in the periodontal apparatus (*parodontium*, *periodontium*). It consists of the gingiva, dental cement (*cementum*), tooth socket (*alveolus dentalis*), and the periodontal ligament (*ligamentum periodontale, desmodont*). The cementum covers the tooth root and anchors the Sharpey's fibers of the desmodont. An average of 28,000 fiber bundles are set up on a 1 mm² sized cement surface [Strub 2011]. These collagen fiber bundles connect the cement with the dental alveolus in the maxilla and mandible. Hence, the periodontal ligament acts as a shock absorber during chewing [Tortora & Nielsen 2012]. Gingiva covers the jaw bone and surrounds teeth cervically. It is to be differentiated between attached (*gingiva propria*) and marginal gingiva. The gingiva propria is fixed immovably by

dentogingival fibers (*fibrae dentogingivales*) on the alveolar bone and cementum. In contrast, the marginal gingiva is movable and located at the gum line. The gum extends slightly into each alveolar socket to form the gingival sulcus (*sulcus gingivae*) [Tortora & Nielsen 2012]. **Figure 2** illustrates a labeled sagittal section of a mandibular molar and the periodontal apparatus.
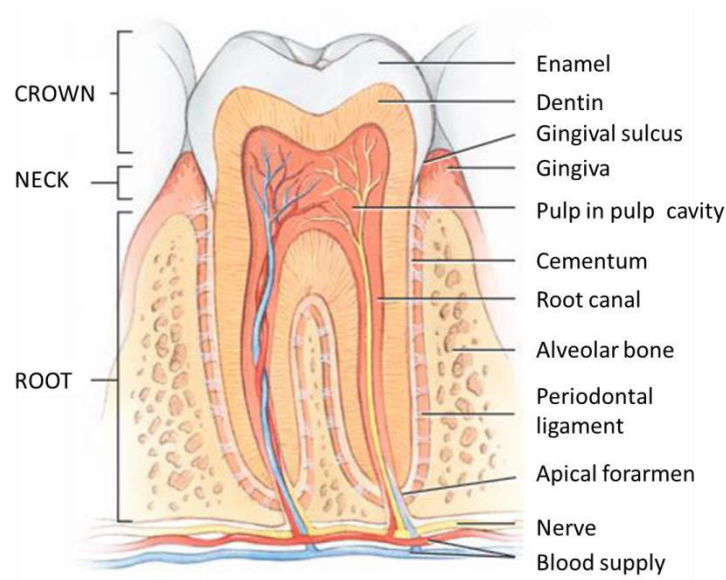

Figure 2: Sagittal section of a mandibular molar [Tortora & Nielsen 2012]

2.2 State of the Art

2.2.1 Dental prosthetics

Oral defects such as caries, periodontitis or trauma can lead to a severe weakening of teeth or may result in tooth loss. Dental prosthodontics can stabilize or replace defective structures, restore their functionality, and also contributes to aesthetics. The planning, production and integration of dental restorations is part of the field of dental prosthetics. Basically, a distinction is made between removable (partial or complete) prosthodontics as well as fixed dental restorations which include artificial crowns and bridges (see **Figure 3**). While in the past 50 years mainly metal-ceramic techniques have been used for the production, all-ceramic crowns and bridges are increasingly requested today [Meyer et al. 2014]. In addition to better aesthetic results, they show a higher biocompatibility, an enamel-like thermal expansion behavior, a reduced plaque accumulation as well as an acceptable clinical longevity [Della Bona & Kelly

2008; Anusavice 1992]. One major parameter for clinical success of fixed dental prosthetics is their accuracy of fit. A misfit on natural teeth may result in unwanted forces on the underlying teeth. An occlusal overload, for example, involves complications such as bone loss. However, natural teeth can handle a 25 - 100 μm axial and 56 - 108 μm lateral displacement in the dental socket due to the periodontal ligaments and therefore adapt to sligth changes in position [Kim et al. 2005]. Poor adaption also may result in damage to the tooth, periodontal tissue and the restoration itself [Bader et al. 1991; Knoernschild & Campbell 2000; Goodacre et al. 2003; El-Anwar et al. 2015].
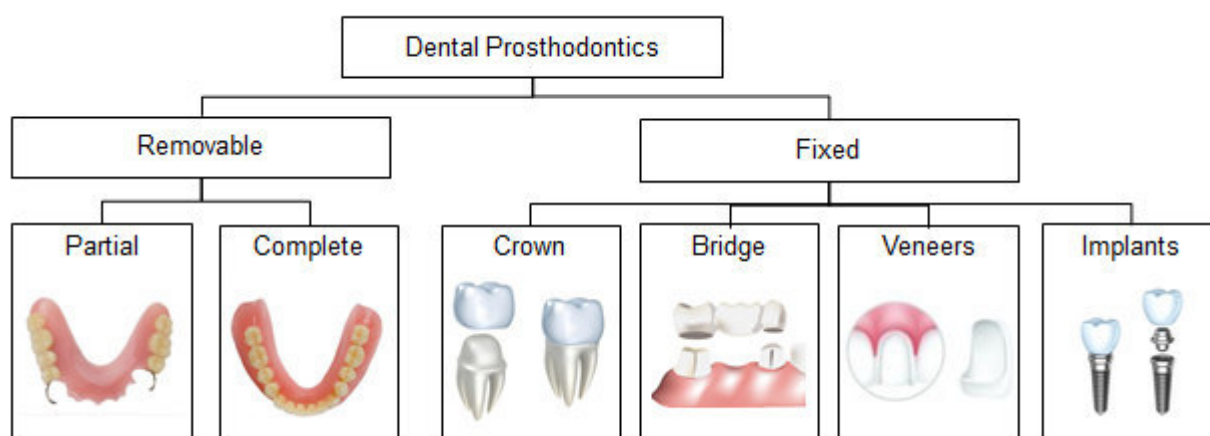

Figure 3: Dental prosthetics: A distinction is made between removable dentures and fixed dental restorations (m.f. [Vollborn 2017; CanStock 2018])

(Tooth) Preparation

If a dental prosthesis is required, the affected tooth needs to be prepared before a dental impression can be done. Preparation techniques greatly influence the long-term success of restorative procedures. Enough hard tooth substance must be removed to achieve a retention and resistance form, taking material-related, construction-related and aesthetic criteria into account, while preservation of natural tooth structures and protection of the dental pulp and marginal gingiva are required [Strub 2011]. **Figure 4** shows four common preparation margin shapes of a tooth stump in order to accommodate a restorative material. According to a study by Wimmer [Wimmer 2009] the chamfer finish line is the most commonly used type of preparation. Theoretically, an additional beveling of the shoulder preparation can avoid marginal errors [Lehmann et al. 2009], but due to the difficult application it is usually rejected today [Strub 2011]. Preparation of the crown stump as well as the values for marginal design and preparation depth in the cervical marginal area given in some guidelines depend on the

restorative materials to be used as well as the edge visibility [Strub 2011]. It is therefore necessary to consider each case individually.
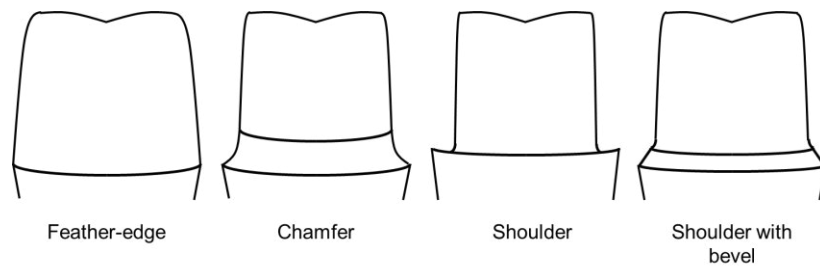

Figure 4: Tooth stump preparation margins with feather-edge, chamfer, or shoulder finish-line

In order to protect the marginal periodontium, a supragingival preparation is done. In some cases (i.e. defective cervix or aesthetic needs) however an equi- or subgingival preparation may be necessary. Hence, particular care should be taken to ensure that the biological width is maintained in order to avoid damaging the marginal periodontium [Padbury et al. 2003]. A reasonable gingiva management is therefore important. Commonly retraction cord and paste with astringent properties to keep the area free of moisture are applied (see **Figure 5**). Many clinicians also make use of electrosurgery or soft tissue lasers to easily create lateral space for a precise impression [Fasbinder 2010]. However, such techniques cause patient discomfort and bear a risk for permament gingival retraction [Phatale et al. 2010].
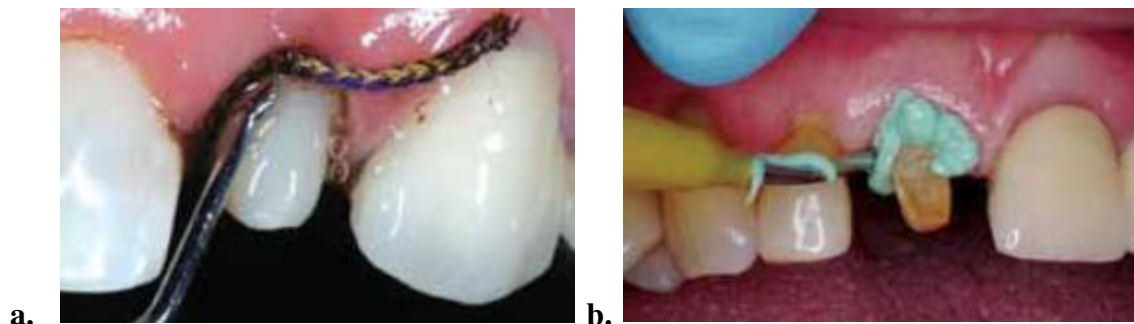
Figure 5: a. Placement of knitted retraction cord for crown preparation, **b.** Placement of paste into gingival sulcus [Strassler 2011]

Conventional Workflow

Conventional intra-oral impressions made of gypsum-based dental stone are traditionally the basis for prosthetic work. They are used by a dental technician in the dental laboratory to produce artificial crowns. Nevertheless, the development of new materials is accompanied by

the introduction of innovative digital techniques [Fasbinder 2010]. These include digital impression taking, and computer-aided design/computer-aided manufacturing (CAD/CAM) systems, which can be incorporated into the common process chains or replace the analog procedures completely (see **Figure 6**). Digital workflows aim at simplification of the process, the reduction of time needed and minimization of error sources. In the course of this work intra-oral impression taking is of particular interest and being discussed in more detail.
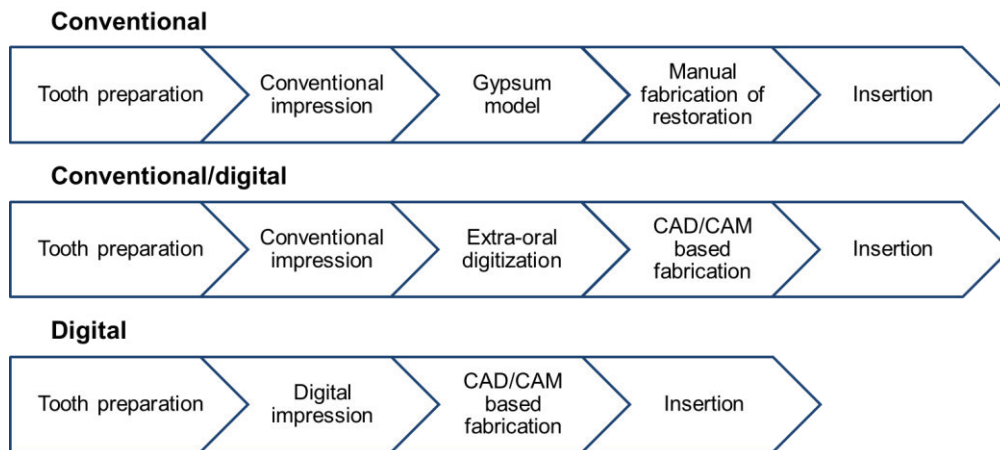

Figure 6: Conventional, conventional/digital and digital workflow for fixed dental restorations (m.f. [Gladbach 2018])

For the planning and production of a restorative denture, a model is necessary that reflects the situation in the oral cavity as accurately as possible. This is ensured by intra-oral impressioning, which can be performed both conventionally and digitally. In the conventional method, an impression material in the plastic state is introduced into the oral cavity. This binds to the desired tooth formation and solidifies. An impression tray holds the impression material as it sets. The result is a negative replica, which is used for further processing. **Figure 7** shows a negative impression in an impression tray and a dental cast of the mandible arch. Variant material components and applications require different impression techniques that can be identified as monophase or dual-phase. A simple and time-saving single step procedure is employed by monophase impressioning (also called single-viscosity technique) using a medium viscosity material (regular body) with high flow properties and dimensional stability. In the simultaneous dual-viscosity technique (sometimes also reffered to as one-step dual phase technique), however, two chemically identical elastic impression materials of different consistencies are used. A low-body material is injected directly into the affected areas and an impression tray containing a high-body material placed unpressurized into the oral cavity. The

two phases polymerize simultaneously. Another dual system is the two-step putty-wash method, which combines a pre-impression with a heavy body or putty material (usually silicone) and a correction impression with a light body to achieve an increased detailed rendition. In principle, it is possible that conventional impressions deform due to various influencing factors. In this context, individual material characteristics as well as the manual handling of the techniques may be mentioned. Thus, elastomers with little or no hydrophilicity may be displaced by saliva, or shrinkage of the extra-oral negative replica may occur as it might be the case in agar impressions. Concerning handling, increased pressure on the light body impression of the two-step dual system may damage the initial model [Strub 2011]. Therefore, guidelines for the various techniques must be followed to ensure accurate impression. Nevertheless, conventional impressions remain a cumbersome procedure for dentist and patient.
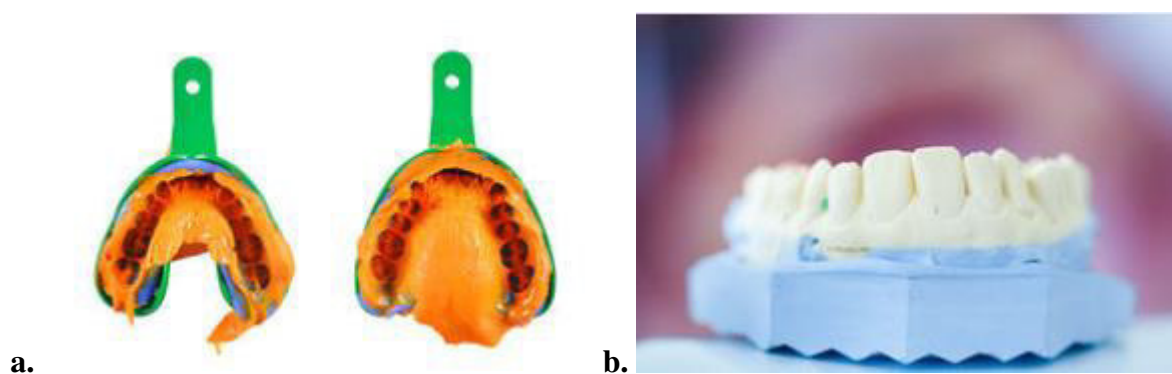

a.   b.

Figure 7: a. Dental negative replicate using silicone in impression tray by means of the one-step dual viscosity method; **b.** Dental gypsum model of a mandible impression [CanStock 2018]

Digital Intraoral Scanning

Replacing conventional impression methods, digital imaging techniques have been developed to record single teeth, quadrants or entire dental arches, giving the dentist the opportunity to perform a direct in-house (*chairside*) production of the restoration [Reich et al. 2012]. In addition, the user receives direct feedback due to an instant magnified display from various perspectives of the digital impression. Discrepancies in the preparation or digital image may be noted and corrected, and therefore prevents the patient from another visit in the dental practice. After recording, the data acquired from an intra-oral scanner are sent to a CAD system for the design of an artificial crown and to form a basis for the CAM system. The scanners currently available on the market are based on optical camera systems that serve the replication and digitization of the complex topography in oral regions. For a three-dimensional

(3D) surface reconstruction, these systems make use of the methods of triangulation [Schmidt 2010], *Active Wavefront Sampling* [Frigerio 2006; Hart et al. 2004] or confocal microscopy [Taneva et al. 2015; van der Meer et al. 2012]. In studies, a similar accuracy of digital optical systems as conventional impression techniques were verified [Seelbach et al. 2013; Boeddinghaus et al. 2015]. Therefore, they present a clinically relevant alternative. Neverthelesse, some optical systems require the application of an opaque powder to reduce the translucency of the tooth structure or non-reflective powder to prevent scattering. The uniformity of the application of the powder depends on the experience of the user and can contribute to a poor fit of the restoration in the case of strong local accumulations [Palin & Burke 2005].

Drawbacks of current Procedures

In both conventional and digital approaches, the precision of the intra-oral impression, particularly at the impression margin, is a critical factor for the production of a patient specific denture [Fasbinder 2010]. As the impression precedure is at the beginning of the process chain, it is unlikely that inaccuracies in the captured data will lead to a high-quality cost-effective restoration. Significant errors in an impression have to be corrected by repeating the procedure associated with further discomfort for the patient. In clinical practice, factors like tooth position, liquid contaminents such as gingival bleeding and saliva, the use of powder, and the location of the preparation margin (finish line) may greatly influence the outcome of an impression. Although digital optical systems show advantages over conventional impression taking, predominant disadvantages remain the same. To date, no commercially intra-oral scanning system has the capability to image the tooth surface through soft tissue that therefore has to be retracted from the preparation margins. To address these limitations, a high-frequency ultrasound-based (HFUS) intra-oral microscanner S.CAI (whitesonic GmbH, Aachen, Germany), which was developed in cooperation with the Chair of Medical Engineering at RWTH Aachen University, prevents a possible solution.

2.2.2 HFUS-assisted intraoral microscanner

Medical ultrasound imaging (sonography) is a widely used non-invasive imaging modality for the examination of (internal) body structures. Due to its physical characteristics, ultrasound has the ability to penetrate soft tissue and fluids without causing physical or biological damage to the patient [Barnett et al. 2000]. It therefore provides the option to image both the supra- and subgingival regions of prepared teeth in a digital impression without the need for gum retraction and/or draining. An *in vitro* study conducted by Chuembou Pekam *et al* [Chuembou

Pekam et al. 2015] using a 3-degrees of freedom (DOF) HFUS microscope (50 MHz) demonstrated great accuracy with an average deviation of < 30 μm (standard deviation $< 25\mu m$) between an ultrasound and an optical reference scan of a prepared human molar. These results are therefore in the clinically acceptable range. The single-element 2-DOF HFUS-based intra-oral microscanner, described in [Vollborn 2017], represents a digital impression system used for intraoral impression taking in case of prosthetic indications such as single-tooth crowns or three-unit bridges. The system performs a surface detection to obtain a digital data set for the planning of a dental restoration using ultrasound. Due to the high-frequency ultrasound (50 - 100 MHz), a resolution in the micrometer range can be achieved.

Operating Principle of the Microscanner

The ultrasound based intra-oral scanner consists of an application part as well as its associated hardware and software for signal processing, controlling, and visualization (see **Figure 8**). The scanner head is placed directly over the prepared tooth in the oral cavity by means of an interface element to initiate the scanning process. During mechanical movement of the focused single-element transducer located in the scanner head, the surface of the measuring area is detected pointwise using an impulse-echo method (see chapter **2.2.3**). The captured data enable a 3D surface digitization of the soft and hard tissue structures.
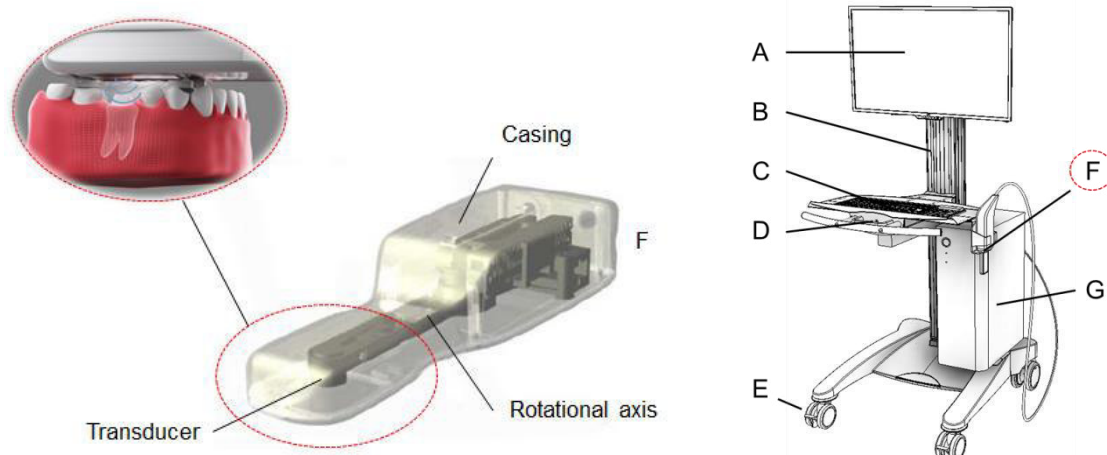

Figure 8: Components of the S.CAI microscanner system: **A.** Touchscreen, **B.** Transport cart, **C.** Keyboard, **D.** Handle **E.** Lockable rollers, **F.** Application part, **G.** Workstation (m.f. [Gladbach 2018])

The intraoral scanning system performs four major functions that include insertion, coupling, scanning, and data processing (see **Figure 9**). **Insertion** involves positioning and fixation of the scanner to the affected area in the oral cavity. For this purpose, an intraoral interface element is used which aligns the scan head parallel to the occlusal surface of the prepared

tooth. It serves as a mechanical link between the application part and the surface to be recorded. By actively biting on the intraoral handpiece by the patient, movements during the scanning process are averted.
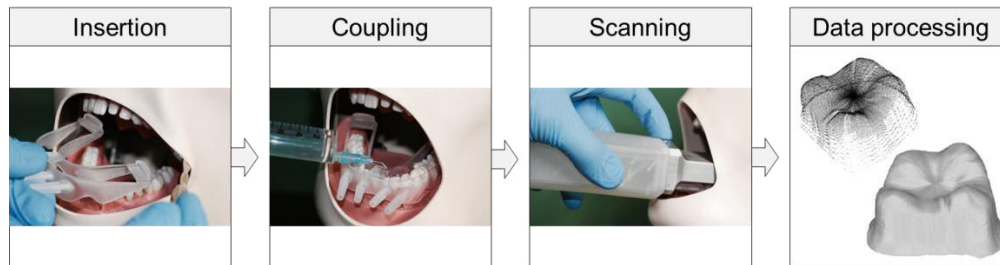

Figure 9: Four main functions of the microscanner system ([whitesonic GmbH 2017; Chuembou et al. 2014])

In the process of **coupling**, a coupling medium is used in order to adjust the impedance of the sound-emitting medium to soft tissue and, thus, to enable the transmission of acoustic waves in the sound path. The adaption causes a maximized reflection on the hard tooth structure, while this effect is minimized at the gingiva. Hence, the inclusion of air bubbles must be avoided. To protect the patient or user from moving components in the scanner head, a separation layer is required. This results in two coupling regions, which in the following are referred to as inner and outer coupling. Seperated from the outer coupling area by an acoustic window, the transducer is surrounded by the coupling medium. The outer coupling is given by the interface element, coupling chamber filled with coupling medium, and tooth structure. The two regions are fixed by actively biting by the patient. Outer and inner coupling form the intra-oral interface of the system (see **Figure 10**).
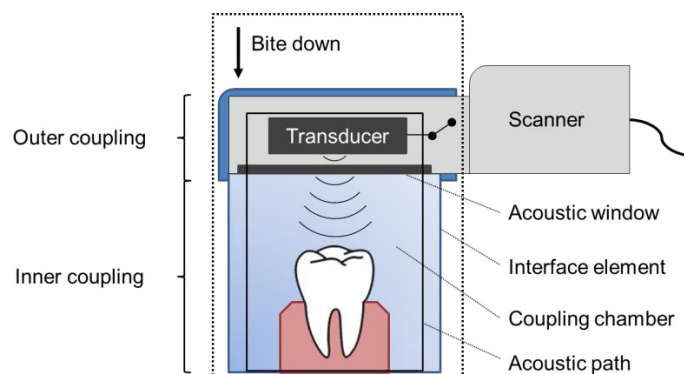

Figure 10: Intraoral interface of the HFUS-assisted microscanning system

During the **scanning** process, the tooth surface is detected pointwise. Therefore, the transducer is moved laterally in a slightly curved course over the image volume (see **Figure 11**). The two degrees of freedom (2-DOF) electrodynamic drive concept of the scanning movement shows a good precision due to low inertia and low inherent damping [Vollborn 2017]. Thus, an exact assignment of the captured surface points to the respective position is fascilitated, which in particular is relevant for digital reconstruction of the 3D tooth model. A single-element transducer is the central electroacoustic unit of the system. It contains a single piezoelectric cell that converts electrical energy into acoustic energy and vice versa. The received analog signals are passed on to an analog to digital converter (ADC) for digitization and further processing steps.
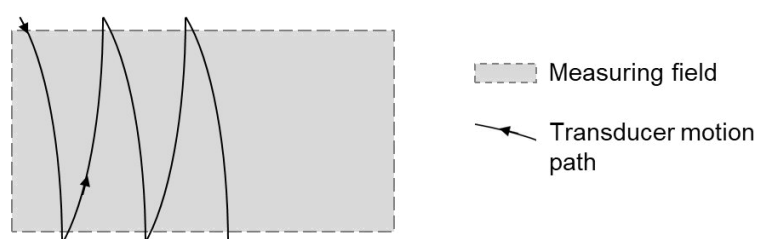

Figure 11: Motion path of 2-DOF single-element transducer (m.f. [Vollborn 2017])

Data processing includes signal processing and reconstruction for the formation of the tooth surface as well as a user interface for the configuration and visualization of a 3D model. Among others, object of signal processing is the optimization of raw data by filtering of disturbances and intensification of the signal-to-noise ratio (SNR). In a segmentation process, detected surface points are assigned to either hard or soft tissue to differentiate between tooth substance and gingiva. Afterwards the surface reconstruction of the segmented tooth structure is performed. As part of this work, signal processing is discussed in more detail.

2.2.3 Signal processing

Signal processing summarizes all processing steps that involve modification, analysis, and manipulation of information in a signal. In a technical-physical context, a signal itself describes an effect emanating from a physical object mathematically expressed as a function [Werner 2009]. In order to better understand the formation of ultrasound signals, the physical basis of ultrasound imaging is explained briefly.

Physical Basis of Ultrasound Imaging

Sound refers to a mechanical deformation in an elastic medium propagating as a (pressure) wave. High frequencies above the upper limit of the human audible frequency range (conventionally 20 Hz to 20 kHz) are called ultrasound [Lerch et al. 2009]. Its generation is performed by the conversion of electrical into mechanical energy at an electroacoustic transducer based on the piezoelectric effect. By means of a control unit, targeted voltage generation at the transducer can yield a defined sound pulse. The single-elemet transducer installed in the HFUS microscanner serves both as a transmitter and receiver of the ultrasonic waves, and thus implements the pulse-echo method. Other than electromagnetic waves, acoustic waves need an elastic medium for propagation which can either be gaseous, liquid or solid [Jenderka 2013]. As known from the fundamentals of physics, the spatial and temporal propagation of a mechanical wave can be described through characteristic parameters:

$$c = \frac{\lambda}{T} = \lambda \cdot f \qquad \text{2.1}$$

The speed of sound c is the velocity with which the wave moves through a medium. In general, this speed depends on the elastic and inertial properties of the material and therefore varies with tissue type, temperature, and pressure. The distance corresponding to one complete cycle of the wave is referred to as acoustic wavelength λ. Frequency f is the number of completed cycles per unit time. Usually, the unit Hertz [Hz] is used to describe cycles per second. The period T is the duration of time of one cycle (reciprocal of the frequency) [Oppelt 2011]. Also known from wave optics, sound phenomena occur if a propagating wave travels from one medium to another. In particular, these include reflection, transmission, scattering, and absorption (see **Figure 12**).
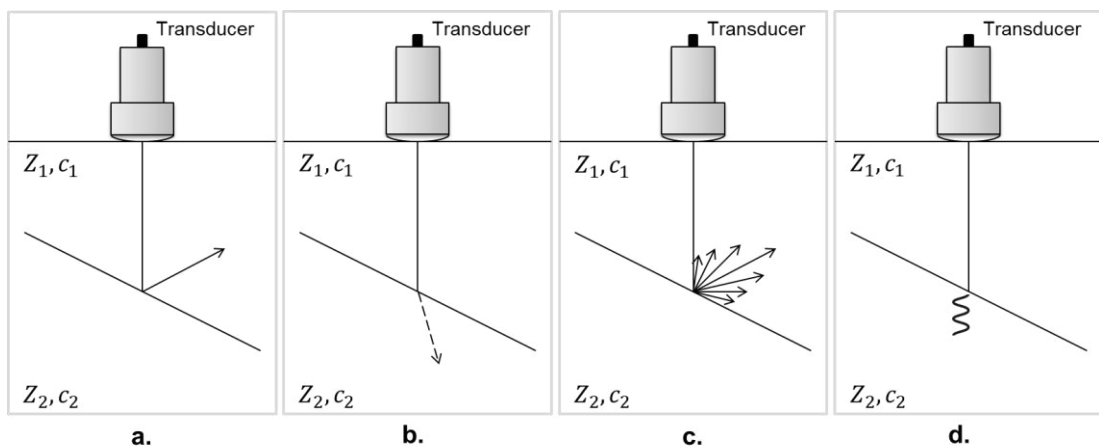

Figure 12: Sound phenomena at tissue boundaries: **a.** reflection, **b.** transmission, **c.** scattering, **d.** absorption

If an ultrasound beam strikes an acoustic boundary (i.e. couple medium-gingiva interface) part of the ultrasound energy is reflected off while some is transmitted. The strength of reflection is expressed by the reflection coefficient r, which describes the ratio of the intensity I_R and I_0 of a reflected and incident wave, respectively. The reflection coefficient R is directly related to the density ρ and speed of sound c in media, yielding the specific acoustic impedance Z [Oppelt 2011]. It follows:

$$Z = \rho \cdot c \qquad\qquad 2.2$$

$$R = \frac{I_R}{I_0} = \left(\frac{Z_2 - Z_1}{Z_2 + Z_1}\right)^2 \qquad\qquad 2.3$$

Hence, the greater the difference of acoustic impedance between two media, the stronger is the reflection. For example, the transition of a sound wave from solids or liquids to air results in a reflection coefficient close to 1, which is equivalent to a total reflection. Following the law of reflection, the angle of a specular reflection is equal to the angle of incidence. Thus, the change in the propagation direction may lead to a decrease in the measurable reflection component of the sound waves. In contrast, sound is reflected off diffusely on rough surfaces. Backscattered ultrasound waves allow record of echoes at the transducer, even if its axis is not coaxial with that of the receding beam. Absorption is refered to the reduction in intensity of the sound waves as it passes through tissue. Most of the energy lost is in the form of heat. The absorption coefficient μ depends on both, tissue characteristics and frequency. Since it is approximately proportional to the frequency, a specific attenuation in dB / (cm · MHz) can be specified [Oppelt 2011]. Scattering and absorption are the major factors of sound attenuation. Typical US field parameters for selected materials are listet in **Table 1**.

Table 1: Sound-specific characteristics of tissues and fluids present in the oral cavity ([Vollborn 2017] after [Duck 2012; Culjat et al. 2010])

Medium	Density	Speed of sound	Acoustic impedance	Acoustic attenuation
	ρ kg/m³	c m/s	Z kN s/m³	$\propto$ dB/(cm MHz)
Water (37°C)	993	1556	1545	0.0022
Blood	1030	1584	1679	0.2
Saliva (like water)	993	1556	1545	0.0022
Gingiva	1043	1561	1628	0.54
Dentin	2900	3800	8000	80
Enamel	2100	5700	16500	120

Image Formation

Each signal received by the transducer represents a superposition of sound waves reflected at tissue boundaries in the scan line. For the transfer and storage of signals, an alternating electrical voltage is advantageous. In the case of ultrasound technology, this is implemented in the conversion of acoustic to electrical (radio frequency RF) signals by means of a piezoelectric element in the transducer. The information is thus contained in the continuous change of voltage over time. The time function of the voltage *u(t)* describes the relationship of the dependent variable *u* to the independent variable *t* [Werner 2009]. During a scan, a fixed number of signals are recorded per slice. In order to avoid a superposition of these signals, a defined time delay is required before a new sound pulse is emitted. Between two pulses a resulting signal is recorded. The low-voltage signals are amplified by means of a variable controlled amplifier (VCA). Their configured gain profile is a function of sample time as signal strength decreases over time due to attenuation of the acoustic energy [Murtaza et al. 2008]. Then, the analog input signals are transformed into a digital data stream by means of an analog-to-digital converter (ADC). The selected sampling frequency f_s should be at least twice the maximum possible frequency f_{max} in the band-limited input signal in order to enable discretization withouth any data loss (Nyquist-Shannon-Theorem) [Deserno 2011]. Commonly, the ADC sampling rate equals four times or more than the transducer center frequency [Murtaza et al. 2008] and is set to $f_s = 400$ MHz for this HFUS microscanner. After digitization, several processing steps are applied to each scan line, including filtering, envelope detection, and grayscale coding of discrete-time numerical signals. For **filtering**, typically a bandpass filter is used to reduce frequency dependent noise. It also offers the opportunity to choose between imaging based on the fundamental frequency (conventional imaging) or based on the second harmonic frequency (harmonic imaging, see section **2.5.2**) [Murtaza et al. 2008]. Harmonics are multiples of the incident carrier frequency f_c [Schlottmann 2001]. Ultrasound imaging typically operates non-coherently on the **envelope** of the signal. This process is called demodulation or detection. The Hilbert transformation results in an analytical representation of the signal. It is independent of the frequency and imaging modality (conventional or harmonical), or changes in the center frequency over time [Murtaza et al. 2008]. The obtained demodulated signal can be displayed as a function of time (Amplitude Modulation or A-Mode (see **Figure 13**)) and converted into a depth axis (z-coordinate) with the relation:

$$z = \frac{c \cdot t}{2} \qquad\qquad 2.4$$

where *t* is the time of flight. Each sample represents an amplitude value that corresponds to the strength of reflection. In addition to the A-Mode visualization, the Brightness Modulation (or B-Mode) is also used as a typical presentation method in medical sonography. For B-Mode imaging, echo-signals recorded along a line are combined. By means of **grayscale coding**, each sample amplitude is assigned to a specific brightness value. Thus, a 2D cross-sectional presentation of the image plane can be generated [Deserno 2011]. Due to linkage of several slices, a 3D representation can be achieved. The position sensor can assign a precise location (x, y coordinates) to the respective signal. For a good representation in A-Mode and B-Mode, the correct gain settings of both the basic gain and the depth gain are required [Burckhardt 1993].
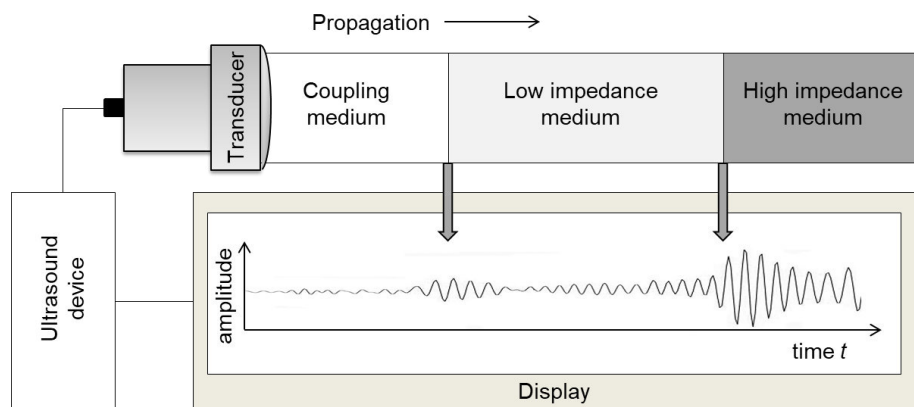

Figure 13: Schematic representation of the puls-echo-method (m.f. [Vollborn 2017])

Advanced Data Processing

Drawback of the strongly focused single-element transducer is the limited depth of field. This causes a poor resolution outside the focus. To overcome this drawback, Passmann and Ermert [Passmann & Ermert 1996] introduced the synthetic aperture focusing technique based on a virtual point source (VSAFT). The focus point of the transducer is considered to be an ideal virtual point source (VPS) of acoustic radiation. While moving the transducer in lateral direction, the reflection of one point may be captured at different positions. Thus, a depth-independent resolution can be achieved by using a delay and sum principle taking the time of flight into account in order to reconstruct the responses of every point of interest (see **Figure 14**). Important parameters of the coupling medium and transducer (speed of sound, aperture diameter, focus length) are included. Chuembou Pekam et al. showed that the VSAFT method can be used to improve the spatial resolution and to increase the signal-to-noise ratio (SNR) in HFUS imaging of tooth surfaces [Chuembou Pekam et al. 2012; Chuembou Pekam et al. 2011; Chuembou Pekam et al. 2015].

Weak reflections of certain tooth surface points (i.e., lateral tooth side walls) are another challenge of the scanner concept. Following the assumption that maximum reflection occurs at
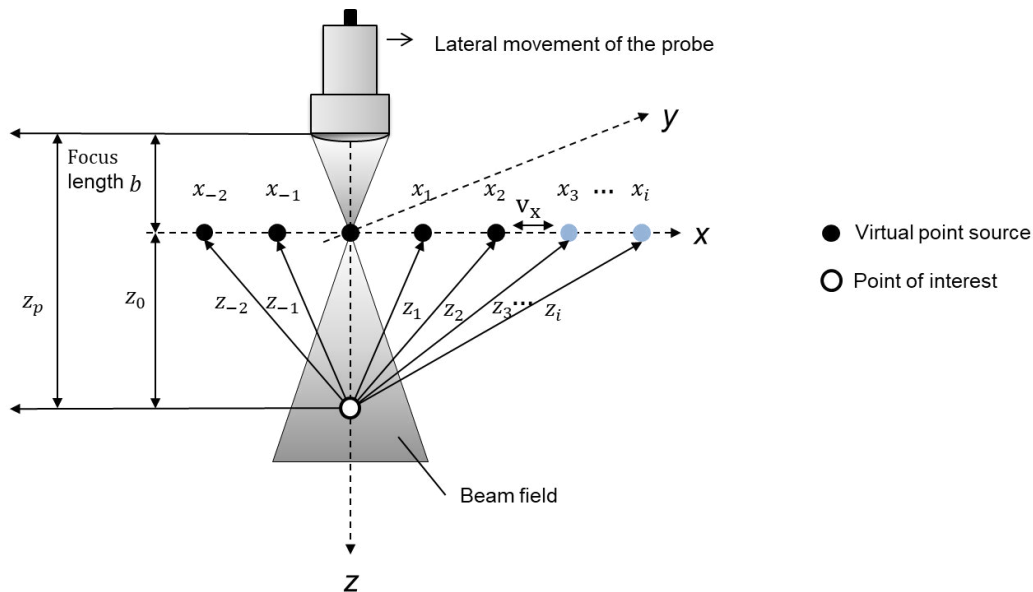

Figure 14: Principle of the delay and sum method based on a virtual point source (m.f. [Chuembou Pekam et al. 2012])

the interface to enamel, a 3D point cloud of the prepared tooth is created by determining the coordinates of the maximum in each A-mode scan line. The surface reconstruction can thus be influenced by noise, measurement errors or data gaps. Also, the low sensitivity to angular aligned specular reflectors is problematic. An improvement in the surface reconstruction could be achieved by superimposing the image data from different imaging angles (sparse spatial compounding (SSC)) [Heger et al. 2011]. However, this required a change in the probe kinematics from 2- to 4-DOF (2 translational and 2 rotational) as well as additional recording operations, which significantly increased both the scanning time and the data processing effort. Therefore, missing surface points are estimated using the *thin plate spline robust point matching* (TPS-RPM) [Chui & Rangarajan 2003] algorithm which is a non-rigid approach to find the optimal mapping between two sets of features. The implementation requires an initial deformable model which is based on a segmented data set. Therefore, demodulation to base-band, linear grayscale coding and threshold-based maxima detection are applied to the original data set in order to separate tooth surface echoes (TSE) for point cloud generation. By means of a linear interpolation in each 2D slice of the 3D point cloud, the density and homogeneity of the initial point cloud is increased. Also, large data gaps (i.e., > 1 mm) on the lateral tooth surface are closed by adding intermediate points due to linear interpolation. By approximating the interpolated tooth contour using a polynomial fit, a corresponding

segmentation model is created for each linear interpolated data slice. Both the so-generated initial segmentation model and the threshold-segmented A-mode data set are used to automatically reconstruct the tooth surface with the TPS-RPM approach. Using an elastic transformation, missing surface data were estimated, whereas the best fit of the deformable model with the original data set was found under the condition of lowest energy consumption. Chuembou Pekam *et al.* demonstrated that the 2D TPS-RPM approach copes with information gaps and outliers, and is thus suitable for the surface resconstruction of prepared teeth [Chuembou et al. 2014; Chuembou Pekam et al. 2015]. Afterwards, the acquired point cloud is meshed to a surface model by *standard triangulation language* (STL). The worflow of the HFUS-based tooth surface reconstruction is shown in **Figure 15**.
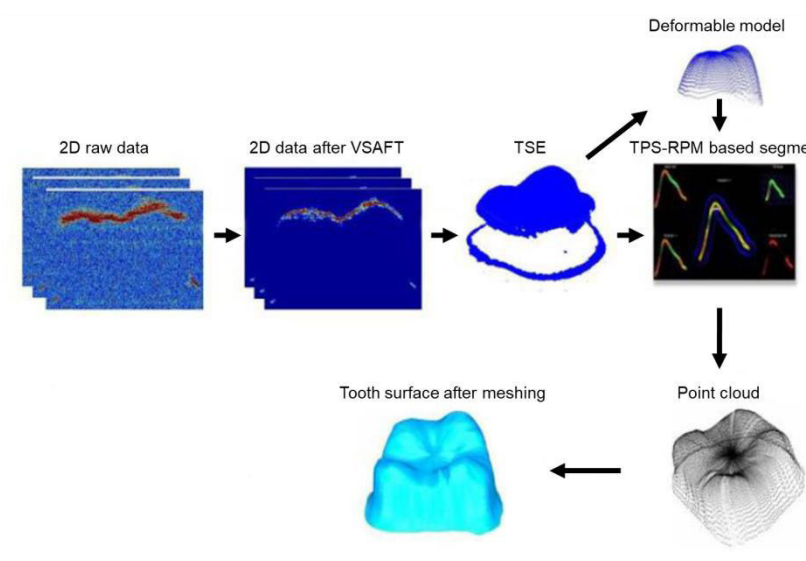

Figure 15: Workflow of the HFUS-based tooth surface reconstruction (m.f. [Chuembou et al. 2014])

2.3 Ultrasound Image Artifacts

Due to its low cost and simple as well as painless application, medical sonography is often the prefered imaging modality. However, it is also accompanied by image artifacts that are commonly encountered in clinical practice [Barr et al. 2013]. Image artifacts are any irregularities or distortions that falsely represent structures to be imaged [Kremkau & Taylor 1986]. They can, for example, occur as added or missing objects, or as a displacement of the real structure´s location. Also, they may reflect the wrong brightness, size or shape. Thus, they present a major drawback of this technique as they may aid in diagnosis. Some of these artifacts are clearly visible in B-mode images; others may be merged with variant structures

and are difficult to be noticed. Hence, recognizing them when they occur is an important first step in medical sonography that is usually done by experienced radiologists. Image artifacts originate at different points in the process chain of the imaging procedure and can be roughly divided into three groups: artifacts that are controllable prior to or during the imaging acquisition [Kirberger 1995]; artifacts of acoustic origin [Kremkau & Taylor 1986]; and artifacts that occur during image processing [Nelson et al. 2000].

2.3.1 Artifacts controllable prior or during image acquisition

Artifacts controllable prior or during image acquisition may be environmental or operator/patient induced and arise secondary to an improper scanner design or an improper scanning technique. This includes electrical interference with other electric devices or radio-frequency signals, patient preparation, as well as patient movement [Kirberger 1995]. US devices tend to be susceptible to electrical interference in the frequency range used by the equipment. Such interference may be displayed as repetitive lines or background noise in B-mode images [Kaeley & Wakefield 2010]. Furthermore, in addition to a suitable distance between the transducer and tooth surface, as well as the intraoral temperature as an influencing factor on the speed of sound c, those artifacts also involve the inclusion of air and other foreign bodies. Air bubbles in the sound path result in an attenuation of the sound amplitude [Meyer & Skudrzyk 1953]. Especially when a water-like couple medium is used, total reflection can occur at water-air interfaces which then may lead to artifacts or a loss of information from structures posterior to the gas bubble. Hence, the intraoral interface must remain free of trapped air for the duration of data acquisition. This requires a verification of the measurement volume on the side of the dentist. Also, it must be ensured that no other foreign bodies such as particles from the tooth preparation or other sound-resistant components occur that may cause artifact formation. In B-mode and C-mode images, artifacts caused by air bubbles in the sonic field can be seen as slightly curved lines and quasi-circular objects, respectively (see **Figure 16**). The C-mode image plane is normal to the B-mode plane. Presented data were acquired *in vivo* using the HFUS microscanner. The transducer was positioned parallel to the tooth´s side wall. The demonstrated artifacts caused by air bubbles located close to the tooth surface may be mistaken as dental substance in the reconstruction process. As with other imaging techniques, e.g., MRI [Zaitsev et al. 2015] or CT [Boas & Fleischmann 2012], patient motion is expected during the scanning procedure. While blood flow provides useful information in Doppler ultrasound [Hoskins 1990], bulk motion in static imaging can be troublesome. The influence of movement relative to the probe was investigated in [Vollborn 2017]. Potential factors include natural breathing, muscle tremors, throat clearing,

swallowing, tongue or mandible movements, coughing or sneezing, as well as varying fixation forces of the patient´s bite. Expected consequences are acceleration of the system or a shift of the scanner head to the tooth structure. Thus, patient motion may lead to misregistration artifacts which may be displayed as blurring or as a straight line in the radiographic image [Park et al. 1981] and thus result in a quality reduction of the 3D-surface reconstruction. As acquisition time becomes significant, the probability of movement during data collection increases.
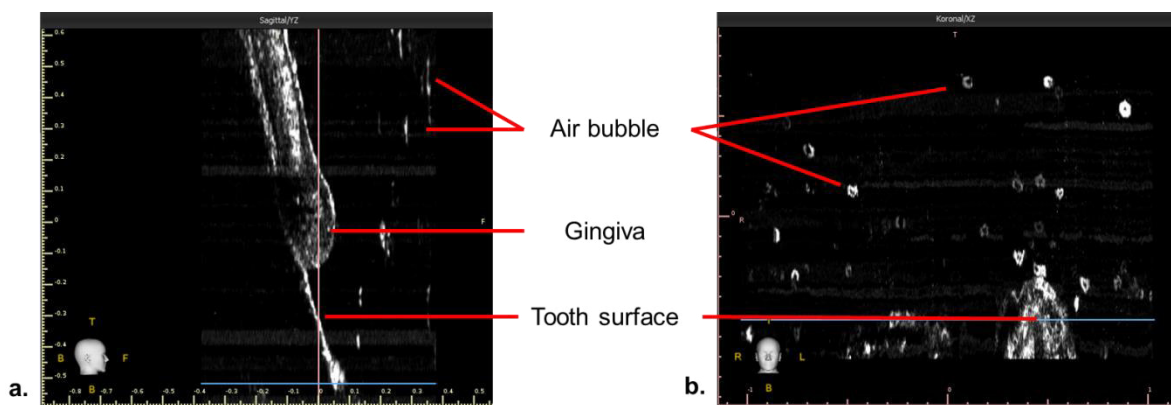

Figure 16: a. Saggital section of a human premolar *in vivo* (B-mode tilted to the right for presentation); **b.** Coronal section of human premolar *in vivo* (C-mode)

2.3.2 Artifacts of acoustic origin

The origin of image artifacts of acoustic origin is well-studied. Most artifacts to occur are of this nature. In order to better understand their formation one must consider the physical properties of the ultrasound pulse formation, the sound propagation in matter and its interactions with tissue, as well as the assumptions made during signal processing by the ultrasound device [Feldman et al. 2009]. Acoustic artifacts occur in particular when these assumptions are incorrect or simplified. They include that an ultrasound beam and echoe travels in straight lines, a detected echoe originates from objects on the transducer main axis and after a single reflection, a constant speed of sound in human tissue is given, and the acoustic energy in an ultrasonic field is uniformly attenuated. In clinical practice these assumptions are often not maintained which favors the errroneously display of echoes. In literature, artifacts of acoustic origin related to B-mode mostly are classified based on resolution, propagation, and attenuation. The most common acoustic artifacts found in literature are listed in **Figure 17**, classified as they are considered in [Kremkau & Taylor 1986]. Artifacts regularly recognized in tooth visualization are highlighted.

In radiology, spatial resolution denotes the abilty of an imaging modality to distinguish between two adjacent objects. Due to poor spatial resolution, closely spaced objects may appear merged together or small objects are displayed magnified. It can be differentiated between
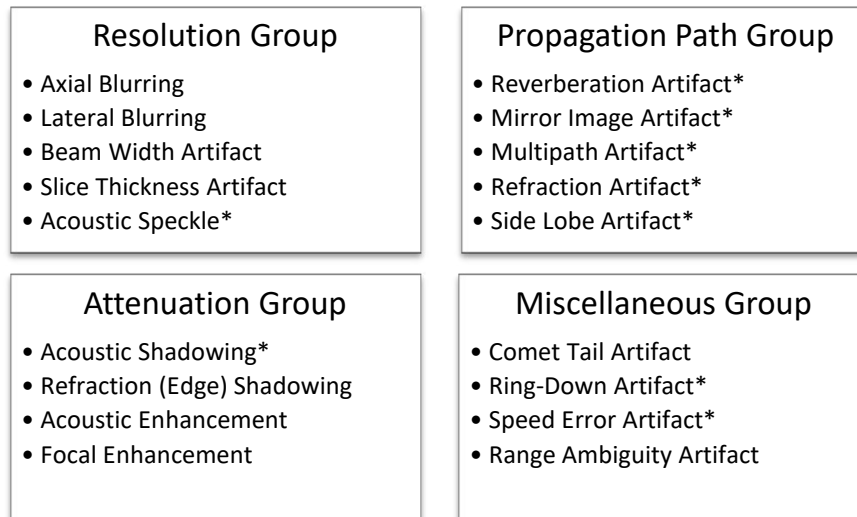
Resolution Group	Propagation Path Group
• Axial Blurring • Lateral Blurring • Beam Width Artifact • Slice Thickness Artifact • Acoustic Speckle*	• Reverberation Artifact* • Mirror Image Artifact* • Multipath Artifact* • Refraction Artifact* • Side Lobe Artifact*
Attenuation Group	Miscellaneous Group
• Acoustic Shadowing* • Refraction (Edge) Shadowing • Acoustic Enhancement • Focal Enhancement	• Comet Tail Artifact • Ring-Down Artifact* • Speed Error Artifact* • Range Ambiguity Artifact

Figure 17: Common B-Mode US image artifacts of acoustic origin found in medical sonography

axial, lateral and elevational resolution in the 3D space. **Figure 18** illustrates an ultrasound field in 3D space produced by a single-element transducer with a mechanically fixed focus. Direction of resolution components are highlighted by arrows.
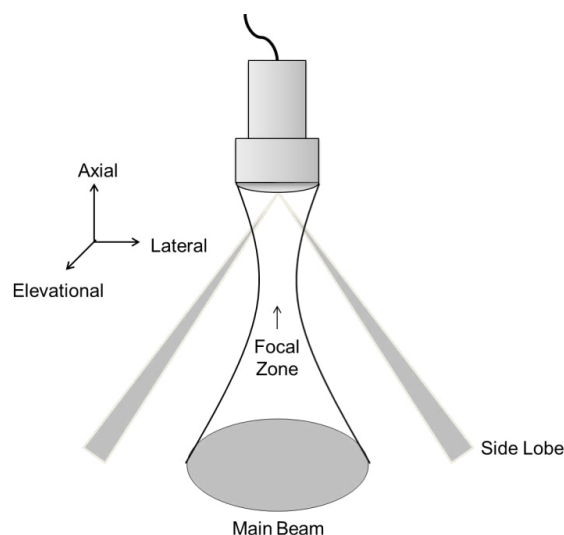

Figure 18: Ultrasound field of a single-element transducer with a mechanically fixed focus

Axial (or longitudinal) resolution is defined as minimal distance that can be differentiated between structures in the course of US waves. It corresponds to half the spatial puls length

and thus is frequency dependent. Axial resolution is high if spatial pulse length is low. Lateral resolution is reffered to the minimum distance that can be differentiated between structures perpendicular to the direction of the US beam. It is equal to the pulse width and thus varies with depth being greatest in the focal region as the beam converges to its narrowest width [Kremkau & Taylor 1986]. Elevational resolution is related to the beam thickness. However, as a single-element transducer is used in the HFUS-assisted microscanner, lateral resolution is used synonymously in this thesis. Artifacts related to spatial resolution are strongly dependent on characteristics of the sonic probe and might remain unnoticed if the exact geometry of the tooth is unknown. At this point, the VSAFT processing approach, which simulates a depth-independent focusing, is already used to counteract the decrease in lateral resolution with depth. Also, lateral blurring can be minimized or prevented completely by recording the region of interest (ROI) (e.g. occlusal tooth surface) in the focal zone.
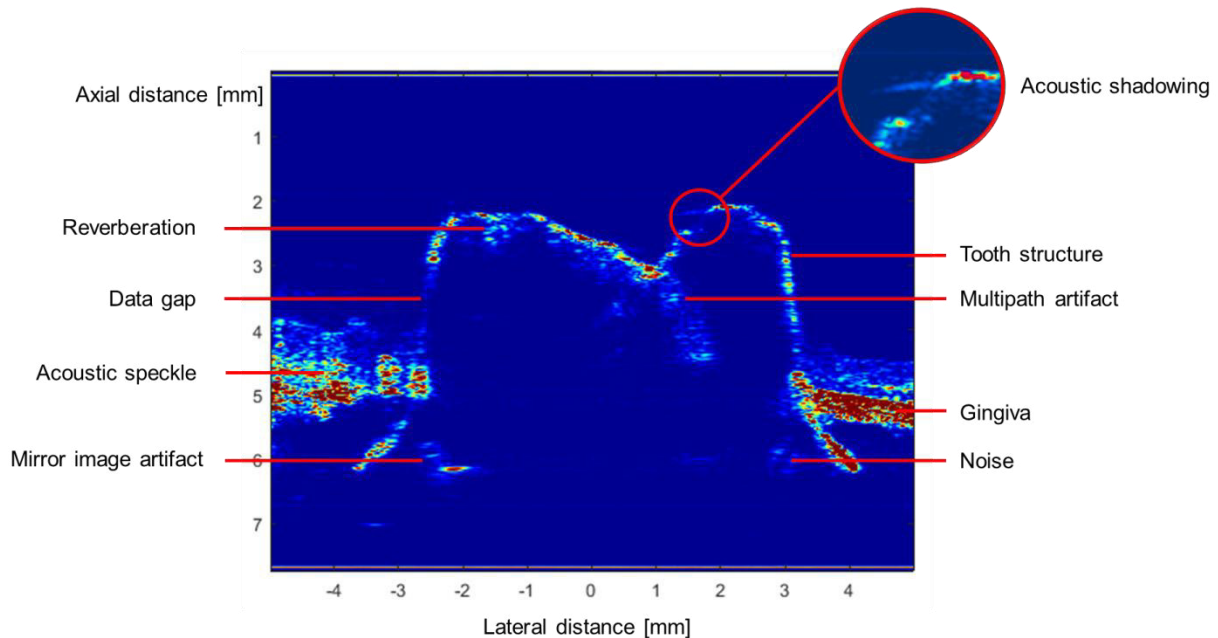

Figure 19: Examples for image artifacts found in B-Mode image of a molar after VSAFT processing

Figure 19 shows a cross-sectional (B-mode) image of a human molar surrounded by porcine gingiva. The specimen was provided for research purposes and a chamfer preparation was performed. A subgingival preparation margin is simulated. Data were acquired *in vitro* using the HFUS microscanner at 50 MHz, and VSAFT processing was applied. Several artifacts are displayed within the image. Acoustic speckle is assumed to be seen as regions of granular appearance in the acquired B-Mode images. The artifact is displayed as multiplicative noise and represents a major source of image quality degradation in medical sonography where several soft tissues are present [Kremkau & Taylor 1986]. In general, speckle is characterized

by a textural pattern that varies depending on the type of tissue. It is closely associated with parenchymal tissue which represents an aggregate of point scatterers. Physical factors such as reflector surface roughness, complex intervening media with multiple interfaces and differing acoustic velocities favour acoustic speckle [Kirberger 1995]. In acquired B-mode images of the HFUS microscanner speckle noise can in particular be observed in areas of gingival tissue. One assumption made by the US device is defined as a uniformly attenuated ultrasonic field during signal acquisition. As the brightness of a structure depends on its depth, and the echogenicity of other objects in the sound path, attenuation errors may occur. Adjacent parts of the same objects may show different intensities posterior to the structure and may be displayed as areas of anechogenicity or enhancement. In **Figure 19**, acoustic shadowing is displayed as an anechoic zone deep to a structure (e.g., air bubble) that points vertically away from the edge of the tooth. Thus, visualization of the expected tooth´s surface is prevented resulting in a data gap of the outline. Acoustic shadowing is characterized by a sound void expanding from a media boundary in case of complete reflection or absorption of the sound beam (see **Figure 20**). In medical sonography, shadowing commonly occurs in the presensence of bone, gas or calculi. Thereby, the acoustic shadows differ according to the physical properties of the reflector: Posterior to bone or calculi, for instance, clear shadows occur due to the high percentage of reflection and absorption with no transmission. In contrast, light reverberation artifacts may be displayed within the shadowed area distal to gas collections when virtually total sound reflections at tissue-air interfaces result in artifactual echoes [Sommer & Taylor 1980]. If the reflector is small in diameter compared to the incident beam width, shadows may not be visible. In diagnostic sonography, acoustic shadowing is also considered as beneficial artifact since it may offer differentiation of structure characteristics.
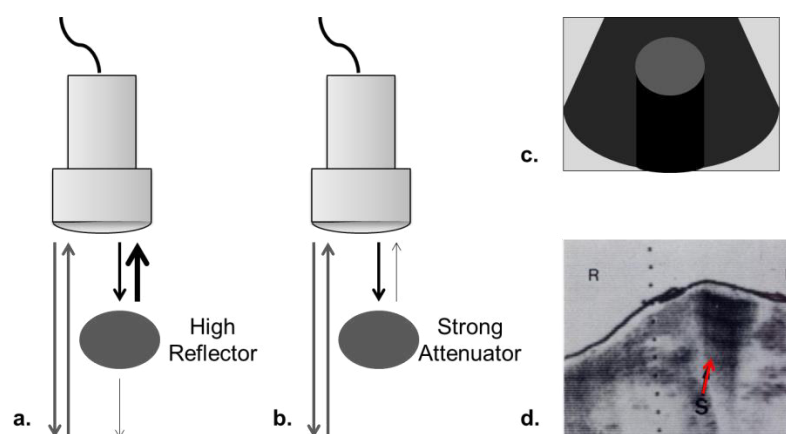

Figure 20: Acoustic shadowing a. due to a high reflector, or **b.** due to a strong attenuator in the sound path. **c.** An anechoic region is displayed posterior to the structure. **d.** Transverse scan of a gas-containing abdominal wall abscess. Shadowing is marked by an arrow (m.a. [Kressel & Filly 1978]).

Due to the high reflection coefficient at the interface between couple medium and tooth, it is to be expected that no structures can be detected below the tooth surface. However, the B-mode image shows different regions that are determined by noise. Defining noise as an unwanted signal, several observations can be made in the presented image. Echoes that undergo several reflections during their propagation are misinterpreted by the ultrasound device (e.g., reverberation artifact, mirror image artifact, or multipath artifact). Close to the occlusal plane of the left dental cusp, equidistal vertical lines may represent reverberation. The reverberation artifact occurs when an ultrasound beam strikes two strong parallel reflectors. The beam reflects back and forth between the two interfaces taking a longer time to return to the transducer. Thus, the detected echoes are misinterpreted as originating from deeper structures [Scanlan 1991]. Structures affected by reverberation are displayed as multiple equidistantly spaced reflections, but may appear smaller due to attenuation. They are more likely to occur if the interface is located close to the transducer. **Figure 21** demonstrates the principle.
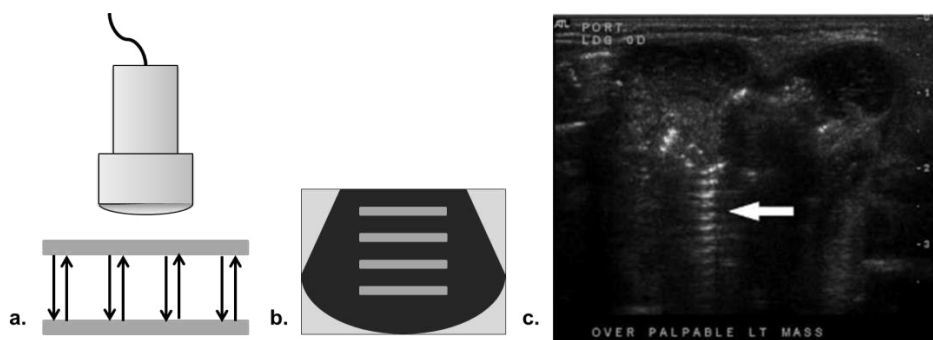

Figure 21: Reverberation artifact. a. Acoustic waves are repeatedly reflected between two strong reflecting interfaces. **b.** Multiple equidistal echoes posterior to the interfaces are displayed in a B-mode image. **c.** A reverberation artifact marked by the white arrow in a US B-mode image of palpable mass in a neonate [Feldman et al. 2009].

A reverberation between the transducer and an acoustic interface is also possible. In case of the HFUS microscanner, reverberation artifacts are especially seen as multiple reflections between the transducer and acoustic window that seperates the outer an inner coupling area (see **Figure 22**). In the point cloud, equidistal vertical lines can be observed forming a plane that represents the reverberation artifact. Due to the algorithm creating the point cloud by means of threshold-based maxima detection (see **2.2.3**), the artifact is less prominent at regions where a posterior high density of points representing the tooth surface exists. As the acoustic window cannot be located at the level of the tooth, this can be clearly be identified as a reverberation artifact.
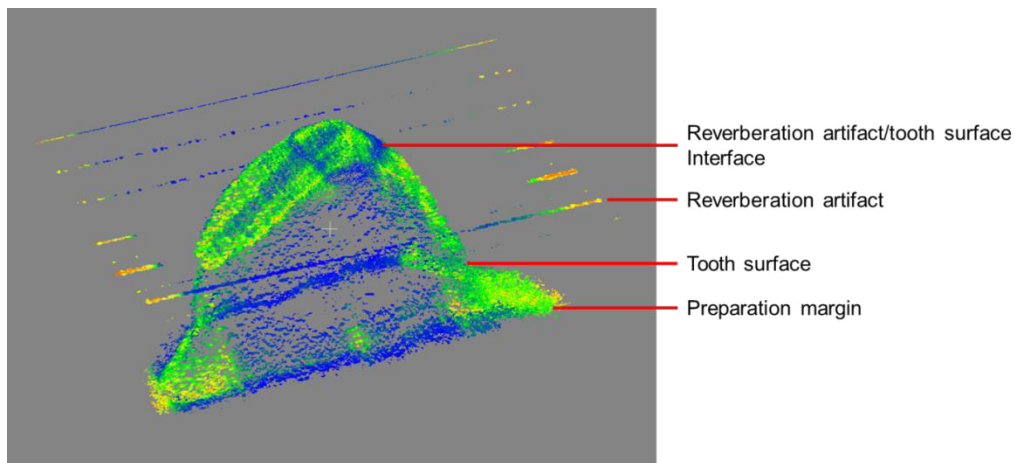
Figure 22: a. 3D Point Cloud of a human premolar with reverberation artifact; **b.** Corresponding B-mode image

As the name implies, the mirror image artifact is displayed as an inverted duplication posterior to a reflecting structure (see **Figure 23**). When sound waves are scattered at a highly reflective and curved (specular) surface some echoes do not return directly to the transducer but rather encounter another structure. They are then reflected back to the highly reflective surface and back to the transducer. In medical sonography, this artifact is commonly observed at the diaphragm with the pleural-air interface as strong reflector [Feldman et al. 2009]. Due to the enlongered time of duration, the second reflecting structure is assumed to be located in the deeper sound field. Here, the curving tooth surface may function as the first strong reflecting medium and the gingival tissue as the second reflector.
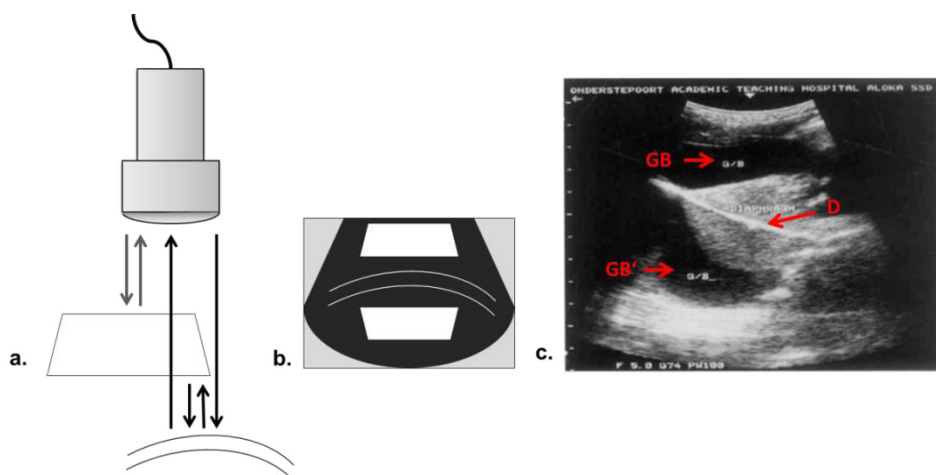
Figure 23: Mirror Image Artifact. a. A sound pulse is reflected at a highly reflective curved object, encounters a second reflective structure, and hits the first object again before it propagates back to the transducer. **b.** The second structure is displayed as an inversely duplicated object posterior to the first curved structure. **c.** Parasagittal cranial abdominal canine ultrasonogram with mirror image of liver and gall bladder (GB and GB') visible beyond the diaphragm (D) (m.a. [Kirberger 1995]).

Another form of this multi path mechanism is the multipath artifact itself. A specular reflector is insonated at an oblique angle causing the sound wave to divert into another direction. The propagating sound wave may encounter another reflector in its path and may be redirected to the transducer for detection [Kirberger 1995]. In contrast to the mirror image artifact, the paths to and from a reflector differ (see **Figure 24**). Due to the elongered time of flight of the traveling sound signal an axial error in reflector positioning occurs. The multipath artifact is commonly difficult to identify but may be the reason for the noise displayed posterior to the right dental cup in **Figure 19**.
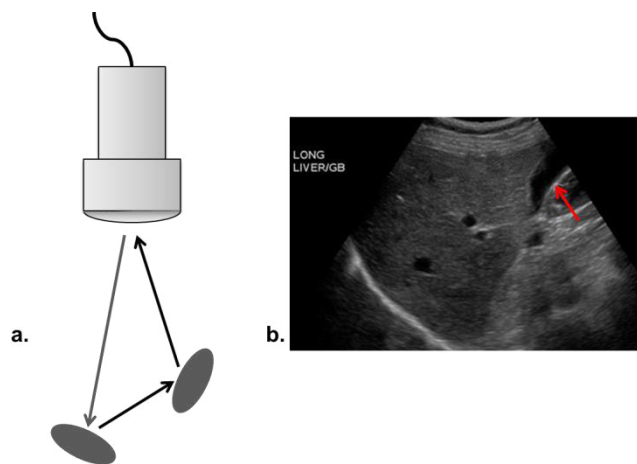

Figure 24: Multipath artifact. **a.** An echo encounters a second reflecting structure before it is propagated back to the transducer. **b**. B-mode image of the liver in which small dots within the lumen of the gallbladder represent a multipath artifact [Wicks 2013].

If an ultrasound beam strikes a reflective tissue boundary at an oblique angle the incident acoustic wave changes direction. The degree of change in direction is dependent on both the angle of the incident sound beam and the difference in the speed of sound c_1 and c_2 between two materials. Snell´s law (see **2.5**) describes the relationship between the angles of incidence θ_i and refraction θ_r at a single frequency wave [Tipler & Mosca 2009]. In general, the incident wave is partially refracted and partially reflected.

$$\frac{sin\theta_r}{sin\theta_i} = \frac{c_2}{c_1} \qquad\qquad 2.5$$

A refracted portion may be reflected off at an interface causing an echo to return to the transducer. Due to the assumption of a straight beam path, perceived echoes may be misplaced to the side of their true location. Thus, structures may be displayed wider or an apparent duplication may appear. This is refered to as refraction artifact. As with the multipath artifact, echo misinterpretation due to refraction is difficult to identify and could not be clearly

recognized in images investigated during this thesis. However, considering the strong difference in the speed of sound in tooth and ultrasonic couple medium as well as the rough surface of the prepared tooth, it is assumed that this artifact is very likely to occur at some point. Some noisy regions cannot be clearly classified as a particular artifact by observing a single B-mode image and thus require an assessment of adjacent slices. Also, they may be caused by objects not located on the main beam axis. When generating acoustic energy at the piezoelectric crystal, secondary beams occur due to radial expansion and contraction of the crystal. They spread from the sensor at angles other than the main beam and are refered to as grating and side lobes (see **Figure 18**). Grating lobes are often associated to phased-array transducers while side lobes can also be created by a single-element probe [Olympus IMS 2007]. The main beam has the greatest acoustic energy and is essentially involved in the imaging process. Even though the energy of side lobes is much lesser, the system becomes error prone to artifacts. If a strong reflector is located in the low-energy off-axis beams the structure is displayed as originating from within in the central beam [Laing & Kurtz 1982]. Side lobes are also involved in the reduction of the SNR in US images [Jong et al. 1985]. Again, it is a challenging task to recognize and identify this type of artifact. However, as a strong reflector such as an air bubble is located in close proximity, it may appear.
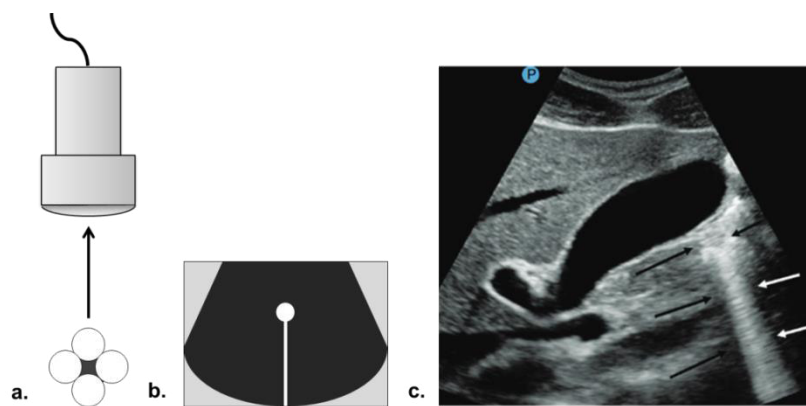

Figure 25: Ring-down artifact **a.** Resonant vibration causes a continuous sound echo; **b.** Illustration of the ring-down artifact; **c.** Ring-down artifact [Kirberger 1995].

The ring-down artifact often has a similar appearance to the reverberation artifact with closely spaced multiples, but evolves due to a completely different process. When an US beam strikes small gas bubbles or a fluid that is trapped between a tetrahedron of gas bubbles, the transmitted US energy causes the structure to vibrate. These resonant vibrations produce a continuous sound wave that is perceived by the transducer [Kirberger 1995]. Hence, the ring-down artifact is displayed as a line or series of parallel band extending from a gas collection

(see **Figure 25**). As bubbles are present in the coupling medium, they may form this construct. However, as several factors have to be fulfilled to make a bubble resonating to an incident sound beam, it is unlikely to be observed at high frequencies used by the microscanner during insonification of bubbles of the dimensions present. In conventional ultrasongraphy, a constant speed of sound in biological tissue is assumed as 1540 m/s. When an acoustic beam travels through a medium with a velocity significantly slower, an echo will take longer to return to the transducer. Thus, echoes are displayed deeper in the image (see **Figure 26**) [Kremkau & Taylor 1986]. This so-called speed error artifact or speed displacement artifact is commonly recognized when an ultrasonic beam encounters an area of focal fat where the sound speed is about 1450 m/s [Nyland & Mattoon 2002]. As present air may also reduce the speed of sound significantly during wave propagation, a displacement may occur in case of the microscanner. If the real propagation velocity is significantly higher than the presumed, the reflector appears shallow.
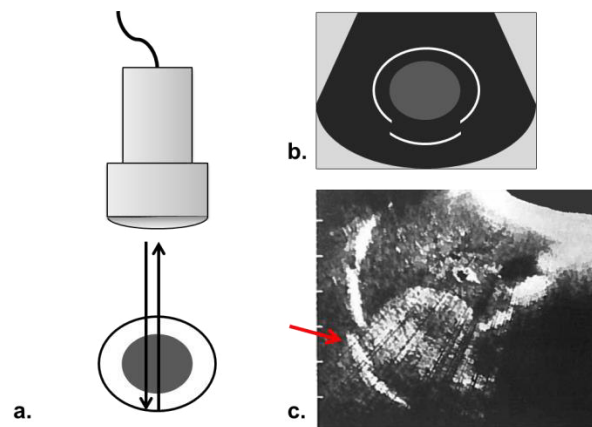

Figure 26: Speed error artifact. a. The acoustic wave encounters a structure of lower speed of sound than assumed before it strikes another reflector. b. The reflector is displayed as located deeper in the ultrasonic field. c. Displacement of the distal diaphragm posterior to an adrenal myetolipoma [Kremkau & Taylor 1986]

2.3.3 Artifacts that occur during image processing

The most straight forward way to obtain volumetric US image data (90° x 90°) is done by aligning adjacent 2D US slices. In this way, 3D US imaging is prone to the same type of artifacts as 2D US imaging as well as others that are unique to volume acquisition and data rendering [Nelson et al. 2000]. If the distance between adjacent slices is non-uniformly, a simple alignment may not accurately represent the dimensions of the structures. Thus, position information is used to register scan planes to the volume. Resolution of the ultrasound image is not necessarily isotropic in axial (in depth), lateral (side-to-side) or elevational (beam

thickness) direction [Nelson et al. 2000]. In case of arbitrary re-slicing of volume data in other orientations, a general degradation in resolution may be seen. Thus, resolution artifacts primarily affect the shape and size of an insonated structure. Also, all artifacts that cause a displacement of the structure within the data generally can result in incorrect identification of location and presence of a structure. This includes, patient motion, all artifacts related to multiple reflections as reverberation, speed error and side lobe artifacts. They result in a distortion of the tooth´s surface during reconstruction. Furthermore, artifacts can also appear through processing steps (e.g., during image segmentation). The quality of a rendered image often depends on the choice of rendering parameters such as threshold or filter properties. So, this may result in the loss of significant information.

2.4 Problem Identification and Research Question

In the previous sections the function of the HFUS-assisted mircoscanner and its signal processing are described. By means of data processing, a digital 3D surface model of a prepared tooth can be visualized to serve as a basis for CAD/CAM systems. The achieved resolution in the micrometer range allows a clinically acceptable impression. Despite the advanced data optimization, the surface reconstruction of a prepared tooth can still be affected by artifacts. They present one of the major limitation factors and may be a source of confusion on interpretation. Artifacts can lead to unimageable surface areas and thus may hinder accurate surface reconstruction. In addition, such artifacts are transferred to every subsequent processing step. With the background of high accuracy requirements for a dental restoration, these errors can adversely affect the quality of the final outcome. Therefore, undiserable ultrasound artifacts have to be recognized, identified and avoided or eliminated as such in order to lead to image-quality improvement. It is expected that in a clinical procedure, the intraoral situation may differ from an idealized model. Foreign bodies such as food particles, remaining dental hard tissues after preparation or air bubbles may occur in the sound path presenting potential artifactual sources. However, it is well known that air bubbles in the sound path present a major degradation factor due to strong inhomogeniteis they cause in the coupling medium. As embedded air bubbles may distort sound wave reflection and influence physical parameters such as acoustic penetration depth and speed of sound, they can be a potential source for several artifacts. Also, air bubbles cause artifacts that are displayed as lines or quasi-circles in B-mode and C-mode images, respectively. It is assumed that the tooth surface detection efficiency of the HFUS-assisted intraoral microscanner is sensitive to air inclusions in the gel. Thus, insufficient coupling might be an important factor of a less

satisfactory outcome of a 3D reconstruction of the tooth surface. Air bubbles in the coupling area are a relevant problem in case of the high quality requirements of an intraoral impression for the production of artificial crowns. Although bubble-free coupling is essential, the intraoral coupling zone cannot be visually monitored using the HFUS microscanner. However, bubble-free coupling is difficult to perform.

Objective of this thesis is to develop and evaluate a method that minimizes the influence of air bubbles in the process of tooth surface reconstruction. As a first step, a literature research is performed to understand the effect and behavior of air bubbles during insonification. Afterwards, a requirement analysis is carried out to define parameters of interest. Furthermore, concepts have to be generated and estimated that optimally fulfill the requirements of the method and contribute to a minimization of the mentioned problems. An evaluation of the implemented concept is carried out with the help of a reference model. As part of this work, following research questions can be defined:

1. What are the physical properties of an air bubble? And how can they be described?

2. How do gas bubbles in an acoustic field behave? And how does this behavior contribute to a feasible detection method?

3. Which parameters for an optimal detection method can be determined?

4. What are constructive methods for the detection of occuring air bubbles?

5. Can the selected method be applied to *in vitro* and *in vivo* data?

2.5 Physical properties of air bubbles

Gas bubbles are ubiquitous in daily life such as carbonated water or foam. Nevertheless, the physical properties of this structure are rarely considered. A bubble may generally be described as a matter-surrounded cavity filled with a gas. In the present system, it is assumed that this gas is ambient air. The surrounding substance is given by a water-based ultrasonic gel. In the following two sections, the physical characteristics of an air bubble are described. It is differentiated between general properties such as shape, and the acoustical behavoir of air bubbles in the sound path.

2.5.1 General physical properties

In literature, the shape of a bubble is mostly described as spherical or quasi-spherical. This is due to the tendency of a structure to minimize the surface tension and is justified by the Young-Laplace formula. Compared to other 3D shapes of the same volume, the surface of a sphere is the lowest, whereby a maximum stability of this shape is achieved. The Young-Laplace formula describes the relationship between the surface tension γ at the liquid-gas interface, the pressure p and the surface curvature [Laplace 1806]. The curvature is determined by the two main radii of curvature r_1 and r_2.

$$\Delta p = \gamma \left(\frac{1}{r_1} + \frac{1}{r_2} \right) \qquad \text{2.6}$$

Δp is the pressure difference between internal and ambient pressure. In a sphere, the two main axes of curvature match at each point. Thus, the equation for a spherical bubble of radius a in a liquid is

$$\Delta p = \frac{2 * \gamma}{a} \qquad \text{2.7}$$

The pressure is thus greater, the smaller the radius of a spheric air bubble is. Due to the effect of surface tension, the surface of the bubble seeks to shrink so that an overpressure p arises in the bubble. Nevertheless, it is well known than only small bubbles are spherical. Larger bubbles may become various shapes. Beside the sphere, ellipsoides and spherical caps are found in literature [Haberman & Morton 1953]. Considering an ellipsoid-shaped air inclusion, the following mathematical descriptions can be made. An ellipsoid´s volume V_E can be defined as

$$V_E = \frac{4}{3} \pi \, abc \qquad \text{2.8}$$

where $a,\ b,$ and c are the semi-axes of the ellipsoid (see **Figure 27**).
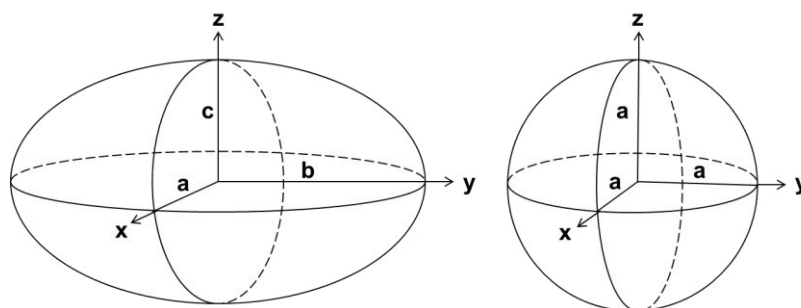

Figure 27: left. Ellipsoid with semi-axes $a, b,$ and c. **right.** Sphere with radius a.

For simplicity, an ellipsoid of revolution with $a = b$ is assumed to determine the surface area S_E. Thus, for an oblate ellipsoid where $a > c$ it is

$$S_{oblate} = 2\pi a \left(a + \frac{c^2}{\sqrt{a^2 - c^2}} \text{arsinh} \left(\frac{\sqrt{a^2 - c^2}}{c} \right) \right)$$

2.9

and for a prolate ellipsoid where $a < c$

$$S_{prolate} = 2\pi a \left(a + \frac{c^2}{\sqrt{c^2 - a^2}} \arcsin \left(\frac{\sqrt{c^2 - a^2}}{c} \right) \right)$$

2.10

A sphere represents a particular case of an ellipsoid, which is true for $a = b = c$. For a spherical bubble with radius a, volume V_S and surface area S_S can be described by equation **2.11** and **2.12**, respectively [Papula 2009].

$$V_S = \frac{4}{3}\pi a^3$$

2.11

$$S_S = 4\pi a^2$$

2.12

2.5.2 Behavior of Gas Bubbles in an Acoustic Field

In general, a structure may be detected using ultrasound due to scattering, absorption, and change in speed of sound if the acoustical characteristics of the structure vary from those of their environmental medium (see pulse-echo method, chapter **2.2.3**). Total acoustical cross-sections for scatter and absorption can be used to describe the effectiveness of sound waves with a body:

$$\sigma_S = \frac{\Pi_S}{I_p}$$

2.13

$$\sigma_A = \frac{\Pi_A}{I_p}$$

2.14

where σ_S and σ_A are the acoustical cross-sections for scatter and absorption, respectively. Π_S and Π_A are the total power scattered and absorbed, respectively. I_p is the incident plane wave intensity [Medwin 1977]. A rigid sphere of radius a can be used for the mathematical descriptions of scattering objects. The acoustical behavior is then differentiated for $ka \gg 1$ or $ka \ll 1$, where k is the wavenumber. $ka \gg 1$ is referred to as geometrical, Kirchhoff or specular scatter [Medwin & Clay 1998]. The Kirchhoff reflection approximation assumes that

the reflections coefficient R (see eq. **2.3**) and transmission coefficient T of an infinite plane wave at an infinite plane interface can be used at every point of a rough surface interface. In the conditions that kR is large and the incident angle θ_i is not close to critical, the spherical wave may then be approximated as a local plane wave. Following this mathematical model, each ray is reflected in such a way that its angle of reflection θ_s is equal to its angle of incidence θ_i (see **Figure 28**) considering the point of reflection to be a tangent plane of the sphere. Diffraction effects are not taken into account. In this model, the scattered power Π_S is then independent of the angle θ_i and all differential geometrical cross-sections are equal.
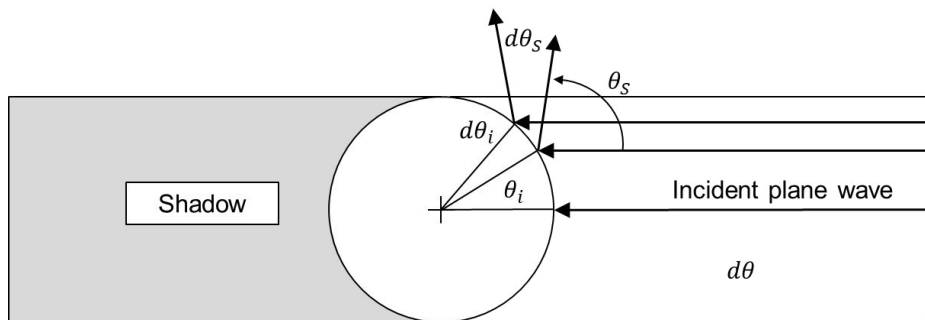
Figure 28: Geometrical scatter from a fixed, rigid sphere at high frequencies for $ka \gg 1$. A shadowing artifact after the scatterer occurs (m.a. [Medwin & Clay 1998])

For $ka \ll 1$, however, the sound wavelength is much greater than the sphere radius and scattering is caused by diffraction only. This scattering is usually referred to as Rayleigh scattering. The acoustical cross-sectional scatter for Rayleigh is smaller than the geometrical cross-section for acoustically small non-resonant bodies as it is for a fixed, incompressible, rigid sphere. In this case, the sound waves bend around the structure and, therefore, are not affected by it. However, a fixed, rigid sphere presents an extreme limit of the physical properties. During insonification, the fluid that fills the sphere determines its acoustical behavior as a scatterer and within its spherical boundaries [Medwin & Clay 1998]. Assuming the gas present in the water-based couple medium to be air, a strong mismatch between air inclusions and couple medium will result in great backscattering. However, if the insonified structure is capable of resonating to an incident sound, the largest detectable effects occur. In literature, various publications dealing with the behavior of gas bubbles in a liquid medium (mostly water) insonified with acoustic energy are found. In most cases the discussions are based on an approximate model limited to a spherically symmetric bubble. A bubble can be determined as a function of pressure and radius (Laplace formula, see eq. **2.6**). The influencing mechanical quantity in the case of sound is (acoustic) pressure [Jenderka 2013]. Stiffness and inertia contribute to resonant mechanical oscillations of a gas bubble. Stiffness is

given by the enclosed volume of gas acting like a spring when the bubble´s equilibrium radius is disturbed. If the bubble radius is small, surface tension becomes significant. Inertia is present due to the liquid´s mass surrounding the bubble and oscillating with it. Insonification of the highly compressible gas bubbles for $ka \ll 1$ by acoustic waves, thus, results in a frequency-dependent volume pulsation that exhibits a unique resonance phenomenon. Resonant bubbles therefore not only behave as a reflector of sound but also as a source. If the initial frequency is at or near the natural frequency of the gas bubble, it will effectively scatter and absorb the sound. The resonance frequency ω_{res} of a pulsating bubble is given by

$$\omega_{res} = \frac{1}{2\pi a} \left\{ \frac{3\kappa P_0}{\rho_\epsilon} \left[1 + \frac{2\gamma}{P_0 a} \left(1 - \frac{\epsilon}{3\kappa} \right) \right] \right\}^{1/2} \qquad \text{2.15}$$

where a is the equilibrium radius of the bubble, P_0 is the static pressure in the liquid, γ is the surface tension of the liquid, κ is the ratio of the specific heats of the gas, ρ is the density of the liquid, and ϵ is a parameter in the range of one to κ dependent on heat conduction in the gas [Nishi 1972]. The resonance frequency is inversely proportional to the radius of the bubble. **Figure 29** shows the resonance frequency versus bubble radius calculated by eq. **2.15** for an air bubble in blood ($\gamma = 60 \ dyn \ cm^{-1}$).
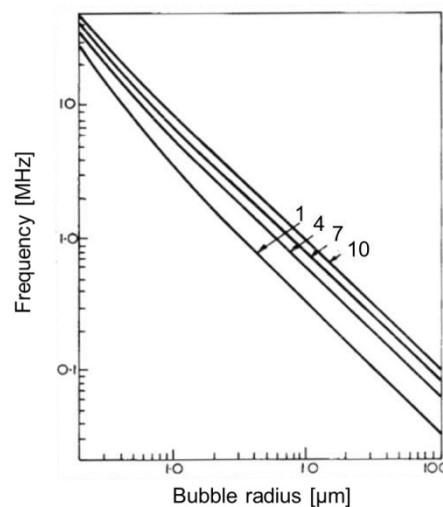

Figure 29: Resonance frequency versus bubble radius for an air bubble in blood for 1, 4, 7 and 10 atm ([Nishi 1972]).

Medwin [Medwin 1977] noted that for bubbles in the radius range of one µm to one mm in water both the scattering and the absorption cross-sections at resonance are a multiple of the geometrical cross-section, and about 10^{10} times that of a rigid sphere of the same radius (see **Figure 30**).
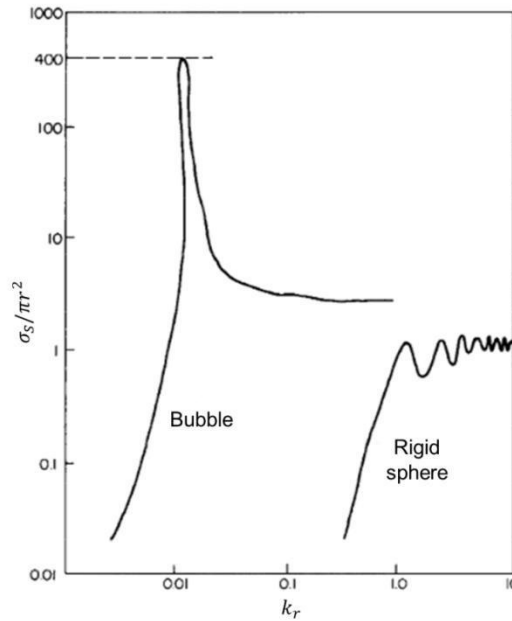
Figure 30: Ratio of total scattering cross-section σ_S to geometrical cross-section for a bubble and a rigid sphere. k is the wave number in water. Resonance peak is calculated for the resonant damping constant $\delta_{res} = 0.1$, which is appropriate for $r \approx 65 \mu m$

Several approximation models for the cross-sectional scattering, absorption and extinction of single bubbles were published. The pioneering derivation edited by Wildt [Wildt 1946] is a widely accepted theory of bubble acoustics. The total scattering cross-section of a small spherical bubble of equilibrium radius a is given by

$$\sigma_S = \frac{4\pi a^2}{((\frac{\omega_{res}}{\omega})^2 - 1)^2 + \delta^2} \qquad 2.16$$

in the limit $ka \ll 1$, where ω_{res} and ω are the radian frequencies of the bubble resonance and the insonating frequency, respectively, and δ is a dimensonless frequency-dependent damping constant. δ is determined by the sum of its components with

$$\delta = \delta_r + \delta_t + \delta_v \qquad 2.17$$

in which δ_r is the frequency-dependent damping constant due to reradiation, δ_t the damping constant due to thermal conductivity, and δ_v the damping constant due to shear viscosity. At resonance, the total cross-sectional scattering for $\omega_{res} = \omega$ becomes

$$\sigma_{S_{res}} = \frac{4\pi a^2}{+\delta_{res}^2} \qquad 2.18$$

36

Thus, the scattering cross-section becomes $4/\delta_{res}^2$ than the geometrical cross-section [Medwin & Clay 1998]. Since the experimental scatter measurements are rather based on backscatter echos than total scattering, a backscattering cross-section (or differential cross-section) for isotropic scattering bubbles is therefore

$$\sigma_{BS} = \frac{\sigma_S}{4\pi} \qquad\qquad 2.19$$

For bubbly mixtures, the attenuation by bubbles is expressed in terms of the extinction cross-section

$$\sigma_E = \sigma_S + \sigma_A \qquad\qquad 2.20$$

that is also given by

$$\sigma_E = \frac{4\,\pi\,a^2\,(\frac{\delta}{k_a})}{((\frac{f_{res}}{f})^2 - 1)^2 + \delta^2} \qquad\qquad 2.21$$

Figure 31 shows σ_S, σ_E, and σ_A for an air bubble in water for a range of radii when insonified by four frequencies. Medwin complemented expected large values of the cross sections at resonance for σ_S and σ_E by large values at $a \gg a_{res}$. However, the absorption cross-sections show the resonance peak only. The cross-sections exhibit a resonance peak when the incident frequency passes through the natural frequency of a bubble and the amplitude of the scattered spherical wave is determined by the amount of damping associated with the bubble´s dynamics. In bubbly liquids where a wide range of bubble radii is present, the bubble density may be taken into account. The total scatter from a bubbly region then depends on the scattering cross section per unit volume. It is to be noted that the approximation stating that only resonant bubbles scatter a given sound field is not rigorous. Thus, in conditions of finite damping, bubbles close to resonance size will contribute. Also, the peak at resonance is only a local maximum. Therefore, bubbles much larger than resonance size can scatter to a greater extent than those of resonance. While the scattering by resonant bubbles is given by the strong coupling with the incident wave resulting in large amplitude of wall pulsation, the pulsation of bubbles much larger than the acoustic wavelength is negligible. In the limit of bubble size, the process then becomes geometrical and acoustic shadows are generated by a bubble due to the high acoustic impedance mismatch [Leighton 1994]. If the bubble is rather an oscillating oblate ellipsoidal bubble than an spherical bubble of the same volume, the
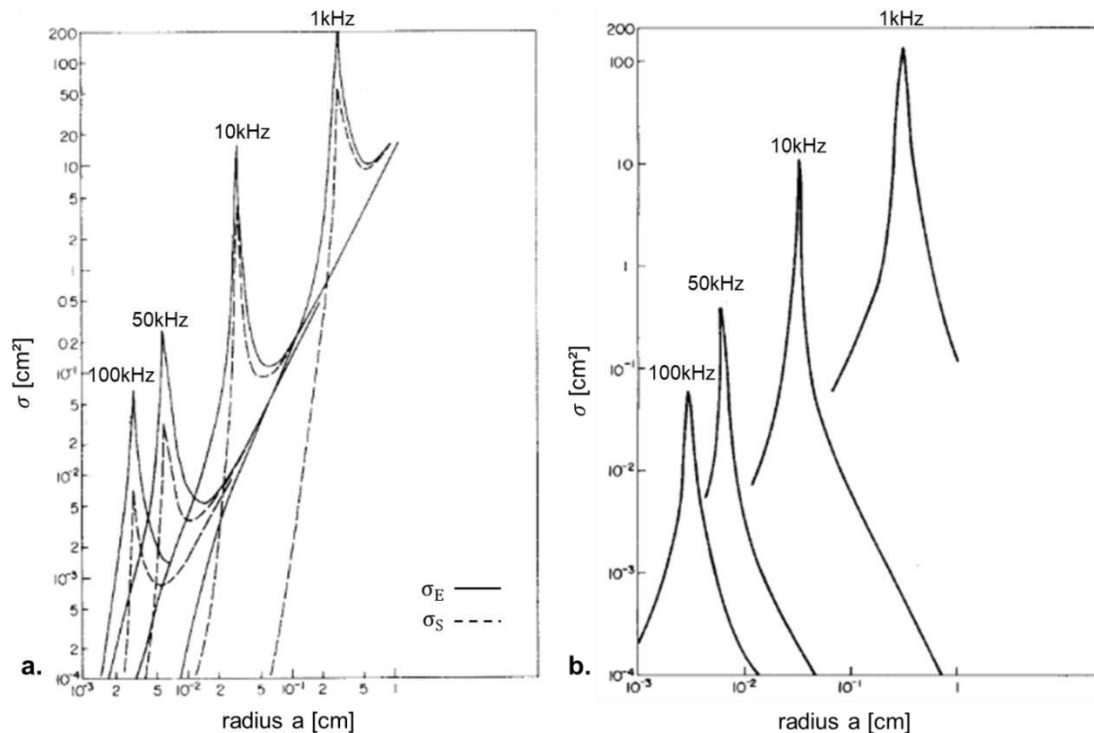
Figure 31: Cross-sectional total scatter σ_S , **extinction** σ_E **and absorption** σ_A for a range of air bubble radii in water at sea level insonified by four frequencies. **a.** Total scattering cross-section σ_S (dashed lines) and extinction cross-section σ_E (solid lines) at four frequencies as a function of bubble radius a. **b.** Absorption cross-section σ_A at four frequencies as a function of bubble radius a. (m.a. [Medwin 1977])

ellipsoidal will have a weaker radiation and a higher fundamental resonance frequency when increasing the aspect ratio [Strasberg 1953]. The resonance frequencies for both oblate and prolate ellipsoidal bubbles was calculated by Weston [Weston 1967] showing that they diverge for aspect ratios greater than 4, while the resonance frequency of the prolate ellipsoid remains slightly higher. **Figure 32** demonstrates the resonance for a prolate ellipsoid at broadside incidence as a function of axial length to cross-sectional diameter. The aspect ratios are the ratio of the major axis to the minor axis. The resonance frequency of a bubble becomes of particular interest when considering harmonic frequencies. Harmonics are integral multiples of the fundamental frequency (first harmonic) and are based on the phenomenon of non-linear sound propagation in tissue or during the insonification of gas bubbles [Schlottmann 2001]. The combination of both the fundamental frequency and its specific harmonics represents a signal´s unique characteristic. While the echoes that compose the fundamental frequency are caused by tissue interfaces and differences in tissue properties, harmonics are produced by the tissue itself [Dutta et al. 2012]. Resonant bubbles emit a significant second-harmonic signal [Miller 1981]. **Figure 33** demonstrates that at second harmonic the graph is strongly peaked at the linear resonance frequency of the bubble. A second but significantly smaller peak can be observed when the bubble is driven at half its linear resonance frequency. Miller found that the second harmonic emissions drop by a factor of 10 with bubble diameters only 1 µm (25 %)

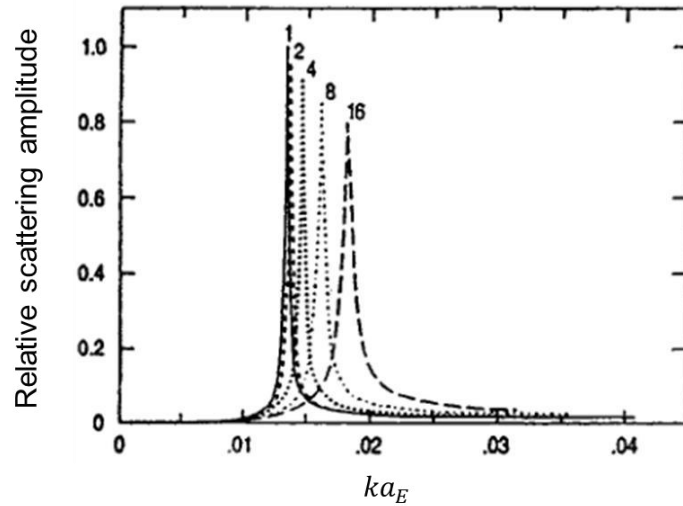larger or smaller than resonance size. Thus, large bubbles are mostly not detectable above background noise.

Figure 32: Change in volume resonance as a function of axial length to cross-sectional diameter for a prolate ellipsoid at broadside incidence at sea level. Aspect ratios 1, 2, 3, 8, and 16 (m.a. [Feuillade & Werby 1994]).
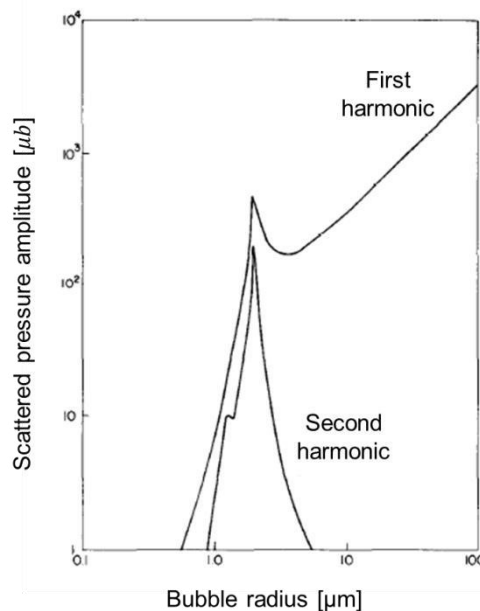

Figure 33: Scattered pressure amplitude versus bubble radius at the first harmonic and second harmonic as calculated from a simplified non-linear theory. Bubbles surrounded by water were exposed to a 1.64 MHz plane wave of 0.2 bar amplitude. The emissions were detected 6 mm away from the bubble (m.a. [Miller 1981]).

3. Conceptual Design

This chapter is intended to develop a conceptual method for the detection of air bubbles in the sound path after data acquisition with the HFUS-assisted intraoral scanning system. In order to determine the needs and conditions for a detection technique, a requirement analysis is carried out that takes relevant characteristics of the gas bubbles in a liquid medium into account. These relate in particular to the position, shape and size of the bubbles to be detected. In addition, acoustic characteristics of gas bubbles within the sound field as described in section **2.5.2** are considered. Afterwards, existing gas bubble detection methods due to ultrasonic data aquisition are summarized. Based on the needs and conditions defined in the requirements analysis as well as the detection methods found in the literature, constructive solutions and concepts are developed and evaluated.

3.1 Preliminary Examinations

Basis of a constructive conception is formed by an appropriate requirement analysis for a detection method of air bubbles. Therefore, a preliminary examination is carried out to investigate characteristics of the coupling space that includes information about a bubble´s and bubble artifact´s shape, size, and location as well as information about other reflection structures in the medium. The characteristics of gas bubbles present in the coupling medium were investigated using three *in vitro* experiments and one *in vivo* patient experiment. Data acquisition and interpretation are described in section **4.1** and **4.2**.

Shape of bubbles in the coupling medium and ultrasonic representation

By visual examination, air bubbles in the coupling medium can be seen in a variety of shapes; some of in a unique form (see **Figure 34**).

Figure 34: Large air inclusions in coupling medium stored in a syringe

However, simplified body shapes can replace a detailed, complicated body. Thus, a spheroidal model is assumed to describe an air bubble in the acoustic field (see section **2.5.1**). In ultrasonic images acquired by the microscanner, however, air bubbles are not displayed as one might aspect. As demonstrated in section **2.3.1**, bubbles cause artifacts that are displayed as slightly curved lines and quasi-circular objects in B-mode and C-mode images, respectively. Their size is strongly dependent on the position of the bubble in the acoustic field. The ultrasound beam from a single, circular focused transducer is characterized by the near field and far field regions with the focal zone located in between. The far field is also known as Fraunhofer zone and demonstrates the diverging beam. If the ultrasonic beam strikes an air bubble´s top boundary, the acoustic energy will be scattered back due to the high impedance mismatch. As the single-element transducer is moved laterally over the image volume, a bubble whose dimensions are smaller than the transducer´s is insonified from various positions. For a bubble positioned in the far field, the bubble is recorded from the diverging beam. If the echo originates from a beam axis other than the main axis it is assumed to be caused by a deeper structure and vice versa. The greater the distance from the focus, the wider the artifact is displayed. In focus, the bubble´s backscatter is displayed as a straight line or a dot only (see **Figure 35**). Thus, a bubble is not shown by its surroundings but their existence is indicated by a characteristic artifact. The center of the line represents the bubble´s scattering area.
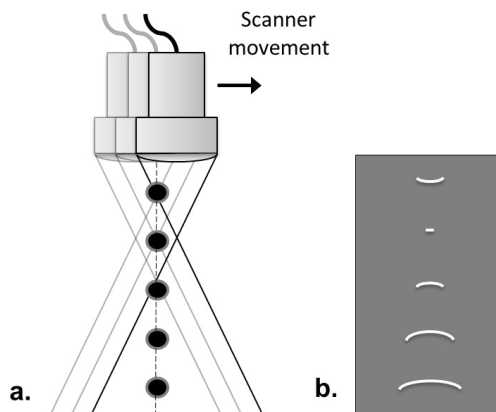

Figure 35: (a.) Air bubbles of the same shape and volume located at various depths in the acoustic field **(b.)** are displayed as slightly curved lines in B-mode images.

In 3D space, the shape of the slightly curved lines may be described as a flat bowl which can also be thought off being a portion of an ellipsoid of revolution with $a = b$. Considering the C-slices as intersecting planes through the bowl at 90°, the following conclusion can be drawn: the plane cross-section is displayed as a circle with radius a. This assumption is wrong, when

changing the angle of intersection through the ellipsoidal part. As the B-mode slices are not equidistal due to the scanner´s trajectory, distortion of the circles occurs. Thus, they can be described as being of an elliptic shape. In a two-dimensional Cartesian coordinate system, an arbitrary ellipse is defined by five parameters: (x_0, y_0) for the center, θ for the orientation, (a, b) for the semi-major axis and semi-minor axis, respectively [Xie & Ji 2002]. The orientation describes the main axis rotation by θ with respect to the x-axis. The formula is given by

3.1

$$\frac{\left((x - x_0)\cos(\theta) + (y - y_0)\sin(\theta)\right)^2}{a^2} + \frac{\left((x - x_0)\sin(\theta) - (y - y_0)\cos(\theta)\right)^2}{b^2} = 1$$

Figure 36 illustrates an ellipse in a two-dimensional Cartesian system. Calculation of the area of an ellipse is given by eq. **3.2**.

$$A_E = \pi ab \qquad\qquad 3.2$$

A circle represents a particular case of an ellipse for $a = b$. Thus, it´s area is determined by

$$A_C = \pi a^2 \qquad\qquad 3.3$$

The aspect ratio of a geometric shape indicates the ratio of its sizes in different dimensions. For an ellipse, this describes the ratio from the major axis a to the minor axis b. Thus, a circle has an aspect ratio of 1:1. Due to the relationship of ellipse and circle, only properties of the ellipse are discussed hereinafter.
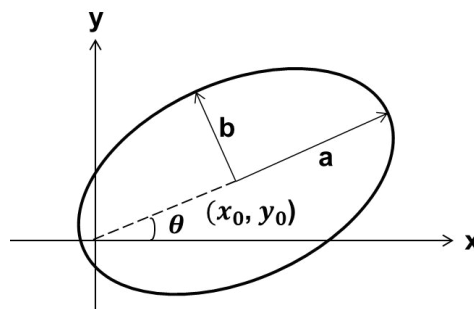

Figure 36: An arbitrary ellipse is defined by five parameters: (x_0, y_0) for the center, angle θ for the orientation, (a, b) for the semi-major axis and semi-minor axis, respectively.

Size of air bubbles and bubble artifacts

Air bubbles of macroscopic size can be observed in the coupling medium. Due to the high incident frequency used by the transducer (approx. 50 MHz), bubbles of macroscopic size satisfy the formula $ka \gg 1$. Thus, only geometrical scattering of bubbles is expected when recording acoustic data with the microscanner. However, the bowl-like artifact caused by an air bubble in the acoustic field does not allow for direct determination of the bubble size. It can be assumed that bubbles of variously sized scattering surfaces located at the same depth in the acoustic field will cause lines of different width. For determining the size of a bubble, a depth-dependent calibration curve considering a spherical bubble of various volumes may be used. However, generation of an appropriate calibration curve is a cumbersome process. Nevertheless, the size of the artifactual bowl can be measured in sonographic recordings. Therefore, C-mode images where generated and the strong outlines of the bubble´s artifacts were measured. For three *in vitro* experiments, the combined mean semi-major axis length per sample was plotted to visualize the variations of the ellipse´s size versus depth in the acoustic field (see **Figure 37**). Due to the theory the artifacts are shown as small lines or dots in focus, the approximate position of the focus is demonstrated by the red line. The outcome of this experiment supports the hypothesis that the size of the acoustic artifact is dependent on the bubble´s depth in the acoustic field. The collected data do not allow any conclusions about the bubble size. These were therefore not included in the calculations.
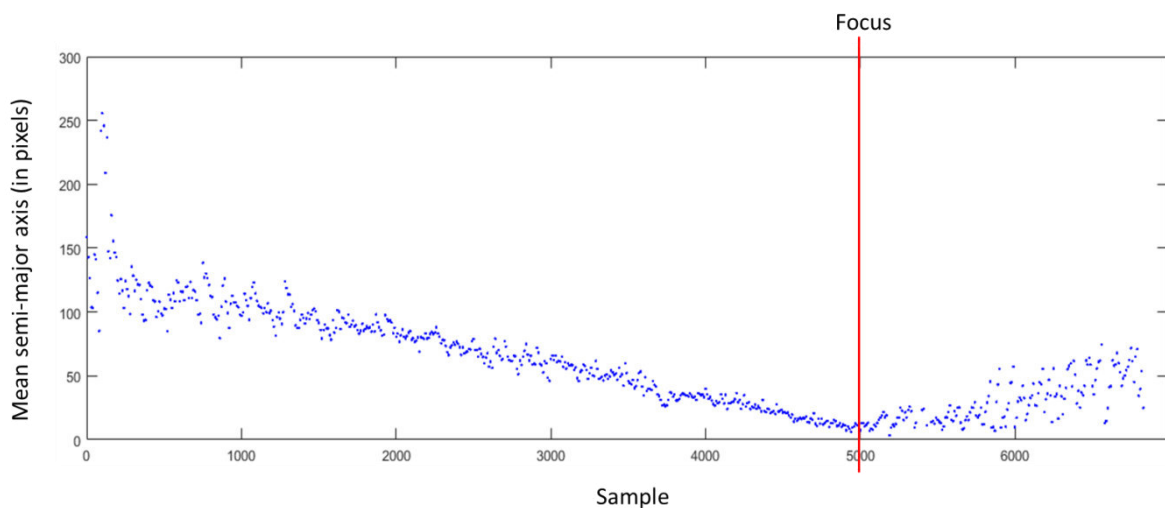

Figure 37: Combined mean length of semi-major axis a (in units of pixels) for three *in-vitro* experiments versus sample depth. The red line indicates the expected location of the focus in the acoustic field. Strong deviations in the samples are thought to be caused by a low amount of data available.

Location and occurence of gas bubbles in the coupling medium

In routine recordings, gas bubbles can be observed throughout the entire coupling space. As part of his master´s thesis at the present HFUS-assisted scanning system, Gladbach [Gladbach 2018] investigated the formation of bubbles due to potential interactions between the coupling medium and contacting intraoral materials such as gingiva or tooth as well as the intraoral coupling element. He performed several *in vitro* as well as *in vivo* (anterior tooth, tooth 11) experiments. Therefore, his findings regarding the position and behavior of bubbles are briefly summarized. By placing the scanner head on the intraoral interface element, air may be locked underneath the acoustic window. The amount of ultrasound gel used and the shape of the gel front are crucial for trapping the air. Size and thus volume of the air inclusions are variable. In addition, when the coupling medium is applied by means of a syringe and applicator needle, the bubbles already present in the gel are injected. Thus, single air bubbles and bubble curtains occur in the entire gel area without contact to other materials. Gladbach further observed that air bubbles in the coupling space occur especially on rough or textured surfaces and attributed this to including gas residues that serve as bubble nuclei. An increased bubble formation was seen at the edges and surface of the element for intraoral coupling. Furthermore, Gladbach was able to identify critical sites in the anterior tooth region due to *in vivo* examinations, mentioning in particular the tooth surface, sulcus and incisal edge as well as the areas tooth-gingiva-tooth (gap), sulcus-gingiva and tooth-tooth contact (see **Figure 38**). This confirms the observations made by Riedel who also found air bubbles on the occlusal surface of molars [Riedel 2016]. The presence of bubbles in the sulcus area can also be promoted by saliva foam, which already has a high proportion of air bubbles that keep remained after gel application. An interaction between blood and gel is also seen to form bubbles. Detachment or rising of the bubbles could not be observed. Also, Gladbach describes the growth of bubbles in the relevant time period for coupling of 15 minutes. After a bubble nucleus is in a stable state, it strives to reach an equilibrium level. The bubble grows until the pressure difference Δp becomes zero or the concentration of the two phases is balanced. Due to bubble growth adjacent bubbles close together or a reduction in favor of another bubble occurs. Growth was detected in air bubbles located in the above mentioned critical zones as well as in injected bubbles. Somme bubbles grow to macroscopic size. Again, detachment or rising of the gas bubbles could not be observed. The exact size and number of bubbles occurring was not further determined by Gladbach.
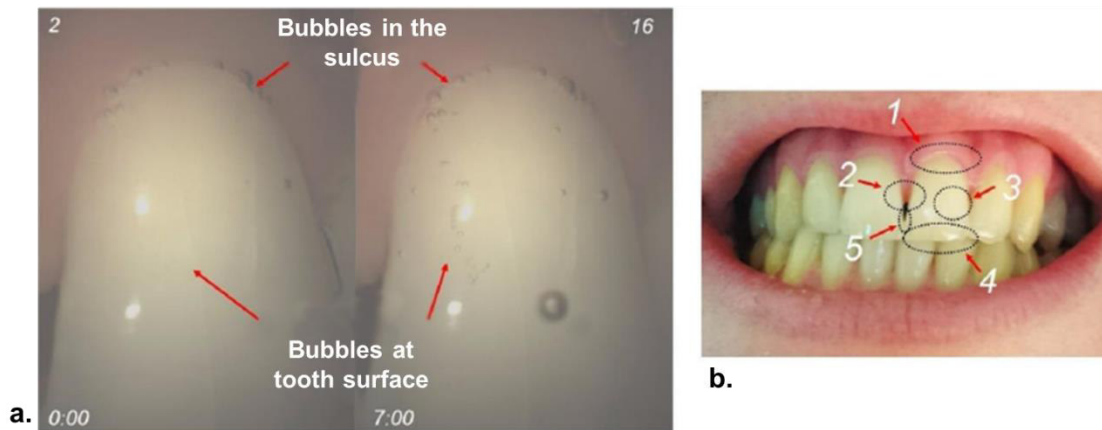
Figure 38: Critical sites observed in *in-vivo* experiments. **a.** At application and seven minutes after application of the coupling medium. **b.** 1: sulcus-gingiva; 2: tooth/gingiva/tooth (gap); 3: tooth surface; 4: incisal edge; 5: tooth-tooth contact (gap) (m.a. [Gladbach 2018])

Other reflecting structures in the coupling space

In a clinical procedure, the intraoral situation may differ from an idealized model. **Figure 39** illustrates a simplified intraoral interface with potential sources of error. Those structures are especially meant to be strong reflectors in the ultrasonic field. Thus, they may falsely be interpreted as originating from the tooth surface, particularly when located close to it, or may cause image artifacts. Here, the term foreign bodies includes all substances that are induced into the intraoral interface either by application of the ultrasound gel (e.g., dust, metal by applicator needle) or that may have already been in the intraoral space (e.g., food particles, remaining dental hard tissues after preparation) as well as other substances not further defined. Air bubbles are excluded from this definition and are shown separately. Foreign bodies may have a variety of appearances at tooth sonography.
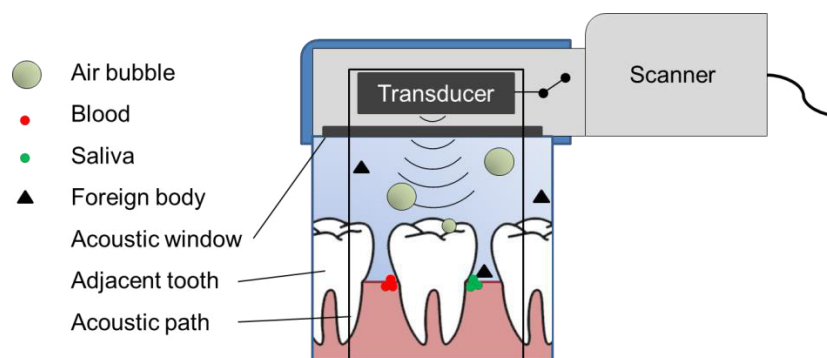

Figure 39: Intraoral interface with potential sources of error that may cause artifacts and/or inaccuracies in the digital impression outcome

Another highly potential reflector is given by the acoustic window that causes reverberation artifacts in B-mode images (see chapter **2.3.2**). At last, a closely spaced adjacent tooth may be detected by a side lobe. How far these structures reflect and disturb the tooth detection or how they are characterized in the ultrasound field was not further analyzed.

3.2 Requirement analysis

The production of high-quality dental restorations requires an accurate reproduction of the intraoral situation. By ultrasound, the surface of a prepared tooth in the micrometer range can be detected and converted into a digital model. The coupling of the acoustic waves is done by means of a water-based ultrasonic gel. Due to the strong impedance difference, maximum reflection at the tooth surface can be achieved. However, like other (non-invasive) medical imaging modalities, sonography is prone to image artifacts (e.g. reverberation artifact, shadowing, or echo displacement) resulting in strong image degradations. Artifacts may cause reduction of the accuracy of the digital impression. Air bubbles within the coupling space represent a major disruptive factor. The findings obtained by the analysis of the bubble position, size, and shape as well as the phenomenon of the bubble artifacts allows for first requirements settings for the implementation of a (software-based) bubble detector. Air bubbles can be described as ellipsoid-shaped air pockets whose volume can be determined by equation **2.7**. Air bubbles present are observed to be in the macrometer range. Nevertheless, bubble formation may cause bubbles with a radius of a few micrometer. Due to the scanner movement bubbles cause artifacts in the shape of a bowl. Those artifacts are therefore an indication for the presence of an air bubble in the acoustic scanning region. In C-mode images, air bubbles stand out from their environment as ellipses whose area can be calculated by equation **3.1**. In the Cartesian coordinate system, an arbitrary ellipse can be determined by five parameters: (x_0, y_0) for the center, θ for the orientation, (a, b) for the major and minor axis, respectively. The equation is summarized in **3.3**. In recordings used for this work, artifactual bowls with a minimal and maximal major axis length of 1.15 and 511.53 (in units of pixels) were found, respectively. An averaged value for the mean major axis and mean minor axis was calculated to be 146.8 ($\pm$ 62.1) and 107.55 ($\pm$ 50.72), respectively (in units of pixels). The length of major and minor axes is especially dependent on the position of a bubble in relation to the focus. Their mean aspect ratio was found to be 1.48. The detected algorithm should therefore be able to detect bowl artifacts in this size range. Gladbach observed the growth of air bubbles during his investigations on the appearance of air bubbles in the coupling space. The observation was evaluated over a time interval of 15 minutes and 30 minutes relevant for

the coupling procedure. Bubble growth is usually a slow process. Due to the fast recording time of the microscanner, which takes about two minutes, it is assumed that there is no further significant growth. Thus, bubble growth is not a factor during detection. Furthermore, it is assumed that the bubbles do not rise during the recording procedure and, thus, are stationary air bubbles. Accordingly, continuous monitoring of the coupling space is not required. When the ultrasound gel is applied, gas bubbles present in the gel are induced into the intraoral interface, but it also favors the inclusion of gas residues on rough surface structures such as the interface element and the tooth hard material by small irregularities. Bubbles that attach to the sidewalls of the interface element are outside the measuring field of the microscanner and can therefore be ignored. In particular, however, the air bubbles occur at critical sites such as sulcus-gingiva, tooth/gingiva/tooth (gap), tooth surface, incisal edge, and tooth-tooth contact (gap) as described in section **3.1**. Depending on their size and the initial ultrasonic frequency, the air bubbles represent a geometric reflector or they oscillate at a specific frequency. Because of the large impedance differences between the ultrasound gel and air, large bubbles located above the tooth surface may reflect or absorb a large portion of the acoustic energy. As a result, less energy will be transmitted to the tooth surface where a relatively weakened echo may occur. However, a more critical factor is presented by bubbles close to the tooth surface and at a depth other than the focus. As they cause the characteristic artifact, they can erroneously be interpreted as being part of the tooth´s hard tissue and thus be included in the calculations during data processing. They also may cause other artifacts, such as shadowing or multipath artifacts, so that data gaps or a displacement of the tooth´s structure occurs, respectively. A detailed analysis on the distances of air bubbles to the tooth surface with regard to the effect on individual processing steps has not been carried out and is beyond the scope of this work. However, it can be assumed that especially sample depths outside of the focus are affected by the poorer lateral resolution. In addition to the bubbles, other (strong) reflectors of acoustic waves are present in the coupling space. These include the tooth and the debris described in section **3.1.** The bubble detector should therefore be able to distinguish between echoes due to bubbles or other scatterer. Visualization of the coupling zone throughout the treatment is not given and manual identification is a cumbersome and time-consuming task. Therefore, an automated or semi-automated detection system using acoustic recordings is to be carried out.

3.3 Bubble detector systems

A literature research on existing methods for gas bubble detection using ultrasonic techniques was performed. Ultrasonics provides a non-contact probing method for versatile applications. Numerous studies have been carried out in the field of bubble perception, detection, and bubble characteristic measurements making use of non-invasive acoutic methods. In medical engineering, bubble detection is critical for several reasons: to maintain a steady-flowing circuit and to prevent complications caused by air embolism entering the cardio-vascular system [Davey & Stather-Dunn 2005]. The detection of bubbles is thus generally applied to extracorporal tubes such as for dialysis or medical drug delivery systems. Intravascular microbubbles due to decompression sickness in divers are detected by means of Doppler ultrasonic monitoring for diagnosis [Beck et al. 1978; Walker 1996]. A technique making use of bubbles is given by the detection of microbubbles as echocontrast agents in medical investigations such as tumour diagnosis and treatment [Calliada et al. 1998; Ignee et al. 2016]. In oceonagraphy, ultrasonic approaches are used for the research of gassy sediment such as coastal gas bubble formation in organic-rich sediment, the role of gas bubbles for sediment geotechnical properties, biogeochemical processes etc. [Wildman & Huettel 2012]. Thus, acoustic gas bubble detection is not limited to medical approaches.

The acoustic properties of gas bubbles were described in section **2.5.2**. Determinitions of the existence of air bubbles have been based on geometrical and resonance acoustic backscatter, excess attenuation, and differential sound speed as well as on their non-linear behavior and acoustic Doppler shift. Further segmentation procedures in sonography are given by image-based methods. Image-based detection methods related to the presence of individual air bubbles could not be identified but present a strong technique in routine medical diagnostics. Automated and semi-automated methods were found. Systems relevant to this work are summarized in the following. Due to the requirement of bubble motion, the Doppler approaches are excluded.

Geometrical approaches based on transmissive ultrasound

The simplest method for detecting gas bubbles in an acoustic field is implemented by the use of two ultrasonic transducers, a transmitting and a receiving one. Both transducers are placed in such a way that they face each other with the medium to be examined located in between. This principle is commonly applied if bubble detection in a medium flowting through a tube is necessary as it may be the case in filling pipelines [Wen et al. 2014] and medical drug delivery systems [Ozeri et al. 2006] (see **Figure 40**). Emitted longitudinal acoustic waves propagate

through the tube perpendicularly to the fluid´s flow and are detected by the receiver on the opposing side of the tube. In such approaches, the passage of sound through a medium is evaluated. Acoustic attenuation is typically determined that varies with different media properties. In theory, an incident sound wave reflects strongly off of a gas-liquid boundary due to a rapid change in acoustic impedance. The combination of scattering and absorption by bubbles causes a sound wave to attenuate. It is therefore assumed that the attenuation of acoustic energy is much higher in air bubbles than in the fluid passing by. Thus, the wave´s magnitude detected by the receiver after encountering an air bubble will be lower than a wave´s magnitude after propagating through the fluid only. In addition, several studies observed an interrelation between voltage attenuation and bubble radius [Ozeri et al. 2006; Wen et al. 2014]. Hence, acoustic attenuation is generally enhanced with increasing bubble size providing the possibility to estimate a bubble´s volume or size by means of digital signal processing algorithms. The numerical relationship is usually acquired by experiment. It should be noted that the same attenuation for a particular bubble size is only given, if the bubble passes through the acoutic field at the same position [Wen et al. 2014]. The use of two transducers allows for continuous ultrasonic examination and thus allows for continuous bubble detection. Another method is based on the theory that the air bubbles have a much lower speed of sound than their surrounding medium. Those sensors measure the transit-time of a sound pulse. Change in speed of sound due to sound bubbles results in a temporal shift in the detection of a transmitted pulse in comparison to the perception of a pulse that has only penetrated the homogeneous medium [Benech & Novakov 1999]. The change of both amplitude attenuation and speed of sound is also given by material-bound acoustical properties such as those of the tube boundaries, while the sound waves propagate through different portions of the air bubble sensor. In such approaches, the tubes inner diameter is comparable to the gas bubbles diameter that have to be detected are usually in the range of a few millimeters and the tubes the medium is flowting through are of a comparable inner diameter.
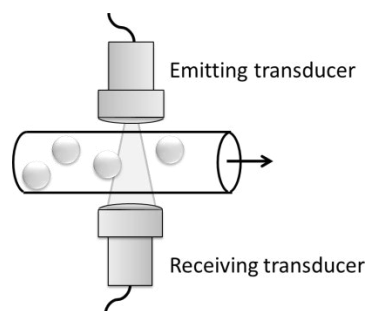

Figure 40: A transmitting and a receiving transducer are placed on opposing sides of a tube in which a liquid medium containing air bubbles is flowting through.

Geometrical approach based on reflected ultrasound

Gas bubbles are a highly efficient scatterer. Hence, a bubble produces an increased signal output of the transducer that can be distinguished from the background signal. Other than in a transmissive acoustic approach, the detection of backscattered echoes requires one transducer only that functions as both an emitter and receiver of acoustic waves. Bubbles are then determined due to impedance changes they cause in a medium [Wildman & Huettel 2012]. To produce an optimal geometric scattering cross-section these bubbles are often relatively large and meet the requirement $ka \gg 1$ (see section **2.5.2**). It then can be differentiated between acoustic signals generated by embedded backscattering objects (e.g., bubbles) and background signal representing homogeneous media (e.g., water or sand). This approach may also be applied to tubes of medical infusion pumps. A linearity between the sensor´s response and bubble can be observed [Benech & Novakov 1999]. Envelope backscatter data typically show a clear maximum when a bubble is penetrated by an acoustic wave. Large amplitude output may not be true if bubbles are near the resonant size.

Resonance frequency-based and second harmonic detection

As described in **3.1.1**, the largest detectable effects occur if a structure is capable of resonating in an acoustic field. Thus, insonification of gas bubbles with a frequency that corresponds to a bubble´s resonance frequency presents a feasible technique to detect bubbles of a specific radius. In medical approaches, this pricinciple is commonly used in ultrasound contrast imaging techniques where free gas bubbles or encapsulated gas bubbles serve as US contrast agents [Dutta et al. 2012]. This allows more detailed perfusion imaging of the cardiovascular system, tumors, and other anatomic structures. The microbubbles are typically gas filled spheres in the range of a few microns and their resonance frequency matches the 1-15 MHz range of clinical US. At resonance frequency of the bubble, scattering and absorption are at a maximum [Nishi 1972]. Using the resonant behavior of gas bubbles in a liquid becomes of particular interest when considering harmonic properties of acoustic waves. For the detection of resonant bubbles, registration of second-harmonics is suitable. Stable bubbles pulsate non-linearly in an acoustic field with amplitude that depends strongly on their size. Resonant bubbles emit a significant second-harmonic signal. Larger bubbles and other structures which do not convert a significant part of the incident wave to non-linearly scattered ultrasound at the second-harmonic are ignored, provided that the second-harmonic background noise in the detector is low. Thus, only resonant bubbles are detected by a device that is based on this method. Resonant approaches typically estimate the bubble size

according to the frequency reflected by the air bubble and, thus, provides a more accurate bubble size estimate than the other methods described above [Medwin 1977].

Image-based segmentation

Segmentation of medical image data is a common method in order to support diagnosis in several medical disciplines. However, US images are difficult to segment due to the relatively low quality in the presence of noise. In medical sonography, image-based segmentation is often done manually or requires manual user interaction. In clinical applications, this method is cumbersome, time consuming and decreases reproducibility. Thus, automatic or semi-automatic applications have been developed. However, fully automatic approaches bear the risk of not being robust. Depending on the level of feature extraction, it can be differentiated between pixel-, edge-, and texture- or region-oriented approaches [Deserno 2011]. In the medical application domain, recent developments incorporate a priori knowledge, e.g. such as anatomical models. State of the art methods for model- or knowledge-based segmentation are given by *Active Contour Models* [Chen et al. 2003; Liu et al. 2010], *Active Shape Models* [van Ginneken et al. 2002; Kropatsch et al. 2007] and *Active Appearance Models* [Cootes et al. 2001]. However, these approaches are difficult to implement, may require an interactively set starting point for segmentation or make use of registrations of training sets of labeld examples [Deserno 2011]. In general image processing, the *Hough Transform* (HT) is commonly used for detecting objects having a simple mathematical description with a small number of determinable parameters such as lines or curves. More complicated geometric figures are also possible to detect, but require more computational time and data memory. The method was patented in 1962 by Paul Hough in "*Method and Means for Recognizing Complex Patterns*" [Hough 1960]. HT refers to a data-based feature extraction joining the information of all pixel [Deserno 2011]. Traditionally, it represents a shape recognition approach of patterns in a binary image that applies edge-based segmentation and region-based aspects. For each point in the image that lies on an edge, all possible parameters of the shape to be detected are transferred into a parameter space (also called Hough space). Each point in the Hough space thus corresponds to a geometric object in the image space. Those parameters may be the slope of a straight line or the radius of a circle. The parameter space then is evaluated by obtaining local maxima which represent the figure of interest. In literature, various methods are found describing the detection of lines, circles and ellipses via Hough [Duda & Hart 1972; Ballard 1987; Bennett et al. 1999; Xie & Ji 2002].

3.4 Basic Concept Development

Based on existing detection methods (see section **3.3**) and the requirement analysis (see section **3.2**), four basic concepts are developed. These are briefly explained in the following. At the end of the chapter an evaluation of the feasibility of these concepts is given.

3.4.1 Concepts

The following statements can be made for all concepts. The data processing was described in **2.2.3**. After storing the digitized RF data, they are transformed into two-dimensional raw data. Using the VSAFT algorithm, the lateral resolution can be increased in depth. A subsequent threshold-based maxima detection per A-line to distinguish between gingiva and tooth surface provides the basis for a 3D tooth model. Due to a small amount of sidewall echoes, information has to be interpolated by means or the TPS-RPM approach. Finally, a 3D reconstruction of the overall tooth surface is possible. The VSAFT algorithm was identified as a critical process step in which the existence of air bubbles and their corresponding bowl-like artifact may have a negative impact on further calculations. It therefore is useful to detect present air bubbles in critical areas before performing the VSAFT approach. Thus, information concerning the position of the bubble is of particular interest. In order to prevent the loss of significant medical data, outcome of the detection method should be given as a matrix or structure that can be passed on to the VSAFT approach for calculation. Thereby, the given input is not changed but rather additional information is provided. Furthermore, in theoretical considerations it is to be assumed that the recorded medium does not perform any movement other than potential vibrations caused by the acoustic field during the acquisition process. In the following, four basic concepts are presented for the detection of air bubbles in the acoustic field.

1. **Concept: Transmission Method**

The intraoral interface element is extended by two transducers, each located on the opposing side wall of the long axis (see **Figure 41**). The transducers are capable to move along the side walls simultaneously to scan the whole volume. The measurement takes place before or after data acquisition by the intraoral microscanner is done. Thus, falsification of the measurements due to additional acoustic rays is prevented. The presence of air bubbles located above and beside the tooth surface is detected by measuring the attenuation. By means of a suitable calibration curve, an estimate of the volume of air inclusion in the specific depth can be made.
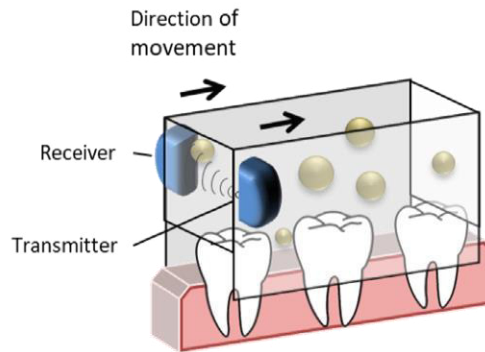
Figure 41: Transmissive approach detecting the presence of bubbles in the acoustic field due to the attenuation they cause. Both the transmitting and receiving transducer are moved simultaneously along the side wall of the intraoral interface element.

2. Concept: Backscattered Signal Detection

Pulse-echo data are acquired with the intraoral microscanner at a frequency valid for patient examination. The assumption is made that due to the impedance mismatch at acoustic interfaces, backscattering objects produce sets of amplitude peaks in the record, and areas of minimal signal imply a homogenous acoustic medium. As described in section **2.5.2**, air bubbles present a strong scatterer of acoustic energy. Due to the scanner movement they cause a bowl-like artifact that is displayed as lines of high echogenicity in B-mode images. An algorithm may be implemented that extracts local maxima of the amplitude above a defined threshold per A-line signal for feature extraction. A peak-clustering method is applied to find boundaries of a bubble´s artifact.

3. Concept: Second-Harmonic at Resonance Frequency

Due to the large scattering cross-section of a gas bubble at resonance and the relationship between resonance frequency and bubble radius, a variable-frequency backscatter method presents a feasible technique for detecting bubbles of various radii. Additional transducers of various frequencies are applied in the scanner head. They are placed side by side so that the backscattered signal is measured. The scan area is captured several times before or after the data acquisition of the microscanner so that they do not hinder an accurate measurement of the scanner. Each record is done using a different sound frequency that matches the natural resonance frequency of the bubbles in the radius range to be detected. By means of the position data acquired by the sensor and an appropriate registration algorithm, the data are summarized. Due to the non-linear behavior of the gas bubbles, the harmonic frequencies are considered.

As described in section **3.1**, the contours of the air bubble´s characteristic artifact can be seen in C-mode images. Simplified, the structure can be described as ellipses. Therefore, C-mode images are first generated for each sample depth. By means of the Hough Transformation, elliptical structures in images are then detected. Parameters of the ellipse such as the center, major and minor axis, and orientation are determined. In a further step, found ellipses are clustered to form an ellipsoid in the 3D volume.

3.4.2 Concept evaluation

Four concepts were described, based on attenuation, geometrical and resonance-based backscattering data, as well as image-data. Their feasibility is evaluated briefly.

Concept one is based on the measurement of the acoustic attenuation in a transmissive ultrasonic approach. This requires the development of a new cost-intensive scanning system that scans the volume along the sidewalls of the interoral coupling element stepwise. Due to the limited space in the oral cavity, implementation will be difficult and may cause additional discomfort for the patient. Measurements of the bubble sensor and microscanner cannot be done simultaneously to prevent interference of the acoustic rays. Therefore, not only an additional procedure step is necessary, it also prolonges the treatment time massively. By measuring the attenuation, the presence of gas bubbles can be confirmed, and a suitable calibration curve can be used to estimate the volume of air in the respective sound field. A statement about the attenuation can only be made if the bubble of the same volume crosses the acoustic field at the same point. Assuming two bubbles of equal volume and shape at different positions in the acoustic field, the bubble located closer to the receiving transducer will cause a bigger attenuation due to a higher blockage of acoustic energy (see **Figure 42**) [Wen et al. 2014]. The development of a calibration curve is very complicated and requires a prolonged investigation. However, this measurement technique offers no possibility to determine the number and exact position of the air inclusions. It should also be noted that the tooth itself represents a strong reflector in the acoustic field. Thus, a complete extinction of the acoustic energy behind this structure can be expected. Accordingly, no conclusions can be drawn about air bubbles that are located anterior or posterior to a tooth. In summary, this concept is rejected.
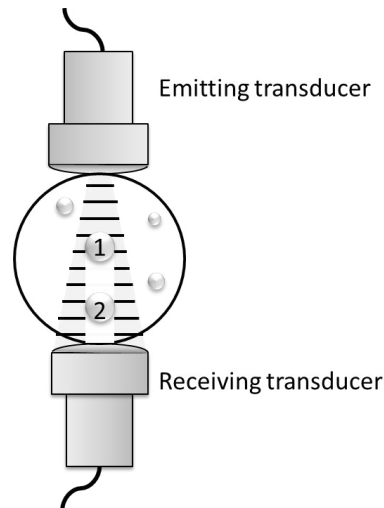
Figure 42: Attenuation behind two bubbles (1 and 2) of the same volume and shape located at different positions in the acoustic field. Bubble 2 blocks more acoustic energy and, thus, causes a bigger attenuation.

Another technique that requires a change of hardware is provided by concept three that is based on the resonance frequency of a bubble. Resonant scattering is only given for bubbles that meet the requirement $ka \ll 1$. Due to the large radius of the bubbles present in the acoustic field, ultrasonic radiation in the kHz and low MHz range is required. Additional transducers are necessary, which in turn lead to additional measurements. Therefore, the same disadvantages can be mentioned in this regard: further costs, and prolonged scanning time. Nevertheless, considering the non-linear behavior of a bubble at second harmonics, only resonant bubbles will lead to significant signal amplitudes that can be distinguished from the background and other linear structures. To some extend, water and blood present a non-linear medium which acquires a second-harmonic component if hit by an acoustic wave. This may falsely be interpreted as a bubble by the detector. However, due to the drawbacks mentioned this concept is rejected as well.

As concept one and three present direct bubble detection approaches, bubbles in the coupling space of the moving microscanner are also indicated by a characteristic artifact reffered to as bowl-like artifact. Thus, another possibility is provided by the implementation of an indirect detection algorithm. One technique is based on the geometrical scattering of gas bubbles in an acoustic field given by concept two that detects a bubble´s artifact according to their strong backscatter amplitude they cause in the receiver. Thus, the analysis and feature extraction of high amplitudes per signal presents a feasible detection technique. **Figure 43** demonstrates an A-line signal (marked in red in the B-mode image) after envelope detection and strong noise reduction below a defined threshold. The signal graph is tilted so that it matches the bowl-lines

in B-mode. Nevertheless, other strong reflectors and noise are present in the acoustic field. As the tooth is expected to be a highly efficient scatterer, it will cause high amplitudes as well and may therefore be confused as resulting from a bubble. Also, it may be possible that the echoes caused by another strong scatterer present overlap a bubble´s echo. Still, this concept may be a first detection method and is therefore pursued in the following.
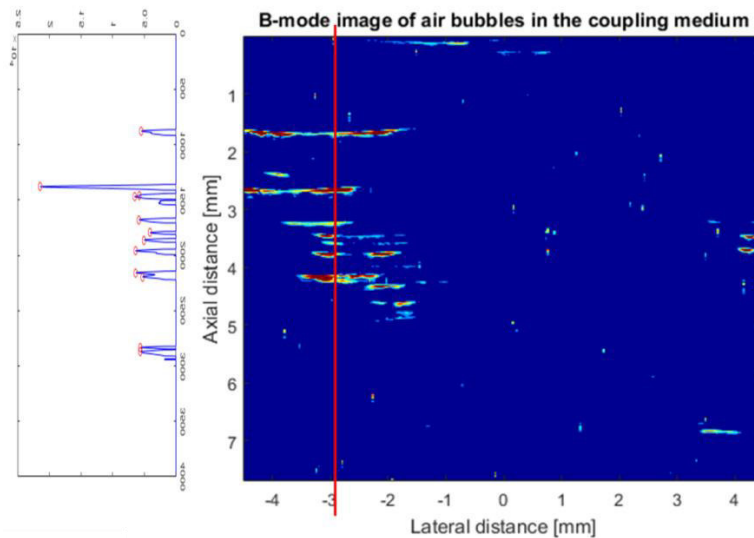

Figure 43: Artifacts caused by bubbles are diplayed as quasi-linear lines in a B-mode image. The red line presents the position of the A-signal shown in the graph on the left-hand side. Peaks in the A-line present the strong backscatter amplitude of the bubble´s artifact.

Concept four requires the generation of C-mode images which is a time-consuming process. The simplest way of obtaining them is given by the acquisition of a 3D data volume and output of images from an angle perpendicular to B-mode. However, the creation of a 3D data volume requires a great RAM. Also, each B-mode slice needs to be pre-processed by means of band-pass filtering and envelope detection before a C-mode image can be extracted from the volume. However, a *Hough Transformation* (HT) is a technique typically used to find simple structures in images such as lines or circles. Five parameters are needed to fully define an ellipse. Therefore, a generalized HT typically requires a five dimensional parameter space that is a memory and time-consuming process. In literature, however, a fast and efficient ellipse detection system is found using a one-dimensional accumulator array to accumulate the length information of an ellipse´s minor axis [Xie & Ji 2002]. HT therefore presents a powerful technique and, thus, concept four will be pursued as well.

4. Methods

Three laboratory *in vitro* experiments and one *in vivo* experiment were conducted to determine the feasability and limits of the ultrasonic detection of small bubbles in the intraoral interface of the HFUS-assisted microscanner.

4.1 Data Acquisition

Data acquisition *(in vitro)*

Three *in vitro* experiments were performed that are hereinafter referred to as *A+, B-* and *B+*. The experimental setup was composed of a coupling medium filled test chamber, the ultrasound-based dental scanner with an integrated single-element transducer (39.8 MHz, 45% bandwidth, $f_\#$ = 6 mm) (S.CAI System, whitesonic GmbH, Aachen, Germany) as described in [Vollborn 2017], a fixation clip, and a holder. For *B-* and *B+*, an additional calibration body was used to function as a rigid scatterer. It was positioned in such a way that the center of the body was aligned with the center of the chamber ground. Chamber and calibration body are shown in **Figure 44**. *A+* accordingly denotes the experimental procedure without test body making use of a test chamber of the same dimensions.
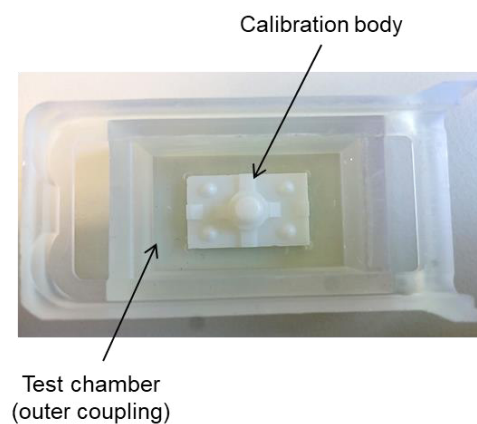

Figure 44: Test chamber and calibration body used for the B+ and B- acoustic readings.

The couple medium (Sterile Aquasonic® 100 Ultrasound Transmission Gel, Parker Laboratories, Inc., Fairfield, USA) was injected using a medical syringe of 10 mL volume (Injekt® 10 mL, Luer Solo, B. Braun Melsungen AG, Melsungen, Germany) and a metal application needle. The samples differ as follows:

- *A+*: injection of couple medium without particular avoidance of air inclusions

- *B-*: particular interest in avoiding the injection of bubbles; removal of tall bubbles using the syringe and application needle
- *B+*: after data acquisition of sample B-, air was manually injected into the test chamber with a syringe to form air inclusions in the ultrasound gel
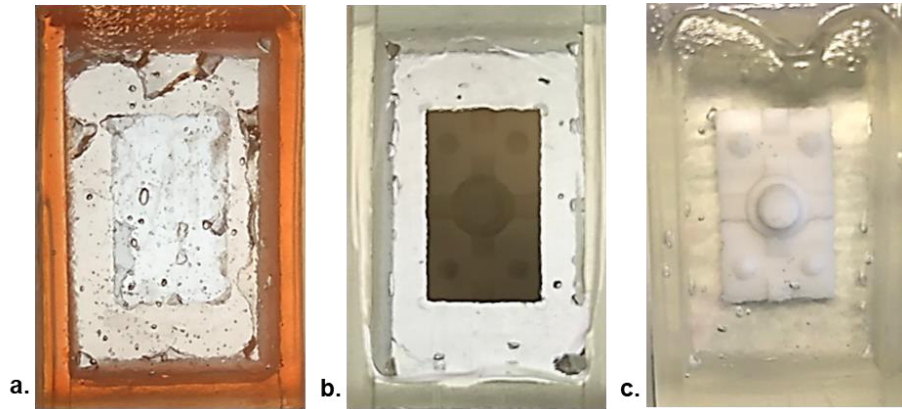

Figure 45*: In vitro* test chambers filled with coupling medium for **a.** A+, **b.** B-, and **c.** B+.

Bubbles were observed by visual inspection in the overall test chamber directly after injection (see **Figure 45**). Gas in the bubbles is assumed to be air. Temperature of the coupling medium was measured using a standard digital thermometer prior to coupling and were 21.9 °C for sample A+, and 18.6 °C for sample B- and B+. The temperature-dependent speed of sound c (in m/s) in the ultrasonic transmission medium was approximated by formula **4.1** which was determined during measurements of the gel.

$$c \cong -0.0545T^2 + 4.4989T + 1485.7$$

4.1

where T denotes the temperature in °C. In order to prevent large air inclusions close to the acoustic window, the test chamber was filled up beyond its edges. Excessive coupling medium was removed using a scraper so that a smooth surface was obtained. The scanner head then was placed on the test chamber and fixed with a clip. In order to avoid motion to cause movement artifacts, the experimental setup was placed on a holder. **Figure 46** shows the setup. Due to the intraoral interface element the sample was positioned such that the beam axis aligned with respect to the sample´s surface normal. Acoustic readings where collected with a step width of $\Delta x = \Delta y = 15\ \mu m$. Afterwards, the analog data were digitized with an ADC (370 MS/s, 16 bit) and stored on a computer. Resulting A-line data were transferred into MATLAB raw data slices and provided for further processing.
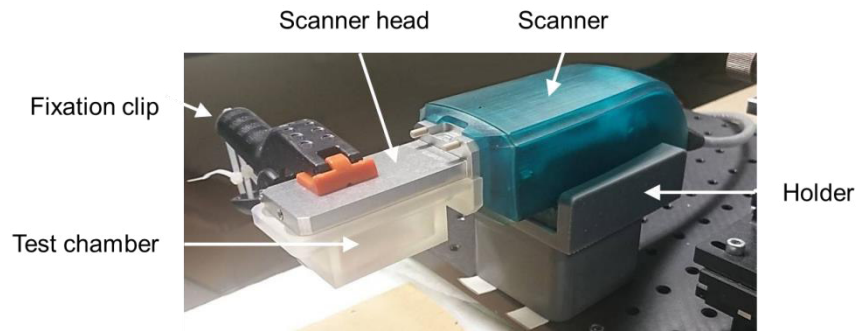
Figure 46: Setup of the *in vitro* experiments *A*+, *B*-, and *B*+

Data acquisition *(in vivo)*

One *in vivo* experiment, carried out under routine practical conditions, was provided for this thesis. The proband was placed on a dental chair in a lying position. The ultrasonic coupling medium (Sterile Aquasonic® 100 Ultrasound Transmission Gel, Parker Laboratories, Inc., Fairfield, USA) was heated to body temperature (approx. 36 °C). The intraoral interface element was placed in the anterior teeth region parallel to the tooth´s side wall. The warmed coupling medium was filled into the interface element. The scanner head was hand-held during acoustic data collection. **Figure 47** illustrates the setup. The obtained recordings will be reffered to as C1 hereinafter.
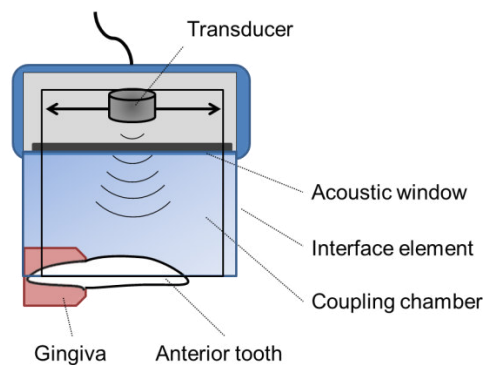

Figure 47: For the *in vivo* data acquisition, the scanner head was placed parallel to the tooth´s side wall.

The properties for all specimens *A*+*, B*-*, B*+*,* and *C1* are summarized in **Table 2** providing information about the temperature of the coupling medium, speed of sound c and the amount of bubbles found.

Table 2: Specimen properties of the *in vitro* experiments (*A+, B-, B+*) and the *in vivo* experiment (*C1*)

Specimen	Calibration body	Temperature	Speed of sound	Amount of bubbles
		T C°	c m/s	
A +	no	21.9	1558	high
B -	yes	18.6	1550	low
B +	yes	18.6	1550	medium
C 1	no/tooth	≈ 36.0	1577	high

4.2 Reference Model

An initial 3D data volume for each sample (A+, B-, B+, and C1) was generated to form the basis of a reference model. To do so, (B-mode) raw data slices were read in into MATLAB (MATLAB/Simulink R2015b, The MathWorks, Inc., Massachusetts, USA) and pre-processing was carried out. Bandpass filtering and envelope detection by means of the Hilbert transformation were performed for each B-mode slice. 3D volume data were acquired by simply aligning all pre-processed slices. Position data have not been applied for simplification.
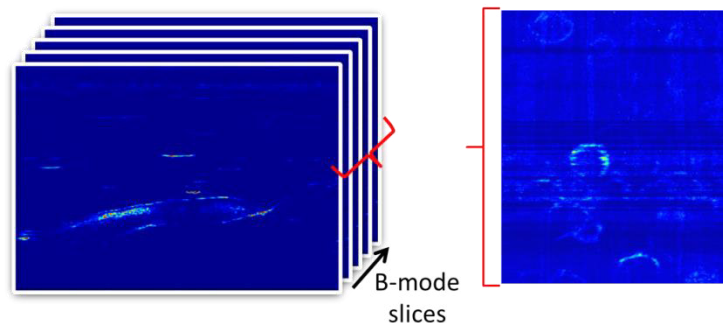

Figure 48: 3D volume data were generated by merging B-mode slices. C-mode images were obtained to visualize the bowl artifact.

C-mode images were generated to visualize bubble artifacts (see **Figure 48**). Median filtering was done to improve the visibility of edges and smooth image noise. Manual boundary segmentation of a bubble´s artifact in gel was performed using the MATLAB built-in function *imfreehand()* and a standard computer mouse. *imfreehand()* allows masking of an image in order to determine parameters such as area (in units of square pixels), center of mass, major

and minor axis (in units of pixels) as well as orientation angle θ of a region of interest (ROI). Bubble artifacts displayed partially only were outlined as well. By default, *imfreehand()* draws a straight line to connect the endpoints of the freehand line to create a closed region (see **Figure 49**). During segmentation, outermost points of the bowl artifact were marked. The segmentation procedure was performed by the author only to guarantee the same assessment for individual bubble artifacts. Information about the marked polygon where stored for further processing. Due to the high sampling frequency f_s of 400 MHz resulting in a large number of C-slices, only every tenth C-slice was processed starting at one.
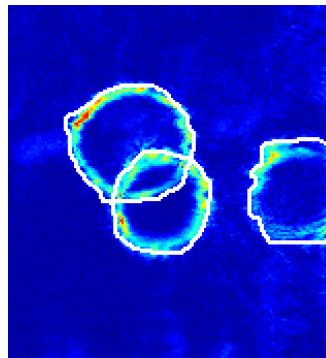

Figure 49: Manual segmentation of the bowl artifact in C-mode images by means of the MATLAB built-in function *imfreehand()*.

In a second step, manually segmented structures of different C-mode slices were clustered according to their center of mass. Therefore, the Euclidean distance (in units of pixels) was determined between the center of mass of a ROI in slice A and a center of mass of a ROI in slice B. If the distance lied within a defined threshold, ROI_B was assumed to be of the same bubble artifact as ROI_A. Segmented and clustered bubble information where stored for further processing and evaluation.

4.3 Implementation

Manual segmentation of the artifactual structure is tedious and time-consuming. Thus, developing a (semi-) automatic segmentation method is advantageous for clinical applications. Two semi-automatic approaches were implemented to be used before the VSAFT algorithm is applied to the acoustic readings acquired by the intraoral scanning system.

.

4.3.1 Indirect signal-based bubble detection

The indirect signal-based detection method is based on the assumption that a bubble causes statistically significant amplitude peaks in the transducer. Therefore, each B-mode slice is pre-processed by applying an envelope detection based on the Hilbert transformation, as well as various signal filtering and smoothing techniques to reduce the impact of noise. For each A-line, peaks above a defined amplitude are extracted using the MATLAB built-in function *findpeaks()*. The function returns a vector with local maxima and the indices at which the peaks occur. After a B-slice was processed, excluded peaks were clustered according to their Euclidean distance. Clusters containing peaks falling below or exceeding a defined intervall are discarded. Cluster centers were computed. In a second step, cluster centers are grouped in the 3D space to form the bowl-like artifact. The assumption is made that the scattering cross-section of the bubble is located at the bowl´s center bottom or top for the near and far field, respectively. Extraction of amplitude peaks caused by the tooth surface is expected as the dental hard tissue presents a strong scatterer in the acoustic field. In theory, the extracted peaks of the tooth are grouped into a huge cluster, thus, exceeding the threshold.

4.3.2 Indirect image-based bubble detection

C-mode images were generated according to **4.2** and stored on a computer for further processing. A median filter was used to improve the visibility of edges and smooth image noise. Morphological operations such as edge-detection and closing (dilation followed by erosion) were applied on binary images to extract the boundaries of the elliptical artifact. The *Hough Transform* (HT) was performed on the methodology introduced by [Xie & Ji 2002] where a one-dimensional accumulator array is used for the voting procedure. A robust implementation was found to be given by Martin Simonovsky whose algorithm is based on the paper mentioned [Simonovsky 2013]. The algorithm was modified to be used for the present problem solution. However, as Simonosky´s code requires a specification about the amount of ellipses to be detected, it just returns the properties of ellipses with the highest score found in the accumulator array. Thus, a threshold was defined to return ellipse properties for scores exceeding the limit. A *Look-Up Table* (LUT) was implemented to change the radius range for the major axis length dependent on the depth of field of investigation. Linear changes before and after the focus was assumed. If ellipse centers were found in close proximity their properties were averaged. After all C-mode slices were processed, ellipses were clustered according to the Euclidean distance between their centers to form the bowl artifact. Information were stored on the computer.

4.4 Evaluation

The reference model was used to evaluate the segmented bowl-artifacts that were obtained by the semi-automated indirect signal-based and image-based approaches. **Figure 50** demonstrates the steps of evaluation. Raw data were read into MATLAB. C-mode images were generated (for the image-based method only). 2D segmentation was performed by detecting ellipses or local maxima clusters in C-mode or B-mode images, respectively. 2D data were stored for comparison with the reference model. A visual examination was carried out. 3D clustering was done grouping the found structures to form the bowl-like artifact. 3D imformation were compared to the reference model as well.
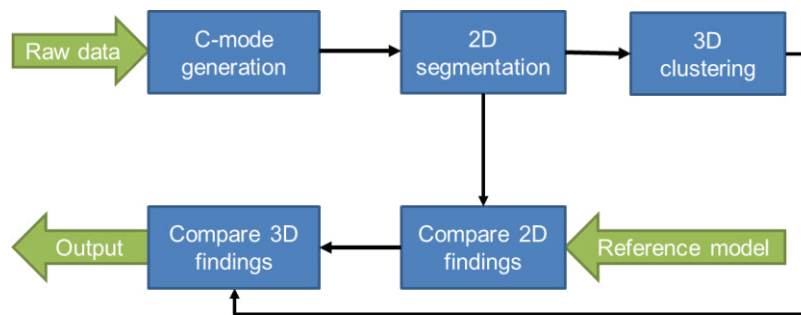

Figure 50: Procedure for the evaluation of segmented bowl artifacts

5.   Results

Two indirect bubble detection methods were implemented as it was described in section **4.3**. Three *in vivo* (*A+*,*B-,* and *B+*) and one *in vivo* (*C1*) experiment were processed for evaluation. Data were analyzed according to section **4.4.**

5.1   Reference model

Reference models were generated for each specimen of the three *in vitro* experiments *A+*, *B-*, and *B+*, as well as for one *in vivo* experiment *C1*. Therefore, the bubble artifacts were manually segmented using the *imfreehand()* function in C-mode images. Due to the high amount of C-mode data available only every tenth slice was processed. Properties such as area, minor and major axis length, and center of mass were determined and stored for each ROI. In a second step, ellipse data are clustered to form the bowl-like artifact. The bottom center of each bowl is assumed to be located at the scattering cross-section of the air bubble.
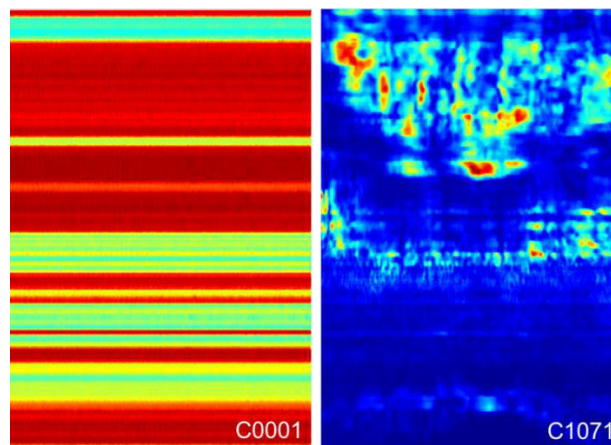

Figure 51: Reverberation artifact in C-mode data for *C1*

For the C-mode images of three *in vitro* experiments, strong artifactual structures were seen and thought to be generated by repeatedly recording lines where the scanner´s trajectory reached its maximum in the last 240 B-slices. After visual inspection, this slices where manually removed from the 3D volume. Results shown hereinafter exclude these slices. Reverberation artifacts caused by the acoustic window are observed in each specimen. In C-mode slices, they can be seen as images of strong noise. The strong reverberation artifacts

were seen to extend into the first 2000 and 2300 slices for the *in vitro* and *in vivo* experiments, respectively. Manual segmentation of bubbles could not be performed in critical slices or was limited due to the low SNR. **Figure 51** shows two C-mode images of *C1* demonstrating the appearance of the reverberation artifact. If two air inclusions are located in close proximity they cause bowl-like artifacts intersecting each other (see **Figure 52**). Each ellipse was marked separately if differentiation was possible. To form a bowl-artifact, the drawn ellipses are clustered by means of the Euclidean distance between the cluster center and the ellipse center. Thus, the two structures on the left are associated to the same bowl group rather than making up separated bowls.
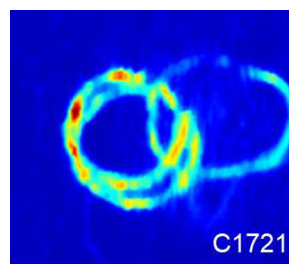

Figure 52: Artifact in close proximity for *B+*.

Table 3 demonstrates the amount of ellipses that were manually segmented as well as the number of bubbles detected. The ellipses were clustered to form the bowl artifact. Each artifact indicates one bubble. Clusters containing one ellipse only were removed as they may have been confused with noise during the segmentation procedure. As aspected the lowest amount of bubbles was found in *B-* as special attention was provided to avoid bubbles in the acoustic field.

Table 3: Number of ellipses drawn, and number of bubbles causing the bowl-like artifact determined by ellipse clustering.

Specimen	Total		Without reverberation	
	No. ellipses	No. bubbles	No. ellipses	No. bubbles
A+	2347	281	1652	212
B -	46	5	8	1
B+	548	43	162	20
C1	3192	332	2794	288

As it was demonstrated in **3.1**, the width of the bowl artifact varies depending on the location of the bubble in relation to the focus of the acoustic beam. **Figure 53** shows the change of the mean major axis length with respect to the sample depth for A+, B-, and B+. As the readings

were done with the same settings other than the temperature of the coupling medium, the focus is assumed to be found in the same depth. A linear change of radius was assumed. A polynomial fit was determined for each region, before and after the expected focus depth. Therefore, data before or after the focus are excluded.
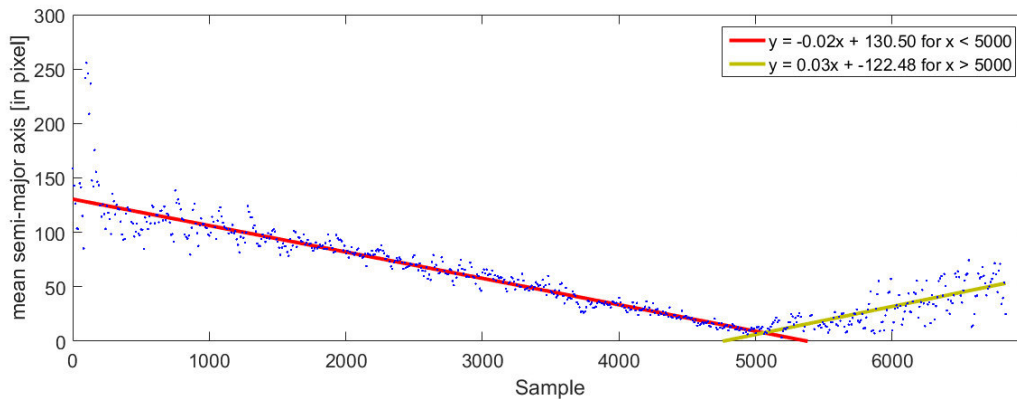

Figure 53: Change of mean major axis length with depth for A+, B-, and B+. Two linear polynomial fit functions were determined for the region before and after the focus.

A similar appearance was seen in the *in vivo* examination demonstrated in **Figure 54**. Due to the strong reverberation artifact within the first C-slices no ellipses were segmented resulting in a low amount of data used for the determination of the linear function. To avoid an intersecting point of the two functions below zero, data were excluded so that the two graphs approximately meet at the assumed focus location. Due to the presence of tooth and gingiva in the acoustic record, low amount of data was provided for regions after the focus.
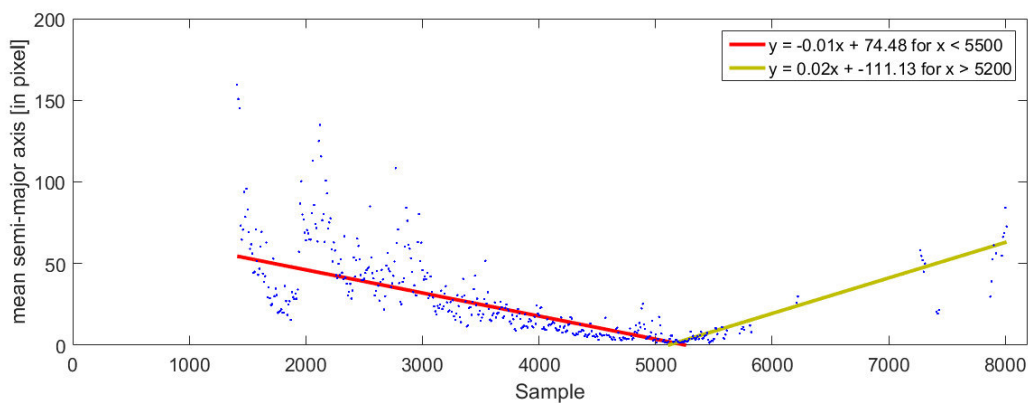

Figure 54: Change of mean major axis length with depth for C1. Two linear polynomial fit functions were determined for the region before and after the focus.

The linear functions were used to generate the LUT for the image-based segmentation approaches. As only a few ellipses were found in B- and B+ a separated determination of

linear functions had no satisfying outcomes. Thus, the averaged data were applied to *A+, B-, and B+*, while the LUT for *C1* was changed.

5.2 Indirect signal-based bubble detection

An indirect signal-based bubble detection algorithm was implemented. Significat amplitude peaks appeared in A-line signals representing a strong echo caused by a static bubble in the ultrasonic field. The locations of the peaks above a pre-defined threshold were clustered by means of the Euclidean distance within a defined radius. The center of each cluster was determined. In a second step, the clusters were grouped to form the bowl-like artifact in 3D space.

Strong reverberation artifacts were observed within the first 2000 samples for *A+*, *B-*, and *B+*, as well as within the first 2300 samples for *C1*. This artifact causes high amplitude outputs at the transducer that are displayed as highly-intensive equidistal lines in all B-mode images (see **Figure 55**). The lines seem to decrease in intensity with depth and appear to be organized in blocks. As their amplitudes exceed the pre-defined threshold for peak detection in a majority of the signals the peaks may be extracted as they are confused of originating from a bubble. Therefore, the corresponding signal regions are excluded from the detection procedure. Results shown hereinafter do not take these sample depths into account.
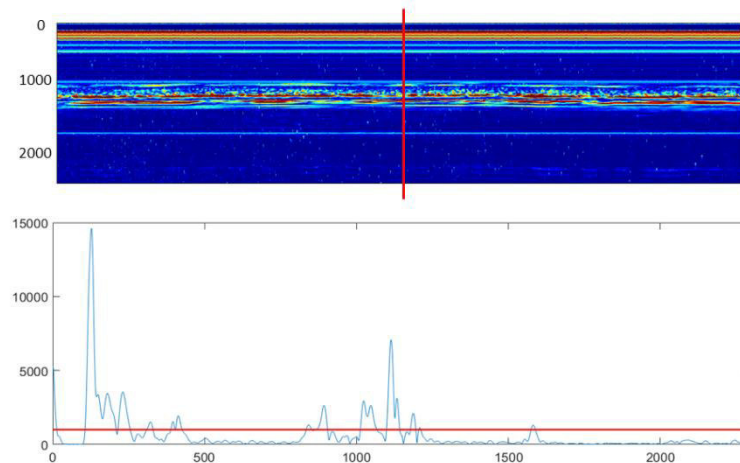

Figure 55: Reverberation artifact within the first 2300 samples observed in B-mode images of the *in vivo* experiment *C1*.

In **Figure 56** a B-mode image of A_+ (left) and its corresponding extracted peaks (right) are shown. The first 2000 signal samples were ignored, thus, the bowl-like artifacts were only detected outside reverberation region.
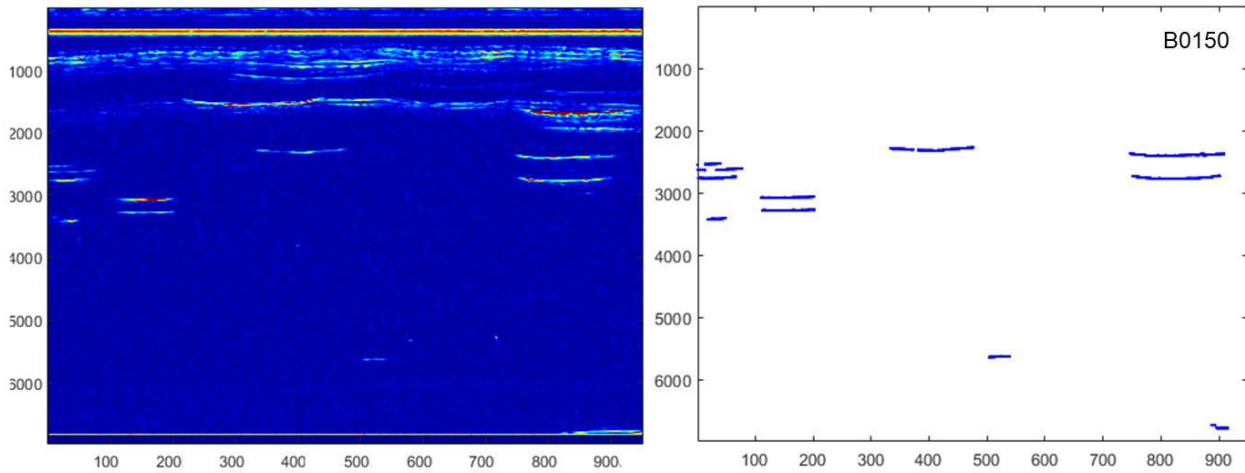
Figure 56: left. B-mode image of A_+; **right.** Bowl peaks extracted by the indirect signal-based approach.

In B-mode images, the width of the bowl-artifact increases until it reaches its maximum and then decreases again until no longer visible. **Figure 57** shows cross-sections through one bowl artifact and its corresponding extracted peaks.
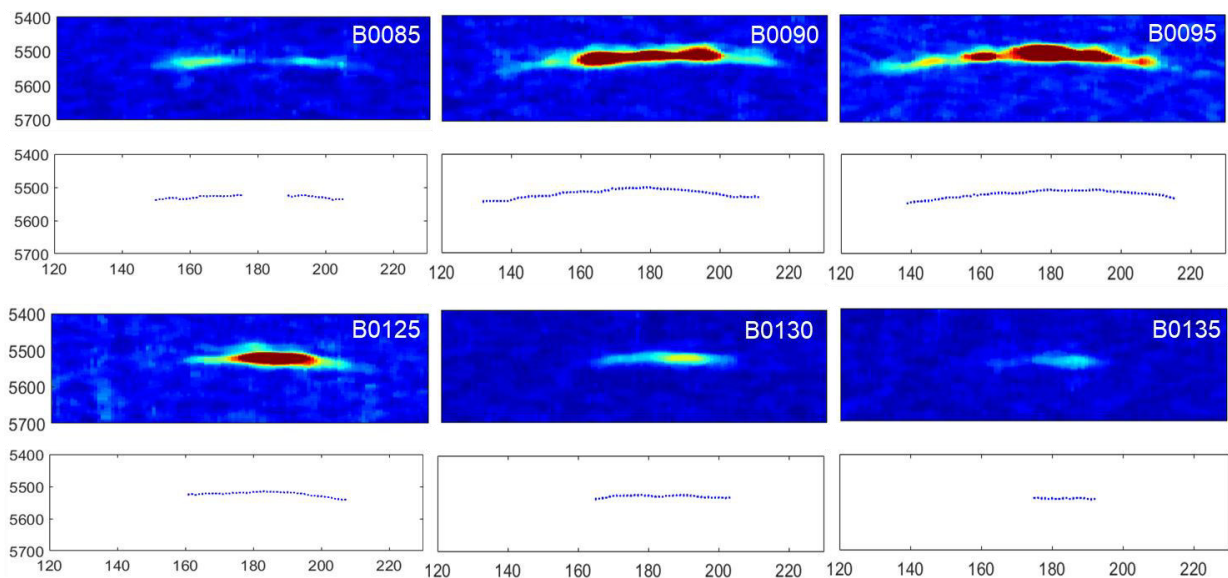

Figure 57: Cross sections through one bowl artifact and corresponding extracted peaks.

By color coding the intensity of the reflected echo is illustrated. Dark blue refers to regions of low amplitude outcomes in the transducer; red indicates regions of high amplitude. Bubble artifacts are not consistently perceived by the transducer. Mostly it is observed that high amplitudes are detected in inner regions of the bowl´s curve in B-mode images. However, exceptions are found as well as seen in the upper left image. The artifact is divided into two parts as being caused by two bubbles. Two peaks clusters are extracted by the detection algorithm. As other strong reflectors in the coupling medium are present in the coupling space, peaks are confused as originating from the bowl-artifact. In **Figure 58** a B-mode image of the calibration body in B+ and the corresponding extracted peaks after clustering are shown. The highest line (marked by the arrow) was removed since it extends the threshold set for the peaks maxima per cluster. Other than assumed, the peaks demonstrating the outline of the calibration body are not clustered as one. Little amount of peaks were found at regions where the body´s surface was aligned parallel to the main beam axis.
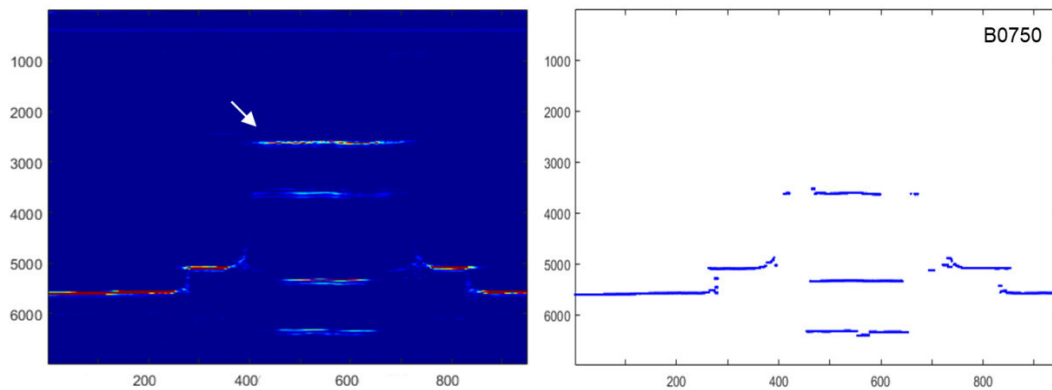

Figure 58: left. B-mode image of the calibration body in B+; **right.** Peaks are extracted caused by the calibration body.

Similar findings were observed for the *in vivo* experiment. As expected, tooth surface and gingiva scatter the acoustic energy to a great extend. However, peak clustering of their surfaces was troublesome due to the unconsistent amplitude outputs recorded; thus, causing several smaller clusters along the surface. An example is given in **Figure 59**. Therefore, removal of big clusters was not given so that they were clustered within the 3D space. For each cluster, the peaks detected in one sample depth were determined. The maximum distance between all peaks was calculated and assumed to be the major axis length of the elliptical structure. The center was defined at the midpoint between the two peak locations. Using the reference model, the outcomes were evaluated. For each manually segmented ellipse, the center and its corresponding major axis length was determined. If a center of a
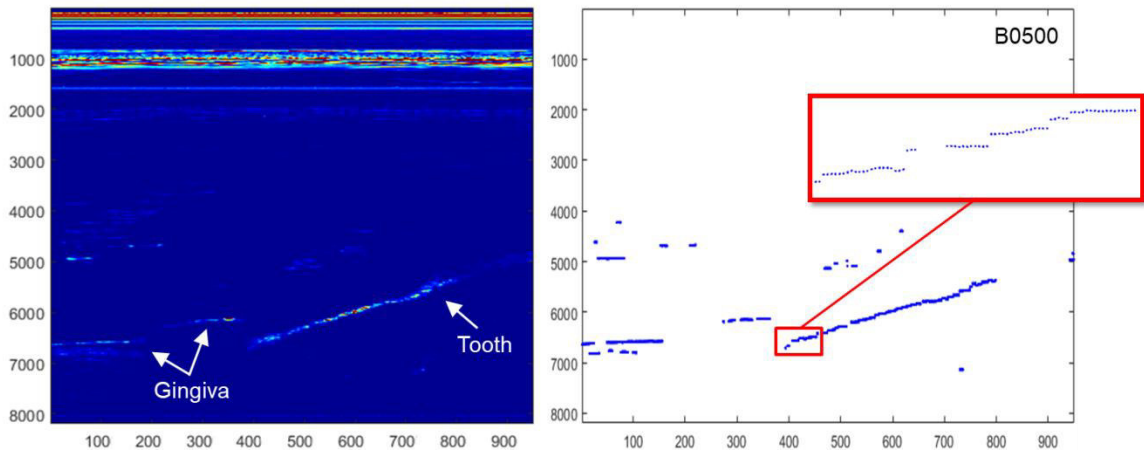
Figure 59: left. B-mode image of the in vivo experiment; **right.** Extracted peaks at the tooth surface were not clustered as one.

detected ellipse was found to be located within the radius of the manually ellipse, it was classified as true positive. The percentage of ellipses classified as true-positive is defined as the ratio of true-positive ellipses to the total number of delineated ellipses. Likewise, the false-positive value is determined. It results from the difference between the detected ellipses and the number of true-positive ellipses. Its percentage is accordingly defined as the ratio of the false-positive to the total number of detected ellipses.
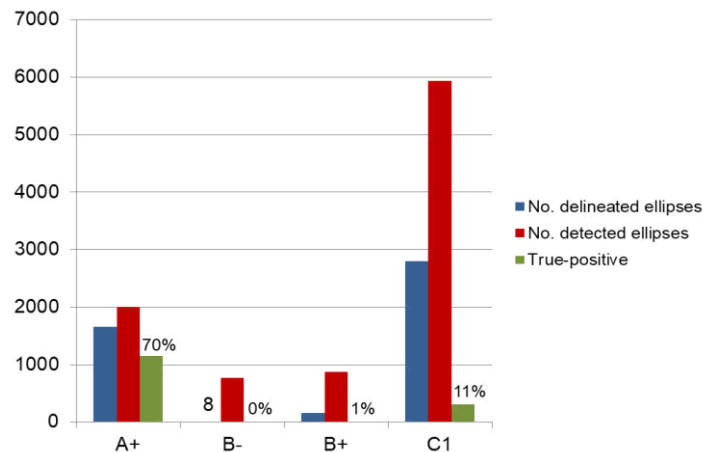
Figure 60: Total number of manually segmented ellipses in the reference model, detected ellipses using the signal-based detection method, and as true-positive classified ellipses.

Figure 60 demonstrates the findings. The highste match was determined for specimen *A+* where no other structures other than the bubble artifacts were present. No elliptical structures classified as true-positive were detected in *B-* and just a low amount of true-positives for *B+*. As expected, a high amount of elliptical structures was determined for C1 as the tooth and gingiva present a strong scatterer in the acoustic field. Due to the incorrect peaks clustering

caused by the inconsistent amplitudes, smaller clusters are confused to be caused by the bowl artifact. False-positive ellipses were found to be 43.5 %, 100.0 %, 99.9 % and 94.9 % for *A+, B-, B+,* and *C1*, respectively.

5.3 Indirect image-based bubble detection

An indirect image-based bubble detection algorithm was implemented detecting the ellipse-like bubble artifacts in C-mode images using the Hough Transformation. A LUT was included to find ellipses of changing major axis length range due the depth-dependency of the artifact relative to the focus in the acoustic field. Again, C-mode slices affected by the reverberation artifact are excluded from the detection procedure. Results shown hereinafter do not take these depth slices into account.

For visual examinations, C-mode slices were displayed. Manually segmented and detected ellipses were marked as simplified circles using the MATLAB in-built function *viscircles().* The corresponding semi-major axis was used as the radius a. Yellow and red circles present detected and manually segmented ellipses, respectively. **Figure 61** demonstrates that the algorithm is able to detect quasi-elliptical structures in sonographic images. Problematic were structures with a low gradient to their surroundings as it can be seen in the right example of the figure. Bubble artifacts were also detected that were not completely located within the image field. However, the center and major axis length between drawn and detected ellipses differ slightly from each other.
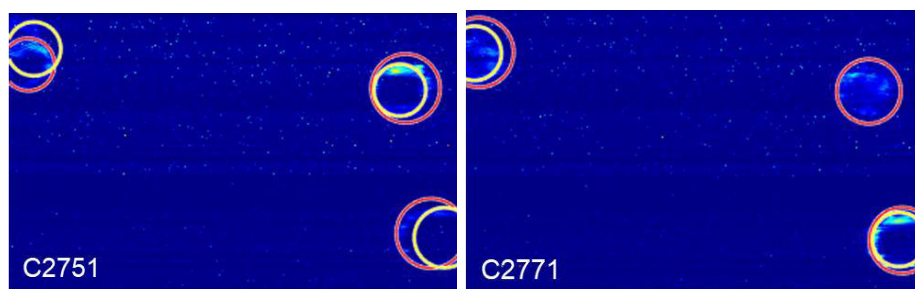
Figure 61: Elliptical structures were automatically detected (yellow) in ultrasonic images by means of the Hough transformation. Two examples are given for *A+*.

Ellipses were falsely detected in regions of strong noise. For each *in vitro* specimen, a field was found that was noisy in a majority of their C-slices. **Figure 62** shows such a field for the A+ sample with the manually segmented (red) and detected (yellow) structures. For visualization, the figure´s contrast and saturation was manipulated to enhance the visibility of

noise. However, the extended false detection of ellipses in these areas was limited to a few slices only. No such region could be defined for *C1*.
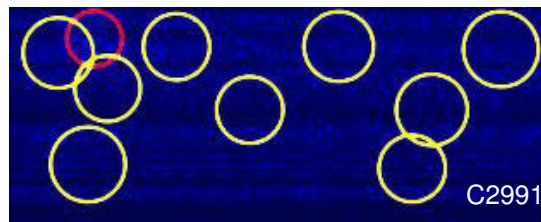
Figure 62: Detected ellipses (yellow) are falsely found in regions of strong noise in *A+*.

Low amplitude outputs of the artifact´s echo in the transducer and a low gradient between adjacent pixels is generally seen to be problematic during the detection process. Then, artifacts are difficult to differentiate from the background. Low amplitudes hinder a consistent noise reduction as wanted structures may be eliminated. **Figure 63** shows a C-slice of the *in vivo* examination demonstrating the limited visibility of bowl artifacts present (left). In the right image the delineated bowl´s ellipses are shown additionally. The detection algorithm recognized the strongest structure only.

Figure 63: Only the strongest elliptical structure was detected by the algorithm.

If two air inclusions are located in close proximity in the acoustic field, their bowl artifacts may intersect when located outside the focus. In such cases, the algorithm may detect it as one ellipse only (see **Figure 64**).

Figure 64: Air bubbles in close proximity cause intersecting artifacts that may be confused as one by the detection algorithm.

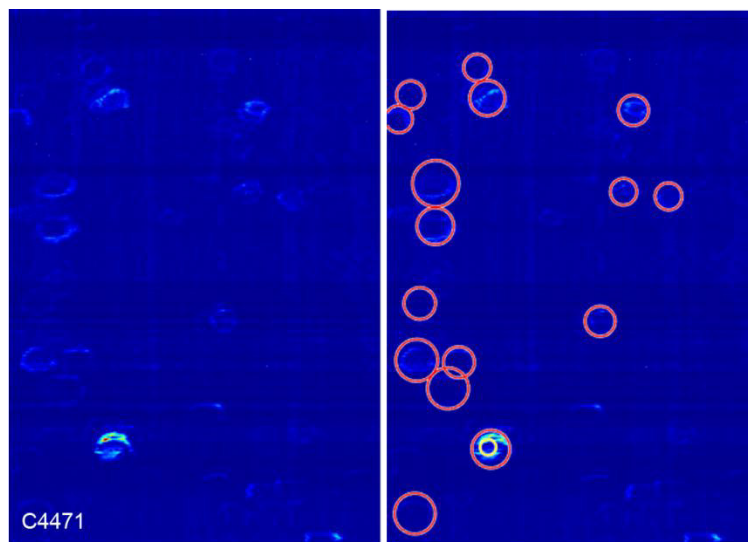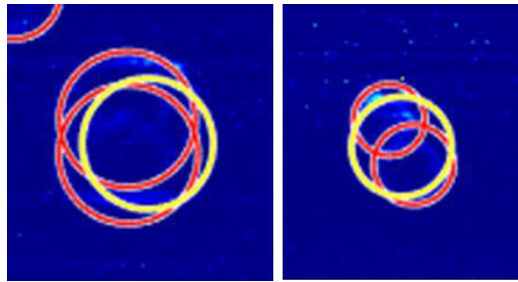In two *in vitro* experiments, *B-* and *B+*, an additional calibration body was used to simulate a tooth structure. The body presents a strong scatterer in the acoustic field. It can be seen that to some extend those structures are falsely identified by the algorithm as being a bowl´s ellipse. The same can be applied to the *in vivo* experiment where tooth structure and gingiva are affected.
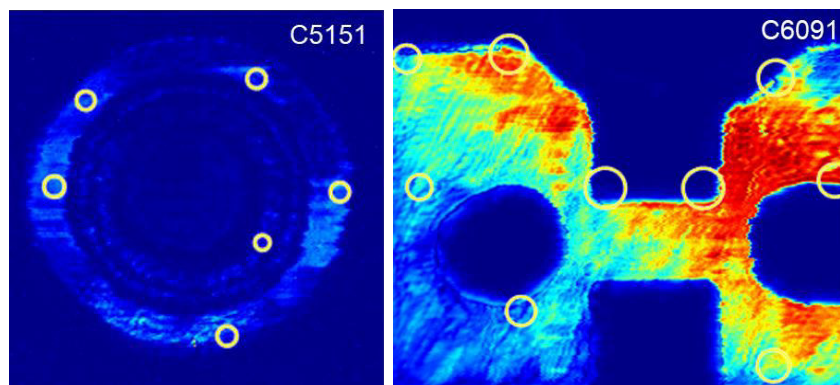
Figure 65: Falsely detected ellipses in B+ at the calibration body.

Due to the LUT integrated into the detection algorithm, elliptical structures out of the detection range are not recognized. However, this is strongly dependent on the position of the structure relative to the focus as the radius range is changed with depth. Manually segmented and detected ellipse properties were evaluated. The reference model is used to determine true-positive detected ellipses. For this purpose, the center of each manually segmented ellipse and the corresponding semi-major axis was determined. If the center of a detected ellipse was within the radius of the manually segmented ellipse, it was classified as true-positive. **Figure 66** shows a bar chart representing the total number of manually segmented ellipses in comparison to detected ellipses and the true-positive ellipses. 13%, 15% and 10% were validated as true-positive for *A+*, *B+*, and *C1*, respectively.

Figure 66: Total number of manually segmeted ellipses in the reference model, detected ellipses using the image-based detection method, and as true-positive classified ellipses.

False-positive detected ellipses were found to be 84.1 %, 100.0 %, 95.8 %, and 77.8 % for *A+*, *B-*, *B+*, and *C1*, respectively.

6. Discussion

The production of high-quality dental restorations requires a detailed reproduction of the intraoral situation. Inaccuracies of fit may cause complications and a repetition of the entire treatment may be necessary. In the digital age, therefore, one reli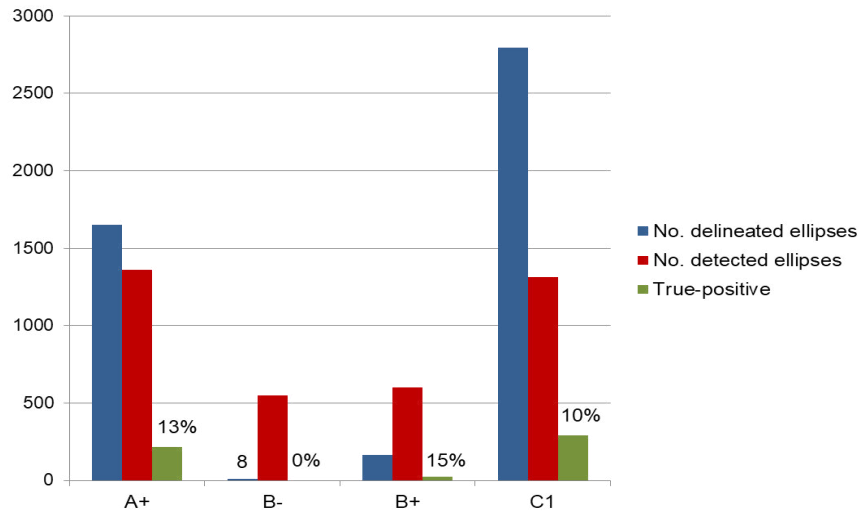es on the reduction of work steps to avoid sources of error. A complete digital process chain is desirable. Ultrasound is a non-invasive method that finds wide application in medical issues. High-frequency ultrasound enables the detection of the tooth surface in the micrometer range. Furthermore, the mechanical longitudinal waves have the ability to penetrate soft biological tissue, such as gingiva or blood. The concept of the microscanner, therefore, overcomes disadvantages given by current procedures for impression taking found on the market. However, as with other medical imaging modalities, sonography is prone to image artifacts. Artifacts may lead to an incorrect data acquisition of the tooth surface resulting in imperfect dental models for the production of artificial dental restorations. Due to their acoustic properties, air bubbles in the coupling space represent a strong degradation factor. It is therefore necessary to keep the ultrasound gel as bubble free as possible. The occurrence of air bubbles, however, cannot be completely avoided. The primary goal of this thesis was to develop a non-invasive method that permits the detection of embedded gas bubbles in the intraoral interface using acoustic readings. The previous chapters have analyzed the appearance and acoustic properties of air inclusions and their artifacts (e.g., shadowing or bowl-like artifact) and requirements for a detection approach were defined. Four concepts were developed in the concept phase where two of which were excluded due to a required change in hardware and the associated lengthening of treatment time. An indirect implementation of bubble identification is provided by recognition of bubble artifacts. Two semi-automatic methods, a signal-based and an image-based method, have been developed. Both methods can, to some extend, be used for the detection of bowl-like artifacts indicating the position of a gas bubble in the acoustic field. After the data evaluation, the scientific questions defined in section **2.4** will be answered within the following discussion.

What are the physical properties of an air bubble? And how can they be described?

A bubble can generally be described as a gas filled inclusion surrounded by any matter such as water or coupling medium in the present system. The gas in the ultrasonic gel is assumed to be air. Due to the surface tension exposed over the bubble, they are typically seen in a spherical shape. However, for greater air inclusions simplified models have to be used as they may adopt various shapes. Thus, an ellipsoid is assumed for a single bubble. Bubbles in the

coupling medium are found to be of macroscopic size. However, microscopic bubbles are also expected due to bubble formation at rough surfaces in the coupling space. The exact size of occuring bubbles was not determined.

How do gas bubbles in an acoustic field behave? And how does this behavior contribute to a feasible detection method?

How an air bubble in the acoustic field behaves is strongly depedent on their size and the initial frequency of insonification. Two phenomena are described: geometrical scattering for $ka \gg 1$, and frequency-dependent volume pulsation for $ka \ll 1$ [Medwin & Clay 1998]. Following the Kirchhoff reflection approximation, specular scattering occurs at the boundaries of the air bubble. Diffraction effects are not taken into account. Due to the high reflection coefficient R at the gel-air boundary, total reflection generates high amplitude outputs at the transducer in pulse-echo measurements. Posterior to the air bubble, a strong attenuation of the acoustic energy can be noticed. Large bubbles cause acoustic shadows that are displayed as regions of low echogenicity in sonographic images. However, smaller bubbles, that satisfy the inequation $ka \ll 1$, are capable of resonating to an incident acoustic wave. Bubbles then behave as a source of sound due to the resonant mechanical oscillations. If the initial frequency is near the natural frequency of the gas bubble, it will effectively scatter and absorb the sound. Both the scattering and absorption cross-sections at resonance are a multiple of the geometrical cross-section. The resonance frequency is inversely proportional to the radius of the bubble. Due to the non-linear acoustic characteristics of air bubbles, resonant bubbles emit a significant second harmonic signal. However, bubbles much larger than resonance size may scatter to a greater extend. As high-frequency acoustic waves are used for acoustic readings with the HFUS-assisted microscanner, only geometric scattering is assumed.

Which parameters for an optimal detection method can be determined?

Due to the high impedance mismatch, no direct visualization of a bubble´s boundary in the acoustic field is possible as a total reflection at the scattering cross-section occurs. Nevertheless, air bubbles in the acoustic field of the HFUS-assisted dental scanner cause a significant artifact that was referred to as bowl-like artifact. The transducer is moved stepwise in a slightly curved path over the entire measuring field. If the bubble is located outside the scanner´s focus, they are insonified from various positions, thus, causing a curved artifact that is strongly dependent on the shape of the acoustic beam. The artifact, therefore, is an indicator for the presence of a bubble. Its properties were summarized in **3.2**

What are constructive methods for the detection of occuring air bubbles?

Based on the acoustic properties of gas bubbles, four basic concepts for bubble detection methods were developed. These are aimed in particular at the geometric properties, as well as the resonance frequency-based and associated non-linear characteristics of gas bubbles. Another detection method is given by the processing of image-based data that are not directly related to the acoustic properties of a bubble. However, the transmissive and resonance-frequency-based approaches require a change of the scanner´s hardware, and additional acoustic readings. Two indirect detection methods, therefore, are pursued making use of the bowl-like artifact. The location of the bubble is determined by clustering.

Can the selected method be applied to *in vitro* and *in vivo* data?

An indirect signal-based and an indirect image-based bubble detection method were realized. Both aimed at segmenting the bowl-like artifact that is caused by bubbles in the trajectory of the transducer. The bowl-like artifact is seen as an ellipse and line in C-mode and B-mode images, respectively. In the signal-based approach, feature extraction is done by determining local maxima above a given threshold for each A-line. By clustering the peaks in 3D space, the segmentation is done. For the image-based segmentation approach, C-mode images were generated. A *Hough Transformation* is used to accumulate the length information of an ellipe´s minor axis in a one-dimensional accumulator array. Both approaches present a potential segmentation technique. However, various limitations are given.

The size and curvature of the bowl-artifact is strongly dependent on the location in the acoustic field relative to the scanner´s focus. It is assumed that the reflections of bubbles in focus are only seen as points. Thus, they can neither be described as an ellipse in C-mode images, nor as a curved line in B-mode. Even though a peak will be extracted in the signal-based approach, provided that it exceeds the minimum amplitude defined, it will be removed during the clustering procedure as clusters of a length below a defined threshold are ignored. The scattered point echo is confused as being noise. The image-based algorithm is able to detect quasi-elliptical structures in sonographic images if the depth-dependent radius range fits the occurring objects. A *Look-Up Tabel* was implemented to change the interval with depth on the basis of the manually segmented ellipses. Due to the limited amount of data, the LUT may not represent common findings. For an exact determination of the depth-dependent radius ranges further experiments and measurements are necessary. Although the intervals can simply be extended, they would then be accompanied by a degradation of the segmentation algorithm as well as additional computation time. The ultrasonic data are strongly affected by the

reverberation artifact in all specimens. It therefore presents a major degradation factor. For both detection methods a manual exclusion of these sample depths was required as they may cause confusion during feature extraction. Accordingly, no segmentation of bowl artifacts was possible in the disposed regions and, thus, no bubbles could be detected. Cutting off the affected samples requires that the reverberation artifact is not found at the level of the tooth to be scanned. In this case, a reduction of the reverberations would be inevitable. By suppressing the reverberation artifact, its influence on the chosen detection methods might be avoided. Reverberation artifacts are commonly encountered during clinical routine examinations. Thus, several publications are found dealing with the recognition, identification and reduction of reverberations in sonographic images [Chang et al. 2008; Kling et al. 1993; Tay et al. 2011]. As ultrasonographic images are prone to noise, the bowl-like artifacts cannot necessarily be clearly distinguished from their background. Thus, manual segmentation and automated segmentation is difficult as some bubble artifacts could not be recognized and identified in the presence of strong noise. Reducing noise in a stronger extend may contribute to an increase in detection ability. To suppress destructive noise and short-term components of a signal, filters are commonly used. However, as some bubbles only cause a low amplitude in the receiver structures of interest may be removed when decreasing noise. Nevertheless, edge-preserving noise reduction methods are found in literature (e.g., [Chinrungrueng & Suvichakorn 2001]). For this study, three ultrasound scans were performed extraorally at a fixed setup without any further movement. Hence, it may not reflect the clinical intraoral situation but avoids additional sources of error. Acoustic *in vivo* readings were provided. The scanning probe was hand-held during examination. Thus, not only the subject movements but also the potential motions of the examiner have to be taken into account. Potential factors include natural breathing, muscle tremors, throat cleaning, swallowing, tongue or mandible movements, coughing of sneezing, as well as varying fixation forces [Vollborn 2017]. Movement artifacts cause a displacement of an echos location or a spatial misalignment in the 3D space [Nelson et al. 2000]. They, therefore, may distort the detection of the bowl-artifact. In the *in vivo* examination it was seen that the detection algorithm could not cluster the extracted local maxima of the tooth surface correctly due to a gap of extracted peaks. This may be caused by the wrong choice of threshold pre-defined for the maxima detection that requires additional examinations to find a universal value. However, variations in the angle of incidence of the sound pulse will reduce the intensity of the backscatter signal. Thus, rough surfaces of strong scatterer may counteract the clustering procedure. Also, due to the anisotropic characteristic of ultrasound image acquisition, data quality varies depending on the view.

While merging different 2D US acquisitions into one volumetric data set, the curvature of the transducer path is neglected due to the great radius of the rotation. However, it may cause distortion of the bowl artifact. Therefore, an elliptical structure was assumed in the image-based approach. However, as a position sensor is included in the scanner head, the position data may be taken into account to reduce the distortion effect. Then, the artifacts cross-sections may be described as a circle and a robust circle detection technique using the *Hough Transformation* can be applied. Several publications are found dealing with this shape recognition method (e.g., [Yuen et al. 1990; Ioannou et al. 1999]). In both the signal-based and the image-based detection algorithm the volumetric data analyzed as sequences of 2D image frames forming the 3D data. A major disadvantage of this approach is the loss of contextual relationships between adjacent frames. A three-dimensional analysis therefore provides the possibility of surface-based analysis rather than obtaining individual sets of two-dimensional contouring [Nelson et al. 2000]. As it was demonstrated in the resulta, both approaches tend to over-segmentation that is typically observed in pixel- and region based segmentation approaches. Incorporating information about topology and relative positions of the objects of interest can improve the accuracy and robustness of the algorithm [Deserno 2011].

7. Conclusion

Two bubble detection methods were introduced using acoustic readings acquired by the HFUS-assisted intraoral microscanner. Both are found to be potential detection methods but show to be limited in their detection ability. Therefore, additional examinations are required to obtain more relevant data for a feasible implementation of the methods. However, as the bubbles are not detected directly no information about the bubble size is provided. The acoustic shielding by proximal gas bubbles may be used to approximate a bubbles size when using a simplified shape model. For future developments, a combination of both methods is conceivable. With the help of the signal-based analysis, local maxima in the 3D volume can be segmented. From the obtained data a point cloud is created. A *Hough Transformation* in the three-dimensional space can then detect the artifacts within the point cloud.

References

[Anusavice 1992] ANUSAVICE, K. J.: Degradability of dental ceramics. In: Advances in dental research, 6 (1992): 82–89

[Bader et al. 1991] BADER, J. D; ROZIER, R. G; MCFALL, W. T; RAMSEY, D. L.: Effect of crown margins on periodontal conditions in regularly attending patients. In: The Journal of Prosthetic Dentistry, 65 (1991), 1: 75–79

[Ballard 1987] BALLARD, D. H.: Generalizing the Hough Transform to detect Arbitrary Shapes. In: Readings in Computer Vision: Elsevier (1987): 714–725

[Barnett et al. 2000] BARNETT, S. B; TER HAAR, G. R; ZISKIN, M. C; ROTT, H.-D; DUCK, F. A; MAEDA, K.: International recommendations and guidelines for the safe use of diagnostic ultrasound in medicine. In: Ultrasound in medicine & biology, 26 (2000), 3: 355–366

[Barr et al. 2013] BARR, R; HINDI, A; PETERSON, C.: Artifacts in diagnostic ultrasound. In: Reports in Medical Imaging (2013): 29

[Beck et al. 1978] BECK, T. W; DANIELS, S; PATON, W. D. M; SMITH, E. B.: Detection of bubbles in decompression sickness. In: Nature, 276 (1978): 173 EP -

[Benech & Novakov 1999] BENECH, P. & NOVAKOV, E.: Ultrasonic detection of air bubbles in ducts using PVDF. In: Measurement Science and Technology, 10 (1999), 11: 1032–1036

[Bennett et al. 1999] BENNETT, N; BURRIDGE, R; SAITO, N.: A method to detect and characterize ellipses using the Hough transform. In: IEEE Transactions on Pattern Analysis and Machine Intelligence, 21 (1999), 7: 652–657

[BMG 2009] BMG: Gesetzliche Krankenversicherung: Abrechnungs- und Leistungsfälle ambulanter Behandlung: Ergebnisse der GKV-Statistik KG 3/2007. Bonn: Bundesministerium für Gesundheit (2009)

[BMG 2012] BMG: Abrechnungsfälle der KG 3: BMG, Referat G 11. Bonn: Bundesministerium für Gesundheit (2012)

[Boas & Fleischmann 2012] BOAS, F. E. & FLEISCHMANN, D.: CT artifacts. Causes and reduction techniques. In: Imaging Med, 4 (2012), 2: 229–240

[Boeddinghaus et al. 2015] BOEDDINGHAUS, M; BRELOER, E. S; REHMANN, P; WÖSTMANN, B.: Accuracy of single-tooth restorations based on intraoral digital and conventional impressions in patients. In: Clinical oral investigations, 19 (2015), 8: 2027–2034

[Brecht et al. 2009] BRECHT, J. G; MEYER, V. P; MICHEELIS, W.: Prognose der Zahnärztezahl und des Bedarfs an zahnärztlichen Leistungen bis zum Jahr 2030. Köln: IDZ, Institut der Deutschen Zahnärzte (2009)

[Burckhardt 1993] BURCKHARDT, C. B.: Signalverarbeitung in Ultraschallabbildung, Doppler und Dopplerabbildung. In: Ultraschall in der Medizin, 14 (1993), 5: 220–224

[Calliada et al. 1998] CALLIADA, F; CAMPANI, R; BOTTINELLI, O; BOZZINI, A; SOMMARUGA, M. G.: Ultrasound contrast agents. Basic principles. In: European journal of radiology, 27 Suppl 2 (1998): S157-60

[CanStock 2018] CAN STOCK PHOTO INC. (ed.) CANSTOCK (2018); URL: https://www.canstockphoto.de/. Zuletzt geprüft am: Jan 2018

[Chang et al. 2008] CHANG, Y.-F; MA, Y; LIN, C.-M; LEE, J.-H.: Reverberation reduction in ultrasonic images via predictive deconvolution. In: NDT & E International, 41 (2008), 4: 235–241

[Chen et al. 2003] CHEN, D.-R; CHANG, R.-F; WU, W.-J; MOON, W. K; WU, W.-L.: 3-D breast ultrasound segmentation using active contour model. In: Ultrasound in medicine & biology, 29 (2003), 7: 1017–1026

[Chinrungrueng & Suvichakorn 2001] CHINRUNGRUENG, C. & SUVICHAKORN, A.: Fast edge-preserving noise reduction for ultrasound images. In: IEEE Transactions on Nuclear Science, 48 (2001), 3: 849–854

[Chuembou et al. 2014] CHUEMBOU, F; HARBOR, D; RADERMACHER, K; HEGER, S.: TPS-RPM based segmentation of three-dimensional high frequency ultrasound SAFT images for CAD/CAM based tooth digitization. In: 2014 IEEE International Ultrasonics Symposium: IEEE (2014): 2347–2350

[Chuembou Pekam et al. 2015] CHUEMBOU PEKAM, F; MAROTTI, J; WOLFART, S; TINSCHERT, J; RADERMACHER, K; HEGER, S.: High-frequency ultrasound as an option for scanning of prepared teeth. An in vitro study. In: Ultrasound in medicine & biology, 41 (2015), 1: 309–316

References

[Chuembou Pekam et al. 2011] CHUEMBOU PEKAM, F; VOLLBORN, T; KENGNE, P; RADERMACHER, K; HEGER, S.: Preliminary Investigation of Ultrasound-based teeth geometry detection using Monostatic Synthetic Aperture Focusing. In: Biomedizinische Technik/Biomedical Engineering, 56 (2011), s1: 1–8

[Chuembou Pekam et al. 2012] CHUEMBOU PEKAM, F; VOLLBORN, T; TINSCHERT, J; WOLFART, S; RADERMACHER, K; HEGER, S.: Sensitivity analysis of synthetic aperture focusing based on the virtual source point for high-frequency ultrasound imaging. In: 2012 IEEE International Ultrasonics Symposium: IEEE (2012): 1–4

[Chui & Rangarajan 2003] CHUI, H. & RANGARAJAN, A.: A new point matching algorithm for non-rigid registration. In: Computer Vision and Image Understanding, 89 (2003), 2-3: 114–141

[Cootes et al. 2001] COOTES, T. F; EDWARDS, G. J; TAYLOR, C. J.: Active appearance models. In: IEEE Transactions on Pattern Analysis and Machine Intelligence, 23 (2001), 6: 681–685

[Culjat et al. 2010] CULJAT, M. O; GOLDENBERG, D; TEWARI, P; SINGH, R. S.: A review of tissue substitutes for ultrasound imaging. In: Ultrasound in medicine & biology, 36 (2010), 6: 861–873

[Davey & Stather-Dunn 2005] DAVEY, C. & STATHER-DUNN, T.: Very small air bubbles (10 - 70 microl) cause clinically significant variability in syringe pump fluid delivery. In: Journal of medical engineering & technology, 29 (2005), 3: 130–136

[Della Bona & Kelly 2008] DELLA BONA, A. & KELLY, J. R.: The clinical success of all-ceramic restorations. In: Journal of the American Dental Association (1939), 139 Suppl (2008): 8S-13S

[Deserno 2011] DESERNO, T. M.: Biomedical image processing. Berlin, Heidelberg, New York: Springer (2011) (Biological and medical physics, biomedical engineering)

[DIN EN ISO 3950 2016] DIN EN ISO 3950: Zahnheilkunde - Bezeichnungssystem für Zähne und Mundhöhlenbereiche (ISO 3950:2016) (2016-09)

[Duck 2012] DUCK, F. A.: Physical Properties of Tissue. York: IPEM (2012)

[Duda & Hart 1972] DUDA, R. O. & HART, P. E.: Use of the Hough transformation to detect lines and curves in pictures. In: Communications of the ACM, 15 (1972), 1: 11–15

References

[Dutta et al. 2012] DUTTA, S; WOO, R. K; KRUMMEL, T. M.: Advanced and Emerging Surgical Technologies and the Process of Innovation. In: Pediatric Surgery: Elsevier (2012): 37–75

[El-Anwar et al. 2015] EL-ANWAR, M. I; TAMAM, R. A; FAWZY, U. M; YOUSIEF, S. A.: The effect of luting cement type and thickness on stress distribution in upper premolar implant restored with metal ceramic crowns. In: Tanta Dental Journal, 12 (2015), 1: 48–55

[Fasbinder 2010] FASBINDER, D. J.: Digital dentistry. Innovation for restorative treatment. In: Compendium of continuing education in dentistry (Jamesburg, N.J. 1995), 31 Spec No 4 (2010): 2-11; quiz 12

[Feldman et al. 2009] FELDMAN, M. K; KATYAL, S; BLACKWOOD, M. S.: US artifacts. In: Radiographics a review publication of the Radiological Society of North America, Inc, 29 (2009), 4: 1179–1189

[Feuillade & Werby 1994] FEUILLADE, C. & WERBY, M. F.: Resonances of deformed gas bubbles in liquids. In: The Journal of the Acoustical Society of America, 96 (1994), 6: 3684–3692

[Frigerio 2006] FRIGERIO, F.: 3-dimensional surface imaging using Active Wavefront Sampling (2006)

[Gladbach 2018] GLADBACH, K. M.: Konstruktion und Evaluierung einer Vorrichtung zur intraoralen Gelapplikation für einen ultraschallbasierten Dentalscanner. Aachen (2018)

[Goodacre et al. 2003] GOODACRE, C. J; BERNAL, G; RUNGCHARASSAENG, K; KAN, J. Y.: Clinical complications in fixed prosthodontics. In: The Journal of Prosthetic Dentistry, 90 (2003), 1: 31–41

[Haberman & Morton 1953] HABERMAN, W. L; MORTON, R. K.: An Experimental Investigation of the Drag and Shape of Air Bubbles Rising in Various Liquids: Navy Department (1953) (Report)

[Hart et al. 2004] HART, D. P; LAMMERDING, J; ROHALY, J. (2004): 3-D imaging system

[Heger et al. 2011] HEGER, S; VOLLBORN, T; TINSCHERT, J; CHUEMBOU, F; WOLFART, S; RADERMACHER, K.: High frequency (75MHz) ultrasound based tooth digitization using sparse spatial compounding. In: Ultrasonics Symposium (IUS), 2011 IEEE International (2011): 2257–2260

[Hoffmann et al. 2006] HOFFMANN, T; JOHN, M. T; KERSCHBAUM, T; MICHEELIS, W; POTTHOFF, P; REICH, E; REIS, U; REITER, F; SCHIFFNER, U; SCHROEDER, E.: Vierte Deutsche Mundgesundheitsstudie (DMS IV). Neue Ergebnisse zu oralen Erkrankungsprävalenzen, Risikogruppen und zum zahnärztlichen Versorgungsgrad in Deutschland 2005. Köln: Dt. Zahnärzte-Verl., DÄV (2006) (Materialienreihe / Institut der Deutschen Zahnärzte, Bd. 31)

[Hoskins 1990] HOSKINS, P. R.: Measurement of arterial blood flow by Doppler ultrasound. In: Clinical physics and physiological measurement an official journal of the Hospital Physicists' Association, Deutsche Gesellschaft fur Medizinische Physik and the European Federation of Organisations for Medical Physics, 11 (1990), 1: 1–26

[Hough 1960] HOUGH, P. V. (1960): Method and Means for Recognizing Complex Patterns

[Ignee et al. 2016] IGNEE, A; ATKINSON, N. S. S; SCHUESSLER, G; DIETRICH, C. F.: Ultrasound contrast agents. In: Endoscopic ultrasound, 5 (2016), 6: 355–362

[Ioannou et al. 1999] IOANNOU, D; HUDA, W; LAINE, A. F.: Circle recognition through a 2D Hough Transform and radius histogramming. In: Image and Vision Computing, 17 (1999), 1: 15–26

[Jenderka 2013] JENDERKA, K.-V.: Ausbreitung von Ultraschall im Gewebe und Verfahren der Ultraschallbildgebung. In: Der Radiologe, 53 (2013), 12: 1137–1150

[Jong et al. 1985] JONG, N. de; BOM, N; SOUQUET, J; FABER, G.: Vibration modes, matching layers and grating lobes. In: Ultrasonics, 23 (1985), 4: 176–182

[Kaeley & Wakefield 2010] KAELEY, G. S; WAKEFIELD, R. J. B. M. F.: Essential Applications of Musculoskeletal Ultrasound in Rheumatology: Elsevier (2010)

[Kim et al. 2005] KIM, Y; OH, T.-J; MISCH, C. E; WANG, H.-L.: Occlusal considerations in implant therapy. Clinical guidelines with biomechanical rationale. In: Clinical oral implants research, 16 (2005), 1: 26–35

[Kirberger 1995] KIRBERGER, R. M.: Imaging Artifacts In Diagnostic Ultrasound-A Review. In: Veterinary Radiology <html_ent glyph="@amp;" ascii="&"/> Ultrasound, 36 (1995), 4: 297–306

[Kling et al. 1993] KLING, T; SHUNG, K. K; THIEME, G. A.: Reverberation reduction in ultrasonic B-mode images via dual frequency image subtraction. In: IEEE Transactions on Medical Imaging, 12 (1993), 4: 792–802

References

[Knoernschild & Campbell 2000] KNOERNSCHILD, K. L. & CAMPBELL, S. D.: Periodontal tissue responses after insertion of artificial crowns and fixed partial dentures. In: The Journal of Prosthetic Dentistry, 84 (2000), 5: 492–498

[Krawczyk et al. 2005] KRAWCZYK, O; GEHRKE, B; LEGLER, H; RAMMER, C; FELDMANN, M; DÖSSEL, O; REUMANN, M. (eds.): BMBF Medizintechnikstudie 2005: Situation der Medizintechnik in Deutschland im internationalen Vergleich. Aachen, Frankfurt: Bundesministerium für Bildung und Forschung (2005) (Bd. 1)

[Kremkau & Taylor 1986] KREMKAU, F. W. & TAYLOR, K. J.: Artifacts in ultrasound imaging. In: Journal of ultrasound in medicine official journal of the American Institute of Ultrasound in Medicine, 5 (1986), 4: 227–237

[Kressel & Filly 1978] KRESSEL, H. Y. & FILLY, R. A.: Ultrasonographic appearance of gas-containing abscesses in the abdomen. In: AJR. American journal of roentgenology, 130 (1978), 1: 71–73

[Kropatsch et al. 2007] KROPATSCH, W. G; KAMPEL, M; HANBURY, A; HANSEGÅRD, J; ORDERUD, F; RABBEN, S. I. (eds.): Real-Time Active Shape Models for Segmentation of 3D Cardiac Ultrasound. Computer Analysis of Images and Patterns: Springer Berlin Heidelberg (2007)

[Krupa & Bekiesińska-Figatowska 2015] KRUPA, K. & BEKIESIŃSKA-FIGATOWSKA, M.: Artifacts in magnetic resonance imaging. In: Polish journal of radiology, 80 (2015): 93–106

[Laing & Kurtz 1982] LAING, F. C. & KURTZ, A. B.: The importance of ultrasonic side-lobe artifacts. In: Radiology, 145 (1982), 3: 763–768

[Laplace 1806] LAPLACE, P. S.: Méchanique céleste. 10th volume (1806)

[Lehmann et al. 2009] LEHMANN, K. M; HELLWIG, E; WENZ, H.-J.: Zahnärztliche Propädeutik. Einführung in die Zahnheilkunde ; mit 34 Tabellen. 11., überarb. und erw. Aufl. Köln: Dt. Zahnärzte-Verl. (2009)

[Leighton 1994] LEIGHTON, T. G.: Acoustic bubble detection-I. The detection of stable gas bodies. In: Environmental engineering, 7 (1994): 9–16

[Lerch et al. 2009] LERCH, R; SESSLER, G; WOLF, D.: Technische Akustik. Grundlagen und Anwendungen. Berlin/Heidelberg: Springer Berlin Heidelberg (2009)

References

[Liu et al. 2010] LIU, B; CHENG, H. D; HUANG, J; TIAN, J; TANG, X; LIU, J.: Probability density difference-based active contour for ultrasound image segmentation. In: Pattern Recognition, 43 (2010), 6: 2028–2042

[Medwin 1977] MEDWIN, H.: Counting bubbles acoustically. A review. In: Ultrasonics, 15 (1977), 1: 7–13

[Medwin & Clay 1998] MEDWIN, H; CLAY, C. S.: Fundamentals of acoustical oceanography. Boston: Academic Press (1998) (Applications of modern acoustics)

[Meyer & Skudrzyk 1953] MEYER, E. & SKUDRZYK, E.: Über die akustischen Eigenschaften von Gasblasen-schleiern in Wasser. In: Acta Acustica united with Acustica, 3 (1953), 6: 434–440

[Meyer et al. 2014] AWMFONLINE (ed.) MEYER, G; AHSBAHS, S; KERN, M; AHLERS, M. O; BECK, J; BARTSCH, K; CHRISTELSOHN, K; REISS, B; BEUER, F. (2014): S3-Leitlinie 083/012: Vollkeramische Kronen und Brücken; URL: http://www.awmf.org/leitlinien/detail/ll/083

[Miller 1981] MILLER, D. L.: Ultrasonic detection of resonant cavitation bubbles in a flow tube by their second-harmonic emissions. In: Ultrasonics, 19 (1981), 5: 217–224

[Murtaza et al. 2008] MURTAZA, A; MAGEE, D; DASGUPTA, U.: Texas Instruments - Signal Processing Overview of Ultrasound Systems for Medical Imaging (White Paper) (2008)

[Nelson et al. 2000] NELSON, T. R; PRETORIUS, D. H; HULL, A; RICCABONA, M; SKLANSKY, M. S; JAMES, G.: Sources and impact of artifacts on clinical three-dimensional ultrasound imaging. In: Ultrasound in obstetrics & gynecology the official journal of the International Society of Ultrasound in Obstetrics and Gynecology, 16 (2000), 4: 374–383

[Nishi 1972] NISHI, R. Y.: Ultrasonic detection of bubbles with doppler flow transducers. In: Ultrasonics, 10 (1972), 4: 173–179

[Nyland & Mattoon 2002] NYLAND, T. G; MATTOON, J. S.: Small animal diagnostic ultrasound. 2nd ed. Philadelphia [etc.]: Saunders (2002)

[Olympus IMS 2007] OLYMPUS IMS (2007): Grating Lobes and Side Lobes | Olympus IMS; URL: https://www.olympus-ims.com/en/ndt-tutorials/transducers/lobes/. Zuletzt geprüft am: 04.05.2018

[Oppelt 2011] OPPELT, A.:Imaging systems for medical diagnostics. Fundamentals, technical solutions and applications for systems applying ionization radiation, nuclear magnetic resonance and ultrasound. 2nd ed. Erlangen: Publicis Corporate Pub (2011)

[Ozeri et al. 2006] OZERI, S; SHMILOVITZ, D; FAINGUELERNT, J.: Ultrasonic Air Bubble Detection Employing Signal Processing Techniques. In: Lavoie, M; Al-Haddad, K; Lagacé, P. J. (eds.): ISIE 2006 program. International Symposium on Industrial Electronics 2006 July 9th to 13th, 2006 Montreal, Canada. Piscataway, NJ: IEEE (2006): 2840–2845

[Padbury et al. 2003] PADBURY, A; EBER, R; WANG, H.-L.: Interactions between the gingiva and the margin of restorations. In: Journal of clinical periodontology, 30 (2003), 5: 379–385

[Palin & Burke 2005] PALIN, W. & BURKE, F. J. T.: Trends in indirect dentistry. 8. CAD/CAM technology. In: Dental update, 32 (2005), 10: 566–572

[Papula 2009] PAPULA, L.: Mathematische Formelsammlung. Für Ingenieure und Naturwissenschaftler ; mit zahlreichen Rechenbeispielen und einer ausführlichen Integraltafel. 10., überarbeitete und erw. Aufl. Wiesbaden: Vieweg + Teubner (2009) (Vieweg Studium)

[Park et al. 1981] PARK, R; NYLAND, T; LATTIMER, J; MILLER, C; LEBEL, J.: B-mode gray-scale ultrasound imaging artifacts and interpretation principles. In: Veterinary Radiology, 22 (1981), 5: 204–210

[Passmann & Ermert 1996] PASSMANN, C. & ERMERT, H.: A 100-MHz ultrasound imaging system for dermatologic and ophthalmologic diagnostics. In: IEEE Transactions on Ultrasonics, Ferroelectrics and Frequency Control, 43 (1996), 4: 545–552

[Phatale et al. 2010] PHATALE, S; MARAWAR, P. P; BYAKOD, G; LAGDIVE, S. B; KALBURGE, J. V.: Effect of retraction materials on gingival health. A histopathological study. In: Journal of Indian Society of Periodontology, 14 (2010), 1: 35–39

[Reich et al. 2012] REICH, S. M; VOLLBORN, T; WOLFART, S.: Die optische intraorale Abformung - vier Systeme im Überblick. In: Deutsche Zahnärztliche Zeitschrif (2012), 67: 177–189

[Riedel 2016] RIEDEL, C. M.: Entwicklung und Evaluation eines Ankopplungselements für ein intraorales Ultraschallgerät. Aachen (2016)

[Scanlan 1991] SCANLAN, K. A.: Sonographic artifacts and their origins. In: AJR. American journal of roentgenology, 156 (1991), 6: 1267–1272

[Schlottmann 2001] SCHLOTTMANN, K. (2001): Neue sonographische Techniken: Wird die Bildgebung einfacher?. 39. Bayerischer Internisten-Kongress 2000, W. München

[Schmidt 2010] SCHMIDT, V. (2010): 3d Dental Camera for Recording Surface Structures of a Measuring Object by Means of Triangulation

[Seelbach et al. 2013] SEELBACH, P; BRUECKEL, C; WÖSTMANN, B.: Accuracy of digital and conventional impression techniques and workflow. In: Clinical oral investigations, 17 (2013), 7: 1759–1764

[Simonovsky 2013] SIMONOVSKY, M. (2013): Ellipse Detection Using 1D Hough Transform; URL: https://de.mathworks.com/matlabcentral/fileexchange/33970-ellipse-detection-using-1d-hough-transform. Zuletzt geprüft am: 04.03.2018

[Sommer & Taylor 1980] SOMMER, F. G. & TAYLOR, K. J.: Differentiation of acoustic shadowing due to calculi and gas collections. In: Radiology, 135 (1980), 2: 399–403

[Sousa & Mourão 2015] SOUSA, J. M. B. R. de & MOURÃO, J. I. d. B.: Tooth injury in anaesthesiology. In: Brazilian journal of anesthesiology (Elsevier), 65 (2015), 6: 511–518

[Strasberg 1953] STRASBERG, M.: The Pulsation Frequency of Nonspherical Gas Bubbles in Liquids. In: The Journal of the Acoustical Society of America, 25 (1953), 3: 536–537

[Strassler 2011] BENCO DENTAL (ed.) STRASSLER, H. E. (2011): Tissue Management, Gingival Retraction and Hemostasis; URL: http://d3e9u3gw8odyw8.cloudfront.net/ie2_ce_tissue_management.pdf

[Strub 2011] STRUB, J. R.: Curriculum Prothetik, Band I-III. 4., überarb. Aufl. Berlin: Quintessenz (2011) (I)

[Susic et al. 2017] SUSIC, I; TRAVAR, M; SUSIC, M.: The application of CAD / CAM technology in Dentistry. In: IOP Conference Series: Materials Science and Engineering, 200 (2017): 12020

[Taneva et al. 2015] TANEVA, E; KUSNOTO, B; EVANS, C. A.: 3D Scanning, Imaging, and Printing in Orthodontics. In: Bourzgui, F. (ed.): Issues in Contemporary Orthodontics: InTech (2015)

References

[Tay et al. 2011] TAY, P. C; ACTON, S. T; HOSSACK, J. A.: A wavelet thresholding method to reduce ultrasound artifacts. In: Computerized medical imaging and graphics the official journal of the Computerized Medical Imaging Society, 35 (2011), 1: 42–50

[Tipler & Mosca 2009] TIPLER, P. A; MOSCA, G.: Physik. Für Wissenschaftler und Ingenieure. 6. Aufl. Heidelberg: Spektrum Akad. Verl. (2009) (OnlinePLUS)

[Tortora & Nielsen 2012] TORTORA, G. J; NIELSEN, M. T.: Principles of human anatomy. 12. ed. Chichester: John Wiley & Sons (2012)

[van der Meer et al. 2012] VAN DER MEER, W. J; ANDRIESSEN, F. S; WISMEIJER, D; REN, Y.: Application of intra-oral dental scanners in the digital workflow of implantology. In: PloS one, 7 (2012), 8: e43312

[van Ginneken et al. 2002] VAN GINNEKEN, B; FRANGI, A. F; STAAL, J. J; TER HAAR ROMENY, B. M; VIERGEVER, M. A.: Active shape model segmentation with optimal features. In: IEEE Transactions on Medical Imaging, 21 (2002), 8: 924–933

[Vollborn 2017] VOLLBORN, T.: Intraoraler Ultraschallmikroscanner für die digitale Abdrucknahme von Zahnpräparationen. 1. Auflage. Herzogenrath: Shaker (2017) (Aachener Beiträge zur Medizintechnik, Bd. 44)

[Walker 1996] WALKER, M.: Doppler bubble detection after hyperbaric exposure. In: SPUMS journal, 26 (1996), 3: 146–154

[Wen et al. 2014] WEN, W; ZONG, G; BI, S.: A bubble detection system for propellant filling pipeline. In: The Review of scientific instruments, 85 (2014), 6: 65106

[Werner 2009] WERNER, M.: Digitale Signalverarbeitung mit MATLAB®. Grundkurs mit 16 ausführlichen Versuchen ; mit 76 Tabellen. 4., durchgesehene und ergänzte Auflage. Wiesbaden: Vieweg+Teubner Verlag / GWV Fachverlage GmbH, Wiesbaden (2009)

[Weston 1967] WESTON, D. E.: Sound propagation in the presence of bladder fish. In: Underwater acoustics, 2 (1967): 55–88

[whitesonic GmbH 2017] WHITESONIC GMBH (2017): Gebrauchsanweisung. Produktserie S.CAI. Aachen

[Wicks 2013] WICKS, S. (2013); URL:
https://sites.google.com/site/stephsultrasound/home/physics-fun/artifacts. Zuletzt geprüft
am: 04.05.2018

[Wildman & Huettel 2012] WILDMAN, R. A. & HUETTEL, M.: Acoustic detection of gas bubbles in
saturated sands at high spatial and temporal resolution. In: Limnology and Oceanography:
Methods, 10 (2012), 3: 129–141

[Wildt 1946] WILDT, R. ((ed.): Physics of Sound in the Sea. Chapter 28. Acoustic theory of
bubbles. Washington DC, USA (1946) (Bd. 8)

[Wimmer 2009] WIMMER, A.-M.: Experimentelle Untersuchungen zur Form praxisüblicher
Kronenstumpfpräparationen. @Halle, Univ., Medizinische Fakultät, Diss.,. Halle, Saale:
Universitäts- und Landesbibliothek Sachsen-Anhalt (2009)

[Xie & Ji 2002] XIE, Y. & JI, Q.: A new efficient ellipse detection method. In: Object recognition
supported by user interaction for service robots: IEEE Comput. Soc (2002): 957–960

[Yuen et al. 1990] YUEN, H. K; PRINCEN, J; ILLINGWORTH, J; KITTLER, J.: Comparative study of
Hough Transform methods for circle finding. In: Image and Vision Computing, 8 (1990), 1:
71–77

[Zaitsev et al. 2015] ZAITSEV, M; MACLAREN, J; HERBST, M.: Motion artifacts in MRI. A complex
problem with many partial solutions. In: Journal of magnetic resonance imaging JMRI, 42
(2015), 4: 887–901